

DISSERTATION

INVESTIGATION OF LASER COOLING AND TRAPPING OF ATOMIC SILICON:
TOWARDS THE DEVELOPMENT OF A DETERMINISTIC SINGLE ION SOURCE

Submitted by

Samuel R. Ronald

Department of Physics

In partial fulfillment of the requirements

For the Degree of Doctor of Philosophy

Colorado State University

Fort Collins, Colorado

Spring 2023

Doctoral Committee:

Advisor: Siu Au Lee

Co-Advisor: William M. Fairbank, Jr.

Jorge J. Rocca

Mario C. Marconi

Copyright by Samuel R. Ronald 2023

All Rights Reserved

ABSTRACT

INVESTIGATION OF LASER COOLING AND TRAPPING OF ATOMIC SILICON: TOWARDS THE DEVELOPMENT OF A DETERMINISTIC SINGLE ION SOURCE

The laser cooling and magneto-optical trapping of silicon atoms were investigated experimentally. These are the first steps towards the development of a deterministic single ion source suitable for single ion implantation of a Kane quantum computer. We identified the $3s^23p^2\ ^3P_2 \rightarrow 3s3p^3\ ^3D_3^o$ transition at 221.74nm as a cycling transition suitable for laser cooling. We also identified the $3s^23p^2\ ^1D_2 \rightarrow 3s3p^3\ ^3D_3^o$ at 256.26nm as a repump transition coupling a lower metastable state with the upper cooling state. Two deep ultraviolet (DUV) laser systems were implemented to provide the cooling and repump laser light. Both systems utilized two stage second harmonic generation to quadruple the frequency of a fundamental laser to produce the DUV light. The cooling laser system utilized frequency quadrupling of a tunable cw Ti:Sapphire ring laser to produce up to 90mW at 221.74nm. The repump laser system utilized frequency quadrupling of an external cavity diode laser to produce up to 35mW at 256.26nm.

A silicon atomic beam source operating at 1400°C was developed that produced a beam of free silicon atoms for laser studies. The atomic beam characteristics were analyzed, and the velocity distribution was manipulated via laser cooling. Careful spectroscopic studies were performed on the cooling and repump transitions. Frequency references for the DUV lasers were investigated in Te_2 and I_2 with Doppler free saturated absorption spectroscopy, using the first doubling stage output of the cooling and repump laser, respectively. Specific hyperfine components of the molecular transitions in Te_2 and I_2 , suitable for frequency references, were identified and measured. Locking of the cooling laser on the Te_2 reference was demonstrated.

A magneto-optic trap (MOT) was implemented in the silicon atomic beam. A CCD optical system to image the fluorescence from atoms in the MOT was developed and achieved single atom

detection capability. MOT trapping of silicon atoms was attempted. The low flux of atoms in the MOT velocity capture range precluded any observation of trapped atoms. A Zeeman slower, based on a novel design utilizing a variable pitch helical solenoid, was designed, simulated, and constructed to improve the flux of slow atoms. No magneto-optic trap was observed due to insufficient laser power for simultaneous Zeeman slowing and magneto-optic trapping.

Investigations were performed for one dimensional laser cooling, via a Zeeman slower, along the atomic beam motion direction. Atomic beam velocity distribution profiles were observed to be modified when the Zeeman slower was on. The parameter space of Zeeman slower currents, laser power and detuning, was explored. A simulation of the atom motion over the 1m long flight path under the influence of the Zeeman slower was carried out and found to agree with the observed results.

ACKNOWLEDGEMENTS

I first would like to thank my Doctoral Committee: Siu Au Lee, William M. Fairbank, Jr., Jorge J. Rocca, and Mario C. Marconi. This thesis was made much better from their input and I really appreciate the amount of time they spent in review.

Siu Au Lee is my advisor and friend and has my undying respect. Throughout my graduate career she continually opened doors and continued to show me new and interesting things and people. I am a different and better person from our interactions and much of my core self has been influenced by her. Thanks Siu Au :)

William M. Fairbank is my co-advisor and he is an absolute wizard. There were many times when we encountered progress absorbing problems that Bill stepped up and came up with quick, workable solutions. The $^{129}\text{I}_2$ identification presented here is his work. He is a very careful man and I only hope that I can live up to his standards throughout my career.

Tony Gorges was a postdoc in our lab early in my graduate studies and he motivated me much more than he knows. A few kind words that he said stayed with me throughout my career and I am not sure that I would be here without his encouragement early on.

Jon Gilbert was a lot of help in the lab during a time when we were doing a lot of building up of the project. His extra hands and extra thoughts were very helpful and I really enjoyed working with him.

Health Kippenhan and Jeff Lyons were undergraduates in the lab that built our heating oven for the tellurium cell. I modified it for PID feedback control once we began our spectrographic search in earnest, and I noticed how well it was built. It was something that needed very little attention from me during data runs and that was a great victory in and of itself.

Rob Scholten introduced us to the Variable Pitch Zeeman Slower and was very forthcoming with design tips from their lab. My interactions with Rob were always enjoyable and building the slower was a fun project.

Jan Hall is a delight to interact with and it was always incredibly motivating when he showed interest in my research. He helped us with a lot of consultation throughout the experiment as an old friend to Siu Au. I got to interact with Jan and his wife Lindy on a personal level several times and they are great.

Gerry Gabrielse allowed me to participate in the ATRAP collaboration and funded me on a trip to CERN to help establish a laser system for his project. Gerry works on really cool experiments with a lot of people and it was great to see how the inside of someone else's lab operates.

As always, behind all the science there are loads of friends and family that have given me lots of support. There are way too many people to name individually but I will strive to continue to show them how important they are to me now and in the future.

DEDICATION

I would like to dedicate this dissertation to my brother Lewis, my other half.

TABLE OF CONTENTS

ABSTRACT	ii
ACKNOWLEDGEMENTS	iv
DEDICATION	vi
LIST OF TABLES	ix
LIST OF FIGURES	x
Chapter 1 Introduction	1
1.1 Quantum Computers	1
1.2 The Kane Quantum Computing Architecture	3
1.3 Placement Techniques for the Kane Quantum Computer	5
1.4 Laser Cooled Single Ion Source	6
1.5 Feasibility of Laser Cooling of ³¹ Si	8
1.6 Statement of Thesis	10
Chapter 2 Theory	12
2.1 Silicon Spectroscopy	12
2.2 Laser Cooling and Trapping	16
2.2.1 Saturation Intensity	18
2.3 Atomic Beams	18
2.4 Zeeman Slower	20
2.4.1 Variable Pitch Helical Coil	24
2.4.2 Zeeman Slower and Trapping Simulations	25
2.5 Nonlinear Optics	30
Chapter 3 Experimental Apparatus and Techniques	37
3.1 System Overview	37
3.2 Silicon Atomic Beam	37
3.3 Variable Pitch Zeeman Slower	42
3.4 Trapping Chamber	44
3.5 Collection Optics and CCD	46
3.6 Laser Systems	52
3.6.1 Cooling Laser	53
3.6.2 Repump Laser	54
3.7 Saturated Absorption Spectroscopy	55
Chapter 4 Experimental Investigations and Results	58
4.1 Silicon Spectroscopy	58
4.2 Characterization of the Silicon Atomic Beam Source	61
4.2.1 Temperature Considerations	61
4.2.2 Atomic Flux Verification	62
4.2.3 Velocity Distribution Measurements	67

4.3	Frequency Control of the Cooling Laser System	69
4.3.1	Molecular Te ₂ Reference Investigation	70
4.3.2	Locking the Cooling Laser to the Tellurium Reference	72
4.4	Repump Transition Investigation	73
4.4.1	¹²⁹ I ₂ Spectra and Referencing the Repump Laser	75
4.5	Magneto-Optical Trap Investigation	77
4.6	Zeeman Slower Investigation	86
4.6.1	Zeeman Slower Initial Testing	86
4.6.2	Zeeman Slower Investigation with the Incorrect Polarization	92
4.6.3	Zeeman Slower Simulations	92
Chapter 5	Conclusions	99
Bibliography	102
Appendix A	Zeeman Slower Field Matching Maple Code	109
Appendix B	Molecular Iodine-129 Spectra	125
Appendix C	Zeeman Slower Python Simulation Code	131

LIST OF TABLES

2.1	Zeeman States	22
3.1	Zeeman slower parameters	42
3.2	Sensitivity at 1 MHz 16-bit Readout	49
4.1	Values Used for the Flux Calculation	66
4.2	Results for atomic beam flux measurements compared to expected values	67
4.3	Silicon Energy Levels for the Repump Transition, and their Uncertainties	73
4.4	Iodine-129 Spectroscopic Constants for Silicon Repump Transition Marker	76
4.5	Relevant Trap Parameters for Silicon	78
4.6	Loading and Loss Parameters for a Silicon MOT	81
4.7	Expected velocity changes in the Zeeman slower running with 120A	91

LIST OF FIGURES

1.1	Kane Quantum Computer Chip Schematic	3
1.2	Kane Gates	5
1.3	Ion Beam Phase Space	7
1.4	Single Ion Deposition	9
1.5	Silicon Isotope Shift	10
2.1	Silicon Energy Levels	13
2.2	Silicon Magnetic Sublevels of our Main Cooling Transition	14
2.3	Silicon Magnetic Sublevel Simulation Results	15
2.4	Spatial MOT Force	17
2.5	Molecular Beam Angular Distribution	20
2.6	Zeeman Slower Field Comparison	23
2.7	Variable Pitch Helical Coil Parameterization	25
2.8	1D Simulation Block Diagram	26
2.9	Simulated Zeeman Slower Velocity Changes for Different Laser Detunings	27
2.10	Trap Simulation Geometry Setup	28
2.11	Trappable Velocity Simulation Plot	28
2.12	Ballistic Trajectory Simulation Plot	30
2.13	Refractive Index Ellipse	33
3.1	Full Experiment Block Diagram	38
3.2	Silicon Oven Schematic	40
3.3	Silicon Velocity Distribution	41
3.4	Constructed slower mounted on a lathe	43
3.5	Top View of Trapping Chamber	44
3.6	Permanent Magnetic Field Coils	46
3.7	CCD collection optics design schematic	47
3.8	Blackbody spectrum of our collection optics setup.	48
3.9	UV filter transmission	48
3.10	Images to determine the depth of field and focus of the CCD optics.	50
3.11	CCD Quantum Efficiency and UV Filter Transmission	51
3.12	Silicon Energy Levels	52
3.13	External Cavity Diode Laser Schematic	54
3.14	Saturated Absorption Spectroscopy Setup	56
4.1	Transverse Beam Geometry	59
4.2	Transverse Silicon Fit	60
4.3	Misaligned CCD Spectra	63
4.4	Beam Flux Verification Spectra	65
4.5	Atomic Beam Geometry in the Horizontal Plane	68
4.6	Silicon Atomic Beam Velocity Fit	69
4.7	Tellurium and Silicon Offset Analysis	70

4.8	Te ₂ Spectra	71
4.9	Te ₂ Lock Signal	72
4.10	¹²⁷ I ₂ Spectra	75
4.11	¹²⁹ I ₂ Reference Spectra	77
4.12	Repump Laser Geometry	83
4.13	Typical Zeeman Slower Testing	87
4.14	Initial Zeeman Slower Test	89
4.15	Interesting Zeeman Slower Spectra	90
4.16	Experimental Zeeman Current Dependence	93
4.17	Experimental Zeeman Power Dependence	94
4.18	High Power 120A Zeeman Simulation Results	95
4.19	High Power 90A Zeeman Simulation Results	96
4.20	High Power 60A Zeeman Simulation Results	97
4.21	Low Power 60A Zeeman Simulation Results	98

Chapter 1

Introduction

1.1 Quantum Computers

Richard Feynman proposed the idea of a Universal Simulator in 1982. [1] His simulator would yield an exact solution for a physical problem and would be indistinguishable from the physical system it was simulating. It could be used to perform experiments and test physical laws. He began with the idea that simulating physics with classical computers relies on using classical approximations usually described by local differential equations. However the physical world is quantum mechanical, and any full simulation would need to incorporate the simulation of quantum mechanics. One way to realize this type of simulation would be to incorporate quantum objects as the building blocks of such a system. He proposed a Quantum Computer as a Universal Quantum Simulator, a new kind of computer that could more readily simulate certain problems that were difficult for conventional classical computing.

Feynman went on to say that "it does seem to be true that all the various field theories have the same kind of behavior, and can be simulated in every way, apparently, with little latticeworks of spins and other things." Feynman proposed using spin-1/2 systems as the basis for the Quantum Computer, and much of the current research relies on spin-1/2 systems to test quantum algorithms. The quantum bit, or qubit, is the fundamental component of the quantum computer. In contrast to the classical bit, which can only represent a 1 or a 0, qubits can be put in superposition states and entangled to drastically increase the parallelism of calculations.

In order to perform calculations we need to be able to individually address our qubits in order to initialize a starting state and we need to be able to allow those qubits to interact with each other. These two processes are usually referred to as single-qubit and two-qubit operations. Universality shows that any multi-qubit operation can be decomposed into single- and two- qubit operations. [2, 3]

In 1994, Peter Shor devised an algorithm based on quantum computation that given an integer could find its prime factors exponentially faster than any classical algorithm. [4] This sparked enormous interest in the quantum computer because the algorithm could be used to drastically decrease the time needed to decipher encrypted messages, particularly the RSA encryption commonly used in internet commerce. This would have drastic impacts for both national security and internet safety.

Another algorithm devised by Grover in 1997 would allow for searches through unstructured databases quadratically faster than any classical algorithm. [5] There are now a myriad of quantum algorithms that will be useful to speed up computation times for certain problems when compared to classical computers. Quantum supremacy was claimed by Google AI Quantum in late 2019 by performing a task in 200 seconds that would take a state-of-the-art classical supercomputer 10,000 years. [6] Subsequently IBM scientists analyzed the findings and argue that a classical system could perform the calculation in less than 2.5 days. [7]

Another application in fundamental research that has seen increased attention is the simulation of molecular properties. The ground state energies of small molecules, such as H_2 and LiH , can be simulated with just a small number of qubits. [8,9] Hartree-Fock electronic structure calculations have been performed that show it is possible to achieve chemical accuracy when combined with error correcting techniques. [10]

Quantum Computation and Quantum Information have become robust fields with researchers contributing from across the world. There are many different experimental systems under active research as candidates for a usable Quantum Computer. The most mature systems are those that utilize spin states of trapped ions and magnons in superconducting Josephson junctions as qubits. [10, 11] There are photonic systems that rely on the polarization state of single photons to be realized as qubits. [12] There are quantum dot systems that rely on tailored quantum dot states to be realized as qubits. [13] There are ionic and neutral atomic trapping systems that use various candidates for qubits, including the intrinsic spin states of either an electron or nucleus as the qubit. [14] There are superconducting systems that use magnons inside Josephson junctions

as qubits. [15] There are even micromechanical systems that use drum head modes on a surface as qubits. [16] Each system comes with its own weaknesses and strengths, and these systems and many more are used to perform tests on quantum computational theories.

1.2 The Kane Quantum Computing Architecture

In 1998, Bruce Kane proposed an all solid state quantum computing architecture based on very precise placement of single phosphorus dopants in a silicon lattice. [17] This all solid state architecture is an attractive design due to the reduced overhead needed to run a system when compared to typical laboratory setups, which often require extensive vacuum and optical systems. In addition, it could rely on the extensive silicon fabrication techniques developed over the last 75 years.

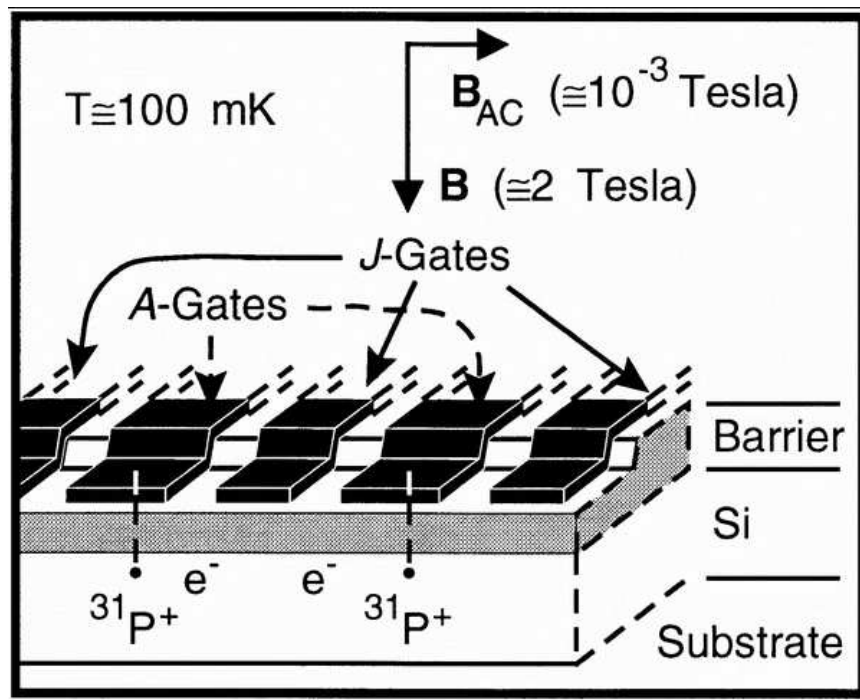


Figure 1.1: Kane Quantum Computer Chip Schematic: The Kane Quantum Computer is based on the precise placement of Phosphorus donors in a silicon substrate. Voltage gates above deposition sites control single qubit interactions while gates between sites control coupling. A large constant magnetic field splits the energy level degeneracy and transitions are performed with a transverse AC magnetic field.

A schematic for the design is shown in Figure 1.1. An array of single $^{31}\text{P}^+$ dopant atoms (nuclear spin = $\frac{1}{2}$) are embedded in an isotopically enriched silicon lattice. Each $^{31}\text{P}^+$ nuclear spin acts as a qubit, and the entanglements are initiated and read out by electrons via hyperfine interactions. Control of the qubits is done by varying the voltages of gates on the silicon surface. A static magnetic field breaks the magnetic state degeneracy giving pure states to act as individual qubits at each dopant site. Cryogenic temperatures are needed in order to allow for operation in the ground spin manifold without thermally populating higher states. Transitions are driven via a transverse RF magnetic field. Each dopant will have a voltage gate above the site, designated as A-gates. The voltage on these A-gates will deform the electron cloud around the dopant, which will change the resonant transition conditions as shown in Figure 1.2a. This can be used to give each qubit individual addressability and allow for single qubit operations. The J-gates, found between dopant sites, are used to couple neighboring qubits together allowing for 2-qubit operations, shown in Figure 1.2b. With this setup, either the nucleus of the dopant or the localized electron cloud may be utilized as the qubit. A possible usage scenario could use the electron spin states as qubits during operations, in order to take advantage of the faster transition rates, and to use the dopant nuclear spin states as a storage register, to take advantage of the long coherence times of the nucleus. Shift registers can be made to transfer a particular qubit state via electron transfer to different parts of the chip for further manipulation or readout.

Readout would depend on single electron transistors. Kane proposed a method of measuring the spin state non-destructively, based on the Coulomb interaction with the transistor base region. [18] Utilizing this non-destructive readout, a spin refrigeration technique can be performed where electron spin states above the ground state would be rejected. This would give an effective spin temperature that would be much lower than the temperature of the chip, allowing for operation at higher cryogenic temperatures.

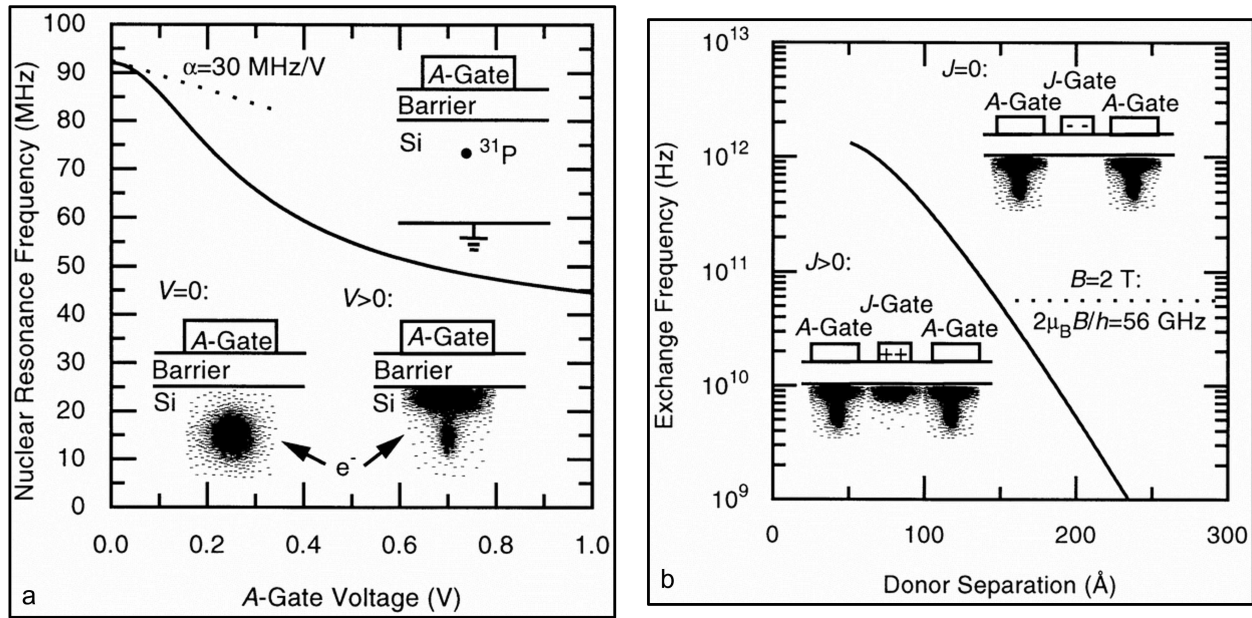


Figure 1.2: Kane Gates: In figure a we see how the single qubit resonant frequency changes as voltage is applied to the A gates. Figure b shows the operation of the J gates, used to couple neighboring qubits.

1.3 Placement Techniques for the Kane Quantum Computer

The challenge for the Kane quantum computer concept is the placement of single ^{31}P ions with a spatial precision of ~ 1 nm. One approach is to use low dose ion implantation in conventional ion beam techniques. However the low dosage ion number is Poissonian in nature and results in a “hit and miss” in the number of implanted ions. In addition, in order to reach nanometer precision in a standard focused ion beam system, an accelerating voltage of 10-20 kV is often needed. These accelerating voltages can cause damage of the substrate, and can have implantation depth variations on the order of micrometers. Much effort has gone into how to detect single ion implantation and how to control the deposition depth. Most notable are the efforts by the Jamieson group at the University of Melbourne and the Clark group at the University of New South Wales. [19] In their method, a track of isotopically pure silicon-28 is sandwiched between section of boron doped silicon that acts as a current channel. As an ion is accelerated into the pure substrate using an ion beam, an inductive readout on successful deposition is performed using the doped channels. In order to reduce the interaction volume of impinging ions, they introduce a photoresist mask

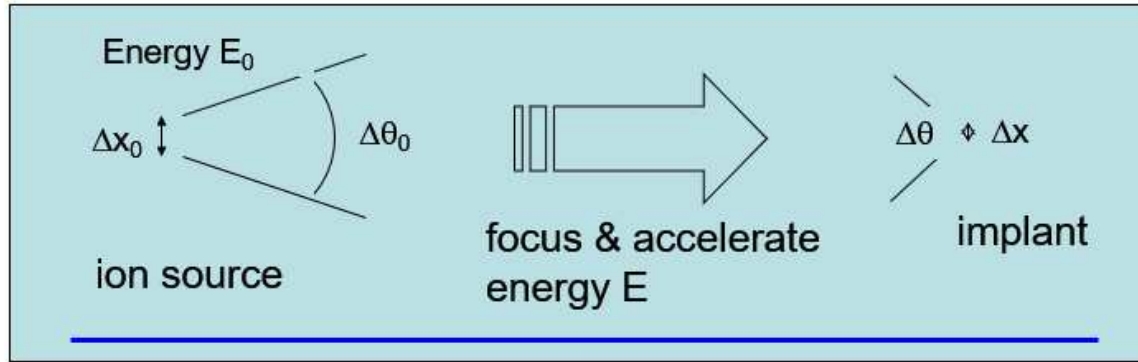
over this section and burn 10nm holes into the mask using an electron beam spaced at regular intervals. Ions that impact this resist layer are completely absorbed and do not diffuse into the substrate. Ion impacts are further confirmed from an x-ray signal given off when an ion impacts a site in the substrate. Once the sample is prepared, they use a low flux broad ion beam and wait for ion impact signals. They have recently achieved two and three qubit devices and performed quantum computing operations that have excellent spin coherence times and high fidelities. [20] The scalability of the technique to larger number of qubits is underway.

The Simmons group at the University of New South Wales has pioneered a novel deposition technique. [21] In their method, a silicon substrate is passivated with a single layer of hydrogen. Using a scanning tunneling microscope tip they selectively remove single hydrogen atoms from the surface at deposition sites. This is followed by introduction of phosphine (PH_3) gas and an annealing step that injects the phosphorus atom and ejects a silicon atom from the deposition site. The sample is then overgrown with silicon followed by the deposition of voltage gates. Readout is performed with single electron transistor methods. A two qubit quantum gate was demonstrated in 2019. [22] Recent published results from their samples have show excellent spin coherence times over $250\mu\text{s}$ with fidelities of 99.9%. [23]

1.4 Laser Cooled Single Ion Source

As mentioned above, the main challenge of a Kane quantum computer is the deterministic placement of single P ion into a Si substrate, with nanometer precision. An ion source utilizing laser cooling and trapping a single atom, followed by resonance ionization at threshold and delivering the ion to the substrate at low energy, will have the potential of fulfilling the requirements of the Kane quantum computer. This technique allows for control over the production of single ions “on demand.” [24]

In properly designed ion beam optics, how well one can focus a circular beam can be predicted based on “phase space” conservation. [25] The concept is shown in Figure 1.3. Typical conventional ion source would have $E_0 \sim 10\text{eV}$. In order to have a small spatial position $\Delta x \sim \text{nm}$ at the



$$\text{phase space} = \Delta x_0 \Delta \theta_0 \sqrt{E_0} = \Delta x \Delta \theta \sqrt{E}$$

Want $\Delta x \sim 1 \text{ nm}$, $E \sim 100 \text{ eV}$
 $\Rightarrow \Delta x_0$ and E_0 must be extremely small
 \Rightarrow ions must be confined and extremely cold

Figure 1.3: Ion Beam Phase space: Schematic of the conserved phase-space volume. We will need to have a tightly confined source in order to implant ions with low energy and the required spatial resolution.

implantation site, conventional ion beam deposition would require $\sim 10\text{keV}$ acceleration. However these accelerating voltages are often destructive to the surface of the substrate, and they can have implantation depths on the order of micrometers. By contrast, a laser cooled ion source has an extremely small initial energy due to its low temperature: $E_0 \sim 100\mu\text{K} \sim 10^{-8}\text{eV}$. The energy factor translates into a phase space advantage of more than 4 orders of magnitude in focusing power over a conventional ion source with the same initial Δx_0 . For practical purposes, implantation of ions with $E \sim 100\text{eV}$ is desired to avoid substantial spreading during implantation.

Jabez McClelland and his group at NIST Gaithersburg showed that a magneto-optic trap ion source (MOTIS) has the lowest phase space when compared to any other ion source. [24] The NIST group pioneered a technique that can produce a single chromium atom on demand in a magneto-optical trap (MOT). [26, 27] In a MOT, six counter propagating laser beams are tuned so the light field reduce momentum of atoms in the overlap region. A quadrupole magnetic field provides a spatial trapping force and causes the atoms to move towards the zero point of the field. This provides a spatially confined cold source of atoms. The MOT technique can be used to trap a single atom. McClelland used a fast feedback loop that turns off the loading of the trap

when a single atom is detected by high efficiency fluorescence. A single cold ion is produced by resonant photoionization and extraction of the trapped atom using conventional charged particle beam optics. Photoionization at threshold does not impart any extra momentum to the cooled atom. This is followed by low energy implantation that prevents crystal damage and ion straggling under the surface of the substrate.

The ground state cooling transition for magneto-optical trapping of phosphorus has a very short wavelength (178nm) that is not technologically viable with present day lasers. Our group at Colorado State University has found that silicon has a radioactive isotope, ^{31}Si , that beta decays to phosphorus in approximately 2.6 hours.



For atomic Si, the cooling laser wavelength is 221.74nm. The resonant ionization wavelength from the upper cooling state is 454nm. Both of these wavelengths are attainable with current technology.

A laser cooled single ion on demand Si source is under development at Colorado State University. The scheme is show in Figure 1.4. Our scheme is an extension of the work done by Jabez McClelland. [24, 26, 27] Our ultimate goal relies on the laser trapping of the isotope ^{31}Si which beta decays after implantation to phosphorus in the Si substrate. Once it is verified that a single atom is trapped, a resonance ionization laser pulse will be applied to photo-ionize the atom. The ion will be deposited with $\sim 100\text{V}$ of accelerating voltage and implanted into the substrate.

1.5 Feasibility of Laser Cooling of ^{31}Si

The laser cooling and trapping of neutral Si atoms require a suitable optical transition such that the atoms can repeatedly interact with the laser photons. The $3s^23p^2\ ^3P_2 \rightarrow 3s3p^3\ ^3D_3^o$ transition at 221.74nm is chosen as the cooling and trapping transition. The $J \rightarrow J + 1$ transition is attractive since it allows laser polarization gradient cooling in addition to the usual Doppler cooling, and the

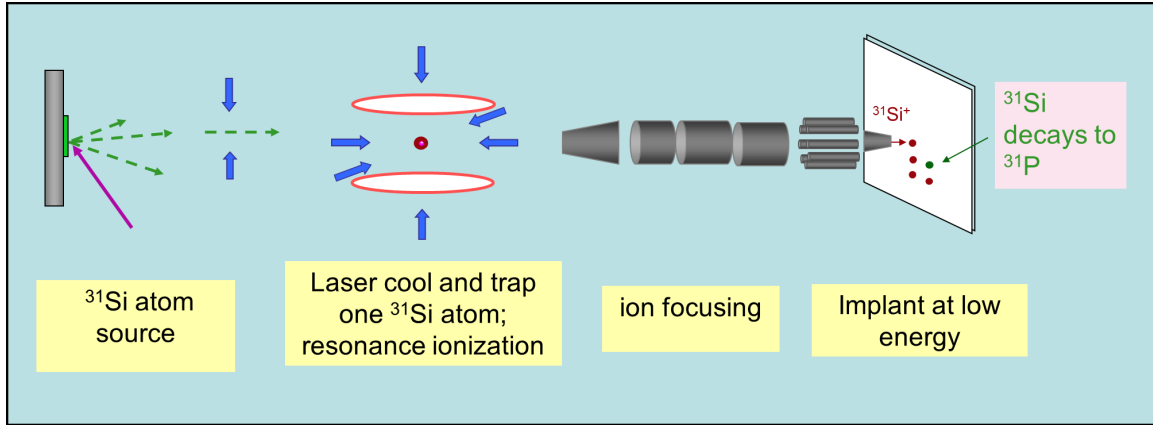


Figure 1.4: Single Ion Deposition: We propose using laser cooling techniques and resonant ionization in our scheme for precise control over our ion source. This control will enable us to have sub-nm deposition fidelity.

atoms can be cooled to much below the Doppler limit. To assess the feasibility of laser cooling of ^{31}Si , our lab has measured the isotope shifts of the cooling transition for the three stable silicon isotopes, Si-28, 29 and 30, and the hyperfine splitting of Si-29. [28] The spectrum is shown in Figure 1.5. From this measurement we were able to deduce the isotope shift and hyperfine structure of the Si-31 atom. The predicted position of the Si-31 cooling transition relative to the stable isotopes is shown on the right side of Figure 1.5.

Laser cooling requires that the laser be "red" detuned (lower frequency) from the center of the transition to achieve cooling. Atoms that encounter a laser with "blue" detuning (higher frequency) are heated and ejected from the trapping region. The conditions for the trapping of ^{31}Si are favorable due to the fact that the transition wavelength of ^{31}Si is shifted to the blue of the other isotopes. See Figure 1.5.

Spectroscopy on levels near the ionization limit in ^{28}Si has been performed in our lab but has yet to be published. [29] We found a collection of suitable states for resonant photo-ionization from the upper cooling level using a pulsed dye laser at 454nm.

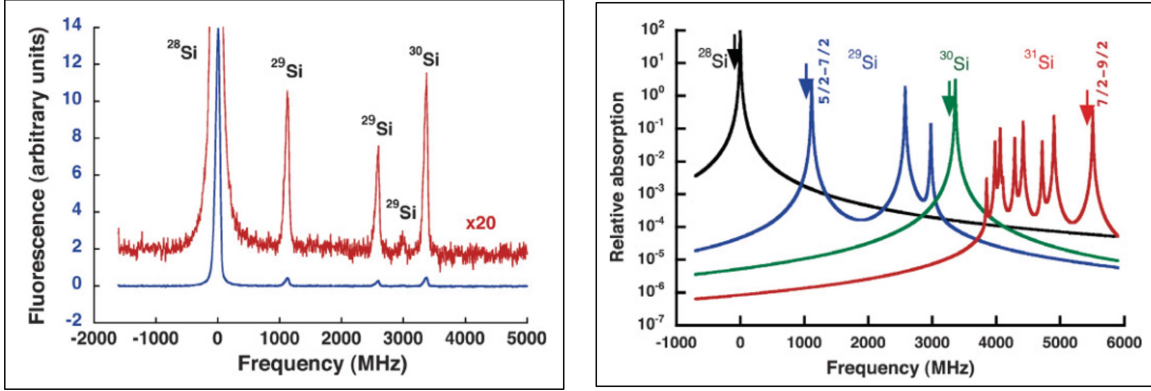


Figure 1.5: Silicon Isotope Shift: On the left is our experimentally observed isotope spectra. On the right is the calculated absorption spectra. The arrows show the approximate frequencies for laser cooling and trapping of the different isotopes. [28]

1.6 Statement of Thesis

Our ultimate goal is to implement a single ion on demand source as shown in Figure 1.4. My thesis research is to investigate the laser cooling and trapping of the stable ^{28}Si isotope, as a first step towards achieving this goal.

In Chapter 2, I will review the theory used in performing my experiments. I will start by discussing the silicon spectroscopy and level structure. I will then present an overview of laser cooling and trapping as well as the technique that we use to cool neutral atoms. I will discuss molecular beam theory needed in order to characterize our atomic beam setup. I will follow with the theory behind the Zeeman slower technique and present the mathematics needed to properly design our slower. I will finally present the theory of nonlinear optics used in our laser systems to generate the deep ultraviolet wavelengths.

In Chapter 3, I will present the experimental equipment used during my research. I will begin with an overview of the entire system. I will introduce the evolution of our silicon atomic beam system. Next I will show the design and construction of our Variable Pitch Zeeman Slower. I will present our trapping chamber, the laser beam geometry and the magnetic field we use in the system. I will present our collection optics system and the system we used in order to ensure we were focusing on the correct position for the trap point. The CCD setup will be presented next and

I will show how we calculate the number of photons emitted in the trapping chamber. Next I will present our laser systems at 221nm and 256nm, and the saturated absorption spectroscopy setup used to obtain reference spectra for our laser systems.

In Chapter 4, I will discuss our experimental investigations and results of the experiment. I will present our silicon spectra and show how we use it to characterize our atomic beam in various ways. I will show how we can use the spacial images on the CCD camera to verify the correct placement of our atomic and laser beams in the trapping region. I will show spectra from a natural isotopic abundance tellurium cell from the saturated absorption setup as well as how we reference that to the main silicon transition. I will show how we used an $^{129}\text{I}_2$ cell as an absolute reference and present the calibration spectra that we used in order to reference our repump laser. I will then outline our attempts at creating a magneto-optical trap for silicon and the difficulties that we encountered. I will finally present some interesting spectra that we obtained while testing our Zeeman slower. Simulations were performed that match well with our observations and show that we are able to drastically change the velocity distribution with our systems.

In Chapter 5, I will summarize the accomplishments of my investigations.

Chapter 2

Theory

Our scheme relies on the development of several systems, including a source of ^{31}Si , deep ultraviolet (DUV) lasers to cool the atoms, a magneto-optical trap (MOT), spectrographic studies for autoionizing states, and an ion beam focusing system. The focus of this thesis is to investigate the laser cooling and magneto-optical trapping of silicon atoms. For this thesis research we study the creation of a trap with the most abundant natural isotope ^{28}Si .

The theoretical framework for implementation and analyzing the MOT experiment is presented in this chapter. Section 2.1 discusses the ground state and magnetic level structure of ^{28}Si , including characteristics that are important to the MOT. Section 2.2 introduces the optical scattering force for a two level system, and how this force can be utilized to trap and cool a sample of atoms. Section 2.3 considers the theory of an effusive oven beam source, and relevant parameters for operation and analysis. Section 2.4 derives the equations needed for the construction and implementation of a Zeeman slower, a device used for increasing the flux of slow, trappable atoms from the atomic beam source. Section 2.5 goes over the theory of nonlinear optics, with a focus on second harmonic generation (SHG), a technique that is needed for reaching the wavelengths relevant to address the silicon ground state manifold.

2.1 Silicon Spectroscopy

Silicon is a Group 4 element with atomic number 14. Its ground state configuration is $3s^23p^2$ $^3P_{0,1,2}$. The most abundant stable isotope is ^{28}Si (92.23%), which is the focus of this work. With 14 neutrons and 14 protons, this isotope has no nuclear spin and therefore no hyperfine interaction to address in the level structure. A diagram of the lower lying silicon levels is shown in Figure 2.1. [30] The $J=2$ level of the ground state manifold used for our lower state sits at 223.157cm^{-1} above the $J=0$ state and is populated thermally at our oven operating temperature. As will be discussed later, Doppler laser cooling requires a cycling transition. The $3s^23p^2$ $^3P_2 \rightarrow 3s3p^3$ $^3D_3^{\circ}$

is such a transition that is reachable with a DUV laser at 221.74nm. The spontaneous emission coefficient is $4.54 \times 10^7 \text{s}^{-1}$, corresponding to an excited state lifetime, $\tau = 22\text{ns}$. [30]

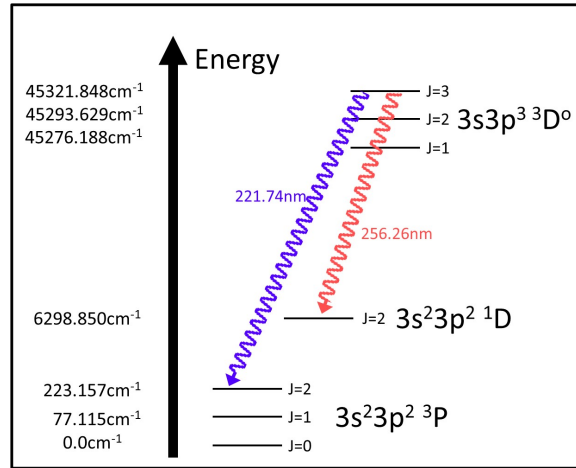


Figure 2.1: Silicon Energy Levels: The blue represents our main cooling transition. There is a small coupling from our excited state to the ¹D₂ metastable state, with a theorized branching ratio of $\sim 1:5700-7200$. [31–33]

From this excited state there is a possible weak decay path to the ¹D₂ metastable state. This transition has never been directly observed. The rate of this transition was calculated using multiconfiguration Hartree-Fock (MCHF) numerical techniques and published by NIST. [33] This model is capable of making estimates of the emission coefficients for different allowed transitions. The MCHF calculation identified both an E1 and an M2 component for the weak transition, with the transition rates equal to $6.28 \times 10^3 \text{s}^{-1}$ and $4.25 \times 10^{-3} \text{s}^{-1}$ respectively. Using the model's A coefficients for our cooling transition ($3.58 \times 10^7 \text{s}^{-1}$) we find a branching ratio of 1:5700 for the upper state. Our main cooling transition is well known and has been measured experimentally. [32] Using the emission coefficient from this work for our main cooling transition ($4.54 \times 10^7 \text{s}^{-1}$) and the theoretical rate for decay to the ¹D₂ state we find a branching ratio of $\sim 1:7200$. If left unaddressed then this would be a major loss for the trap and reduce the trap lifetime. It is worth noting that in the NIST tables [30] as well as the most recent transition probabilities compilation published by

Magnetic Sublevels and Transition Probabilities

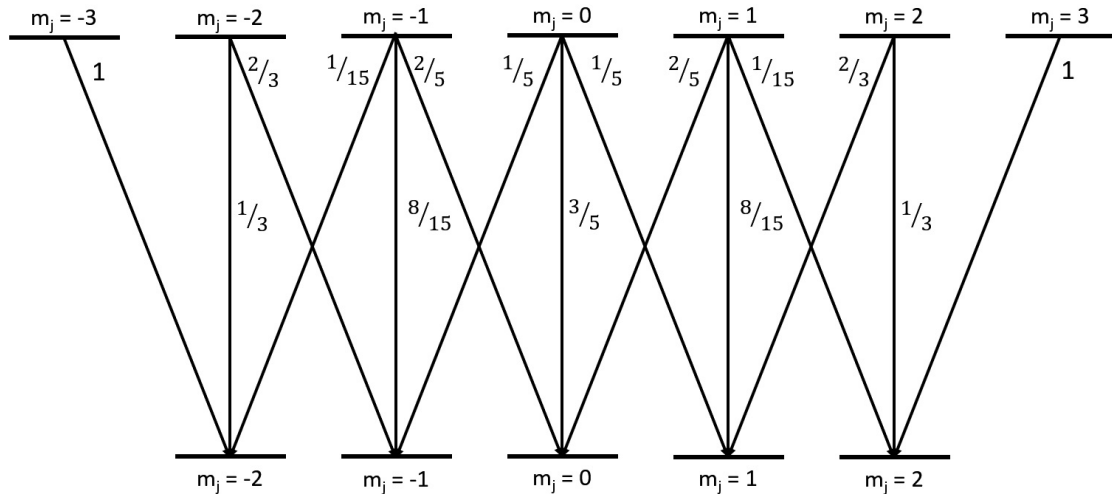


Figure 2.2: Silicon Magnetic Sublevels of our Main Cooling Transition: A diagram of the Zeeman splitting of our main cooling transition. The numbers represent the square of the Clebsch-Gordon Coefficients.

NIST, [34] the E1 transition was inadvertently omitted and only the M2 transition is listed. Using the emission coefficients from the M2 transition makes this branching ratio negligible.

Since these states have nonzero angular momentum, the levels will be split in the presence of a magnetic field due to the Zeeman effect, the details of which are discussed in Section 2.4. The states are summarized in Figure 2.2. The lower state with $J = 2$ has 5 magnetic sublevels, and the upper state with $J = 3$ has 7. Linearly polarized photons will drive transitions with $\Delta m = 0$ and is referred to as π -polarized. When exciting with these photons the substate population will tend to coalesce near the $m = 0$ state due to the higher Clebsch-Gordon coefficients near the $m=0$ state. Circularly polarized photons can drive transitions with $\Delta m = \pm 1$ depending on the helicity of the photon. If the helicity of the photon is in the direction of the magnetic field, then transitions will add quanta of angular momentum to the state, giving $\Delta m = +1$. If the helicity is reversed, then transitions will give $\Delta m = -1$. These are referred to as σ^+ and σ^- photons, respectively. The σ^+ photons are always driving the transition increasing the angular momentum and the atoms will be

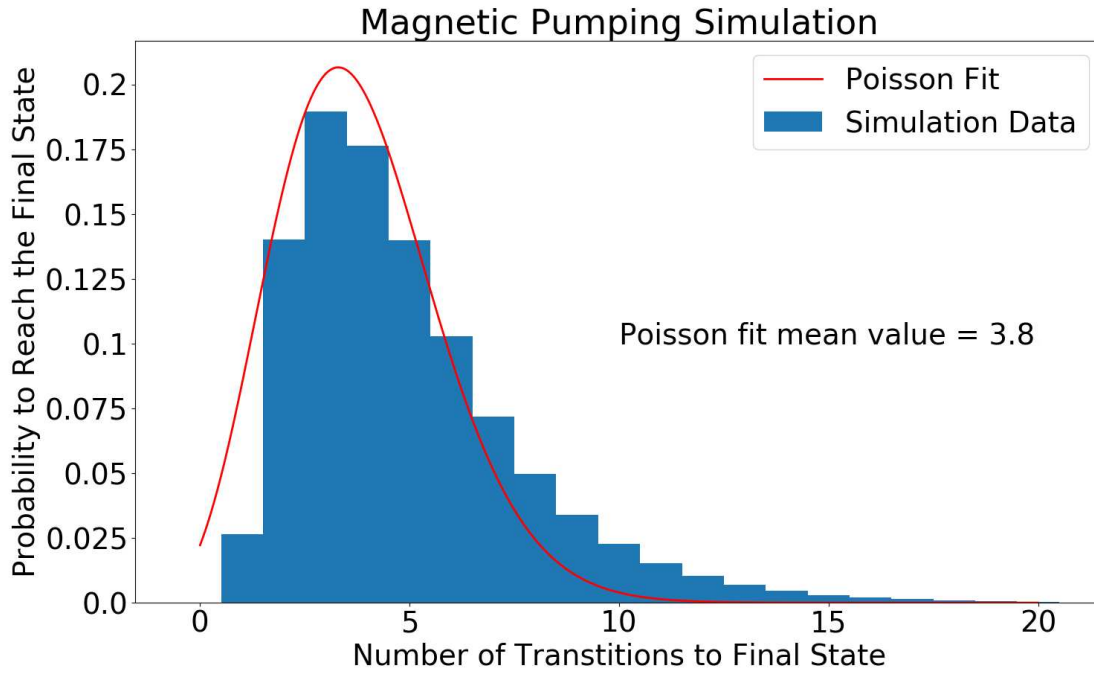


Figure 2.3: Silicon Magnetic Sublevel Simulation Results: This plot shows how many transitions it takes for an atom starting in the $m_j = -2$ ground state to end up in the $m_j = +2$ ground state using σ^+ polarized photons. At this point the atom can be treated as a 2-level system. Note that if on resonance this process happens very fast ($\sim \mu s$), however if the atom scattering rate is low based on the environment or laser parameters, these transitions have the potential to take a much longer time. While this process does not inherently follow a Poissonian distribution, a Poissonian fit was calculated for comparison.

guided to the $m_j = 2 \rightarrow m_j = 3$ transition where they will remain. Once in this state we can treat the system as a simple 2-level transition. The same process will work in the case of driving $\Delta m = -1$ transitions towards the $m_j = -2 \rightarrow m_j = -3$ transition. It does not take very long to drive the atom into this condition. Figure 2.3 shows a simulation of this process with an atom initially in the $m_j = -2$ ground state. It tracks how many transitions it will take to be guided into the $m_j = 2 \rightarrow m_j = 3$ state, using a random number generator to simulate the probabilistic nature of the decay process. This histogram shows the normalized distribution for a sample of 1 million atoms starting in the $m_j = -2$ state. From this distribution, there is a 90% probability that an atom will be pumped into the final state after 8 transitions.

2.2 Laser Cooling and Trapping

Laser cooling and trapping relies on using near-resonant photons to excite and manipulate atoms and molecules. Since the photon has momentum, $\vec{p} = \hbar\vec{k}$, a particle that absorbs a photon undergoes a recoil in the direction of the photon travel. The emission process is isotropic and over many transitions averages to a net velocity change of zero. The velocity change imparted by a single photon absorption is called the recoil velocity and its magnitude is $v_r = \frac{\hbar k}{M} \equiv \frac{h}{\lambda M}$, where M is the mass of the particle. The steady state scattering rate for an atom in a two-level system is given by [35]:

$$R_{scat} = \frac{\Gamma}{2} \frac{I/I_{sat}}{1 + I/I_{sat} + 4\delta^2/\Gamma^2} \quad (2.1)$$

where Γ is the natural transition linewidth, equal to the inverse of the excited state lifetime, I is the intensity of the light, I_{sat} is the saturation intensity discussed in Section 2.2.1, and δ is the total detuning from resonance from all sources, such as the laser detuning, the atomic velocity, and the local magnetic field strength. This rate times the photon momentum gives us the scattering force.

The first demonstrations of laser cooling of neutral atoms were done with a single laser utilizing the Zeeman effect. [36] The modern version of this technique is outlined in detail in Section 2.4. After light force manipulation of atoms was observed, research moved to 3D confinement of neutral atoms. Initial work began with a technique called optical molasses [37]. In this scheme, three orthogonal pairs of counter-propagating laser beams are detuned below resonance. As an atom approaches a laser beam, it absorbs a photon that is Doppler shifted into resonance and receives a momentum kick in the direction of the laser (opposite of the atomic motion). It then will emit a photon on resonance in a random direction. This process is repeated over many cycles, giving the net effect of damping the atomic motion. This causes the atoms to move sluggishly through the intersection of the six lasers beams. Since this force is only proportional to the velocity of the atoms, we need another technique to give a spatially dependent force, and therefore confine the atoms. This confinement technique is known as a magneto-optic trap, or MOT. [38]

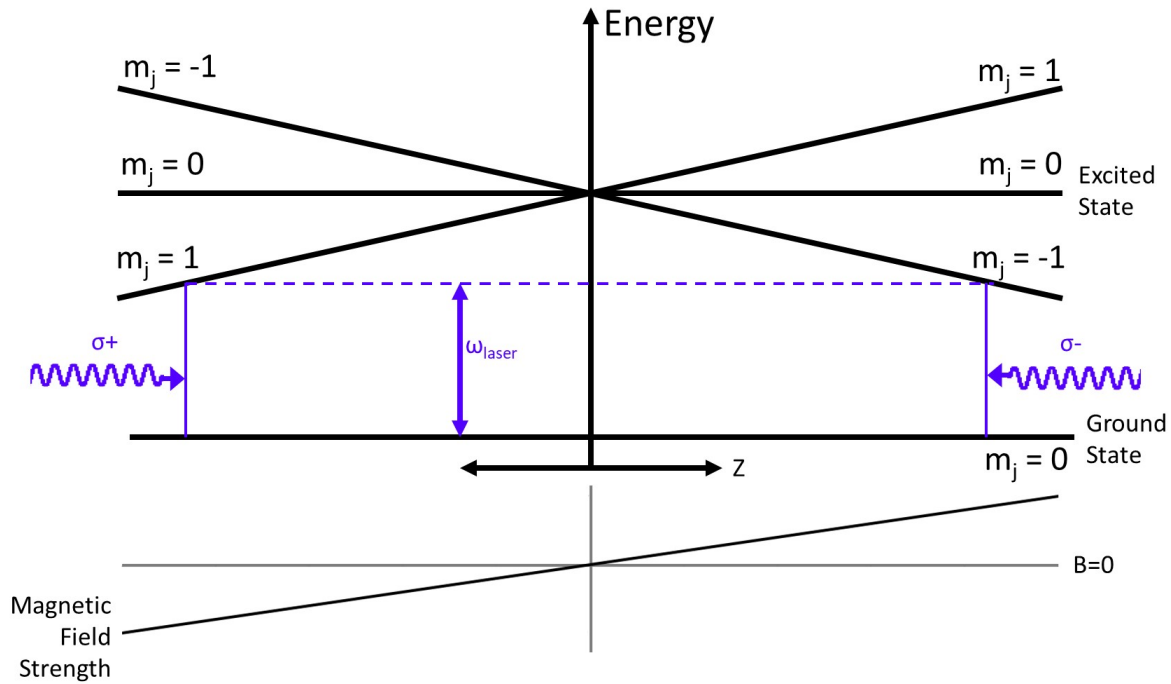


Figure 2.4: Spatial MOT Force: Atoms in the negative field region will preferentially scatter photons with $\sigma+$ polarization and receive momentum kicks towards the trap center. The same is true for $\sigma-$ scattering on the opposite side of the trap center.

As discussed in Section 2.1, circularly polarized light can be used to drive atoms into particular magnetic substates. If we create a spatially dependent magnetic field, then we can create a spatially dependent force based on this level splitting using circularly polarized light. A simple one dimensional schematic of this spatial dependence for a $J=0$ ground state and a $J=1$ excited state is shown in Figure 2.4. Atoms on the left side of the figure are subject to a negative magnetic field. σ^+ photons coming from the left side of the figure drive transitions to the $m_j = 1$ excited state and give momentum kicks towards the magnetic field zero. These photons are off resonant with atoms in the $m_j = 1$ state in the positive field region. The atoms pass through the magnetic field zero crossing and the magnetic substates become degenerate. As they enter the right side of the figure σ^- photons drive atoms into the $m_j = -1$ excited state and undergo transitions that give momentum kicks back towards the magnetic field zero. These photons are off resonant with atoms in the $m_j = -1$ state in the negative field region. As atoms pass through the magnetic field zero crossing the

behavior is reversed again. Utilizing this restoring force along all three spatial dimensions leads to confinement of atoms near the magnetic field zero.

2.2.1 Saturation Intensity

The saturation intensity for a given transition is defined to be the photon intensity which shortens the lifetime of the excited state by a factor of 2. [39] The expression for this is given by:

$$I_{sat} = \frac{h\nu}{\sigma\tau} \quad (2.2)$$

where h is Planck's constant, ν is the laser frequency, σ is the atomic absorption cross section, and τ is the excited state lifetime. Depending on the conditions of the experiment, the approximation for σ can take multiple forms. Following the standard convention we use the form for a simple two-level system [40]:

$$\sigma = \frac{3\lambda^2}{2\pi} \quad (2.3)$$

where λ is the transition wavelength.

With this in mind, our expression for the saturation intensity becomes:

$$I_{sat} = \frac{h\nu}{\left(\frac{3\lambda^2}{2\pi}\right)\tau} = \frac{2\pi hc\Gamma}{3\lambda^3} \quad (2.4)$$

Here we have used the expressions $\tau = 1/\Gamma$, where Γ is the natural linewidth of the transition and $\nu = c/\lambda$, where λ is the wavelength and c is the speed of light in vacuum. For the silicon cooling transition, the saturation intensity is $86.7mW/cm^2$.

2.3 Atomic Beams

Sources for atomic beams typically work by heating an element in an enclosure and allowing the atomic vapor to leave through a small aperture. The on-axis flux of atoms or molecules leaving a source with a thin walled aperture that reaches a detector area, A_d , is given by [41]:

$$\Phi = 1.118 \times 10^{22} \frac{PA_s A_d \text{ atoms}}{l_0^2 \sqrt{MT} \text{ second}} \quad (2.5)$$

where P is the vapor pressure in Torr, A_s and A_d are the source and detector areas in cm^2 , l_0 is the distance to the detector in cm, M is the atomic mass in amu, and T is the temperature in Kelvin.

Our system uses an atomic beam as the source for silicon atoms. If the pressure inside the oven is low enough so that there are negligible collisions as the vapor escapes, then that oven is considered an effusive source. Our source aperture is cylindrical in shape, 1mm in diameter and 2mm long, whose behavior is distinct from that of a thin-walled aperture or slit. Atoms attempting to leave the source at high angles will strike the wall of the aperture and have a much smaller chance of escaping, and those that do escape will do so at a different angle. This geometry will alter the angular distribution of the atomic beam while maintaining the same on-axis flux as that of a thin-walled source. The angular distribution for a source with $2r=L$ is shown in Figure 2.5. [41] Our source has a somewhat different geometry ($4r=L$) and we expect the distribution to be narrower.

In order to ensure that the oven is working in the effusive, or transparent, regime for this type of source, one must find the ratio of the mean free path, λ_m to the channel length, L . This ratio is called the Knudsen number, given by $K_n = \lambda_m/L$. For $K_n \gg 1$ we are ensured effusive flow. In practice $K_n \sim 1$ is found to have effusive flow for most purposes. [41] The mean free path is given by

$$\lambda_m = \frac{1}{n\sigma\sqrt{2}} = 7.321 \times 10^{-20} \frac{T}{P\sigma} \text{cm} \quad (2.6)$$

where n is the particle density, σ is the cross-section given in cm^2 , T is the absolute temperature in Kelvin, and P is the pressure of the local environment in Torr. For our experiment, $T = 1673\text{K}$, $P = 3.4 \times 10^{-4}$ Torr (the silicon vapor pressure at this temperature), and a typical collisional cross-section of $5 \times 10^{-16} \text{cm}^2$, we calculate a mean free path of ~ 800 meters. Therefore $K_n \sim 3.5 \times 10^5$ and we are always in the effusive regime.

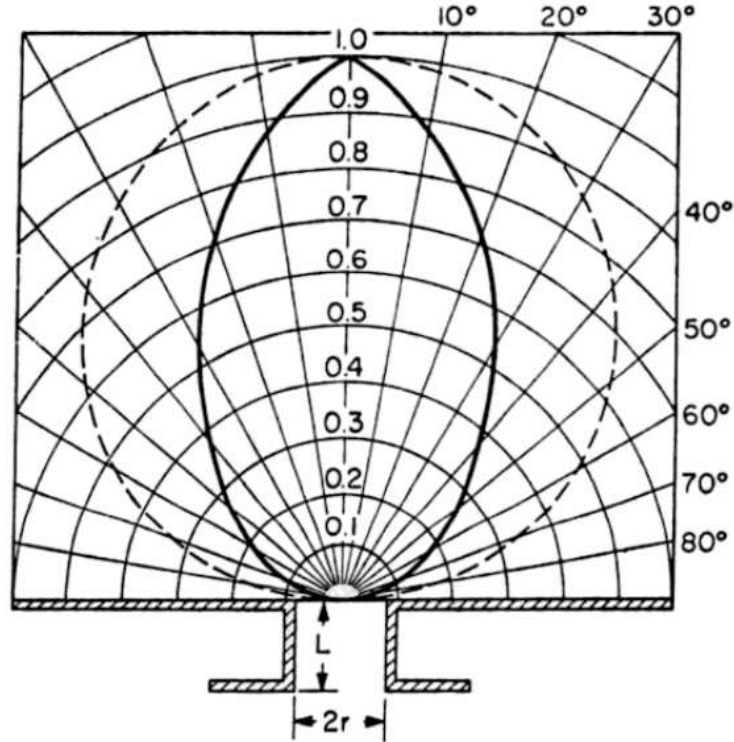


Figure 2.5: Molecular Beam Angular Distribution: The solid line is the distribution of atoms effusing from a channel whose diameter and length are equal. The dashed line is for a channel of negligible length. [41]

To first approximation, beams operating in the effusive regime follow a Maxwell-Boltzmann distribution function of the form

$$\rho(v) = 2 \left(\frac{m}{2k_B T} \right)^{3/2} v^3 e^{-\frac{mv^2}{2k_B T}} \quad (2.7)$$

where m is the mass, k_B is Boltzmann's constant, T is the absolute temperature, and v is the velocity. [41]

2.4 Zeeman Slower

Zeeman slower are used in atomic beam experiments where the goal is to increase the number of atoms available at low velocities. The distribution is controlled both by atomic parameters as well as the geometry of the system. In order to increase the number of atoms at low velocities, we use lasers and magnetic fields to populate the lower velocities from populations in higher velocities.

For any significant amount of slowing, we must keep our laser on resonance with these faster atoms for many transitions. We do this by matching the Doppler detuning of a constantly decelerating atom with a Zeeman detuning from a specially tailored magnetic field. First we define the laser detuning from the atomic resonance as $\Delta_0 = \omega_l - \omega_0$, where ω_l is the angular laser frequency and ω_0 is the angular atomic transition frequency. The Doppler shift of the transition is given by:

$$\delta_{Dop} = -\vec{k} \cdot \vec{v} \quad (2.8)$$

where k is the wavevector and v is the velocity. The Zeeman shift of an atomic transition is given by:

$$\delta_{ZE} = \frac{\Delta E}{\hbar} \quad (2.9)$$

where ΔE is the energy shift due to the Zeeman Effect and \hbar is Planck's constant divided by 2π . In general, the Zeeman energy shift is given by:

$$\Delta E = \mu_B B (g_e m_e - g_g m_g) \quad (2.10)$$

where μ_B is the Bohr Magneton, B is the magnetic field strength, g is the Landé g-factor of the state, m is the magnetic quantum number of the state, and the subscripts e and g represent the excited and ground states, respectively. The Landé g-factor can be calculated using:

$$g_J = g_L \frac{J(J+1) - S(S+1) + L(L+1)}{2J(J+1)} + g_S \frac{J(J+1) + S(S+1) - L(L+1)}{2J(J+1)} \quad (2.11)$$

where g_L is the electron orbital g-factor, g_S is the electron spin g-factor, L is the orbital angular momentum quantum number, S is the spin angular momentum quantum number, and J is the total angular momentum quantum number. For our case, we have $g_L \approx 1$ and $g_S \approx 2$ which simplifies the equation to:

$$g_J \approx \frac{3}{2} + \frac{S(S+1) - L(L+1)}{2J(J+1)} \quad (2.12)$$

Table 2.1: Zeeman States: This table shows relevant parameters used in our Zeeman energy shift calculation for use with the Zeeman Slower.

	Ground State	Excited State
Term Symbol	3P_2	${}^3D_3^o$
L	1	2
S	1	1
J	2	3
g_J	$\frac{3}{2}$	$\frac{4}{3}$
m_J	2	3

We choose to use σ^+ light for our slower. The states used for our system are summarized in Table 2.1, giving $\Delta E = \mu_B B$. Using Equation 2.10 to solve Equation 2.9 for the magnetic field; for an atom counter propagating a laser at a velocity, v , we have a magnetic field expression:

$$B = \frac{\hbar}{\mu_B} (\Delta_0 + kv) \quad (2.13)$$

By keeping the atom on resonance, we assume that the atom will decelerate adiabatically, which allows us to model the motion using simple kinematics. Consider the case of constant deceleration, a , of an atom from initial velocity v_0 , the velocity v of an atom at a location z would be given by:

$$\begin{aligned} v(z) &= \sqrt{v_0^2 - 2|a|z} \\ &= v_0 \sqrt{1 - \frac{2|a|z}{v_0^2}} \\ &= v_0 \sqrt{1 - \frac{z}{L}} \end{aligned} \quad (2.14)$$

where $L = \frac{v_0^2}{2|a|}$ is the length of the Zeeman slower. Substituting this into Equation 2.13 gives us a field expression of the form:

$$B = \frac{\hbar}{\mu_B} \left(\Delta_0 + kv_0 \sqrt{1 - \frac{z}{L}} \right) \quad (2.15)$$

where v_0 is the optimized entrance velocity, z is the distance along the slower and L is the length of the slower. The ideal field is shown in Figure 2.6 in red. The blue is the field from the coil design program which was used for all of the simulations.

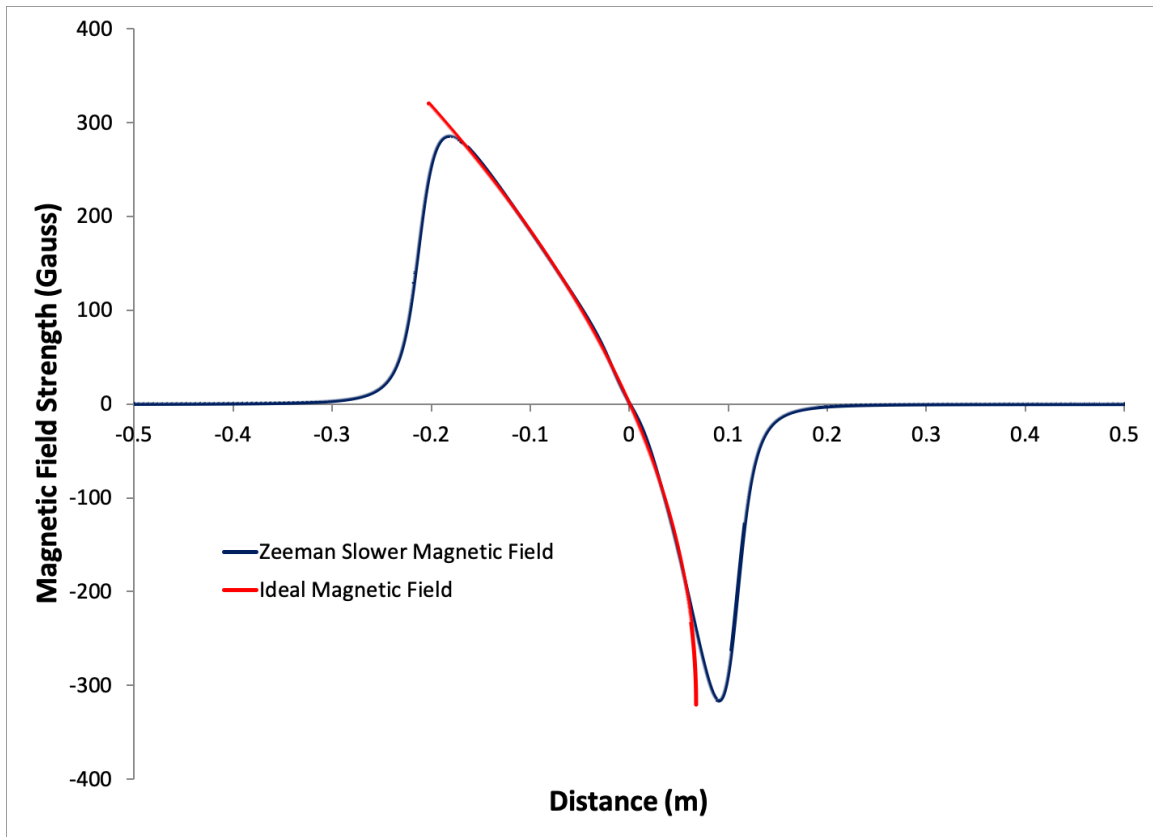


Figure 2.6: Zeeman Slower Field Comparison: Shown in red is the idealized magnetic field for adiabatic deceleration of an atom in a counter propagating laser field. In blue is the output of the coil design program that defined the coil winding used for the variable pitch Zeeman slower. The coil design field was used in all the subsequent simulation work.

The expected acceleration is defined using the scattering force acting on the atom by the laser. In order to ensure that the process proceeds adiabatically, we introduce a factor η between 0 and 1 to effectively give the atom longer time to scatter a single photon in a particular detuning region. This gives an expression:

$$a = \eta \frac{F}{m} = \eta \left(\frac{h\Gamma}{2m\lambda} \right) \left(\frac{s_0}{1 + s_0} \right) \quad (2.16)$$

where Γ is the transition linewidth, m is the atomic mass, and $s_0 = I/I_{sat}$ is the saturation parameter.

2.4.1 Variable Pitch Helical Coil

The Zeeman slower constructed in our lab uses a novel helical design developed by Professor Robert Scholten's Group. [42] Typical Zeeman slowers use many tapered layers of conductor in order to create a solenoid whose magnetic field matches the needed shape. Our slower is constructed by varying the spacing between the conductor in order to generate the field shape. This is done using a power series expansion of the winding parameter, $\theta(p)$, used in a parametric function used to describe a helical coil. The parametric equations for a helix take the form:

$$\begin{aligned} \vec{r}(p) &= [x(p), y(p), z(p)] \\ x(p) &= R \cos(\theta(p)) \\ y(p) &= R \sin(\theta(p)) \\ z(p) &= p \\ \theta(p) &= \sum_{n=1}^4 c_n p^n \end{aligned} \quad (2.17)$$

where R is the radius of the coil. To generate a good fit to the idealized field, the power series in the winding parameter $\theta(p)$ is taken to fourth order. The geometry of this parameterization is shown in Figure 2.7. The magnetic field of the slower is found by directly integrating over this

curve using the Biot-Savart Law. The Maple code used to fit and check the field matching is found in Appendix A.

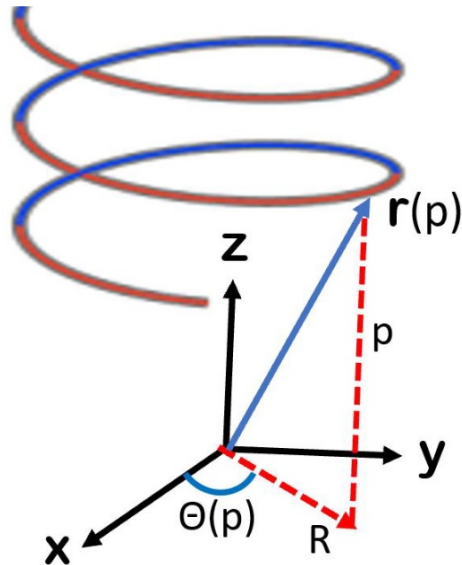


Figure 2.7: Variable Pitch Helical Coil Parameterization: This figure shows the geometry of the variable pitch helical coil parameterization. The power series in the winding parameter $\theta(p)$ is taken to fourth order to generate a good fit for the magnetic field that meets the spatial specifications of the experiment.

2.4.2 Zeeman Slower and Trapping Simulations

Now that we know our on axis magnetic field dependence, we can start simulating how an atom would respond as it travels down the slower. We began our simulations tracking one-dimensional trajectories through the coil. This simulation represents a perfect scenario: if our atoms stay perfectly on the path of the laser, do not interact with other atoms in the atomic beam, and maintain the adiabatic condition imposed in the design; this would be the behavior that we expect. A block diagram for the simulation is shown in Figure 2.8

Using this simulation we can track the velocity of an atom when it passes through the slower for different laser detunings. For a certain detuning, almost all of the atomic velocities are changed very little. For atoms in the designed velocity window however, there is a large effect. In Figure 2.9,

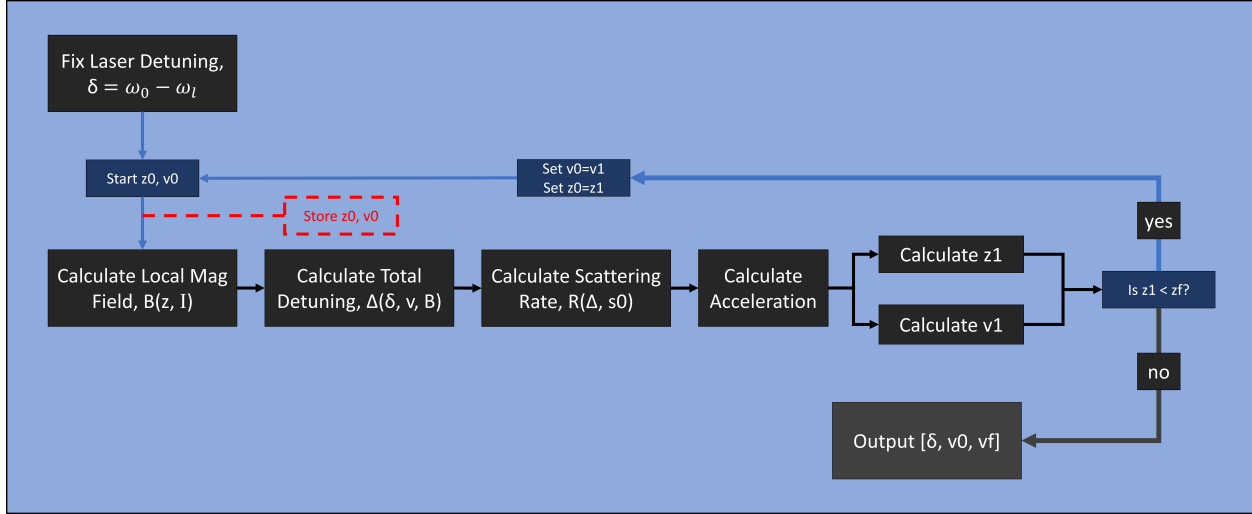


Figure 2.8: 1D Simulation Block Diagram: This is how we determine the atomic behavior in the perfect scenario of maintaining the adiabatic condition with non-interacting atoms. The magnetic field strength can be controlled with the current, I , and the scattering rate is effected by the laser saturation parameter, s_0 . It is set up to store individual velocity and position steps in an array, and outputs the detuning, initial, and final velocities.

we see the simulated evolution of several initial velocities with different laser detunings. Near the design condition, the Zeeman slower has little effect on atoms above the threshold velocity. These atoms are slowed slightly due to off-resonant scattering and leave the slower with close to the same velocity with which they had entered. Atoms below the threshold velocity but above the slower's exit velocity are greatly effected by the slower. For atoms in this window that are far from the threshold velocity, the atom will see similar off-resonant cooling until they reach the point where the magnetic field brings the total detuning to zero. They then follow the curve of the Zeeman slower design until they leave at the slower's exit velocity. In the one dimensional case, all of the atoms within the slower's capture range should leave at the exit velocity.

If we change the laser detuning, it has the effect of changing the exit velocity. During the slower's operation the detuning can be adjusted in order to vary the exit velocity in real time, for optimizations during trapping experiments. Another interesting aspect of the slower's operation is seen when we greatly change the laser detuning. As we tune farther from the design condition of an exit velocity near zero, we see that the total change in velocity for atoms on resonance in the

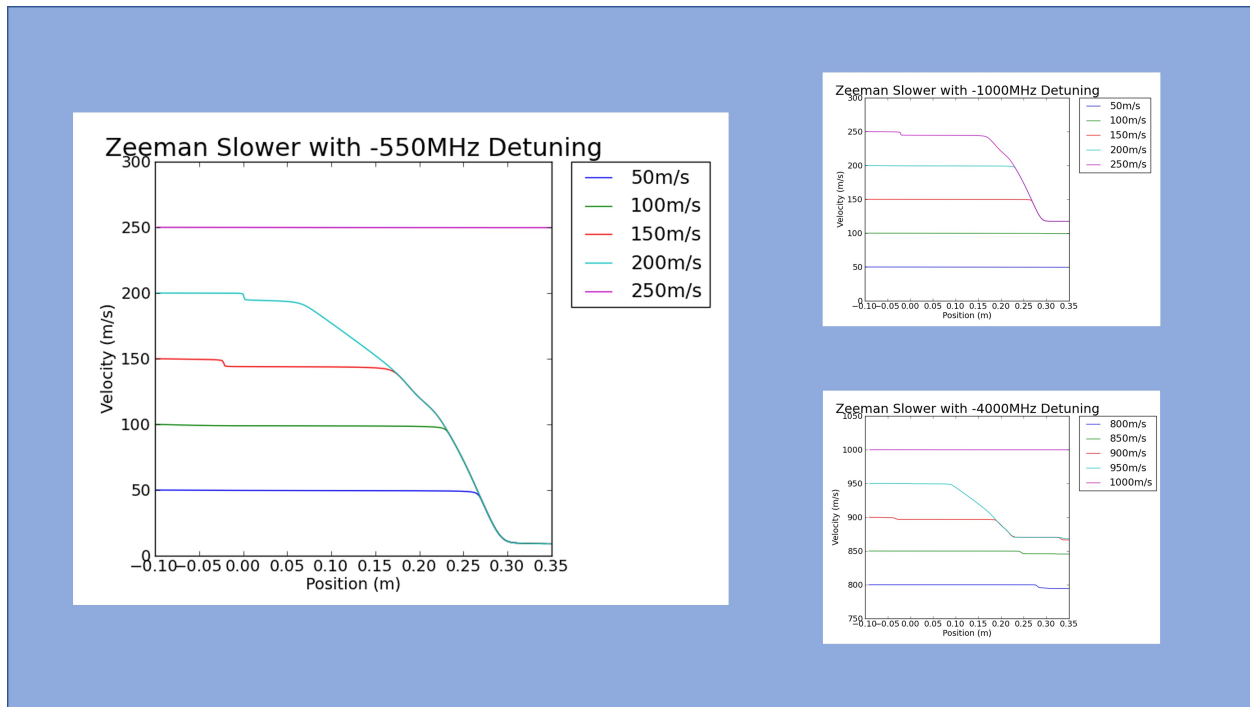


Figure 2.9: Simulated Zeeman Slower Velocity Changes for Different Laser Detunings: The simulation shows how we expect different velocities to behave as they travel through the slower. The Zeeman slower magnetic field zero crossing is located at position of 0.175m. For the design parameters, we expect atoms at 200m/s and below to enter the slower and exit at a velocity of approximately 10m/s. Atoms traveling faster than 200m/s see almost no effect. As we move away from the design parameters the dynamics are altered. The exit velocity and total change in velocity differ based on the detuning.

slower is reduced. This is to be expected, the adiabatic condition imposed in the design translates to constant acceleration motion. With the length constraint, the difference of squared velocities is conserved under kinematics.

We also ran simulations to determine our MOT trapping velocity as well as our expected trap size. Force terms were included for the two horizontal beams as well as the vertical laser beam and gravity. The trap center is at the origin and cooling lasers are Gaussian with centers that run along the x, y, and z axes. An atom traveling in the atomic beam will approach the origin from the negative x-y quadrant. Atoms looking at the trap center will see a spheroid potential as shown in Figure 2.10. The horizontal lasers approach the origin from 45° and therefore are projected with a larger effective area as seen from the atomic beam. Initial position and velocity were varied in three dimensions in order to simulate the trap capture dynamics under different approach vectors.

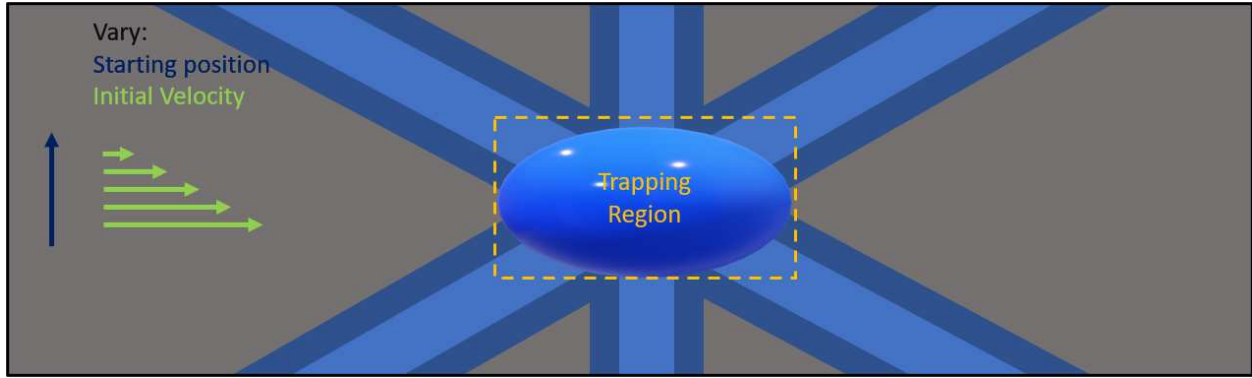


Figure 2.10: Trap Simulation Geometry Setup: In order to map out the effective size of our trapping region, the simulation will vary the starting position and initial velocity away from the trapping region and plot the trajectory. This gives us information on the variability of the trap velocity based on parameters of each individual laser, allowing us to tune optimum power balancing and predict what signals to expect from a functioning trap.

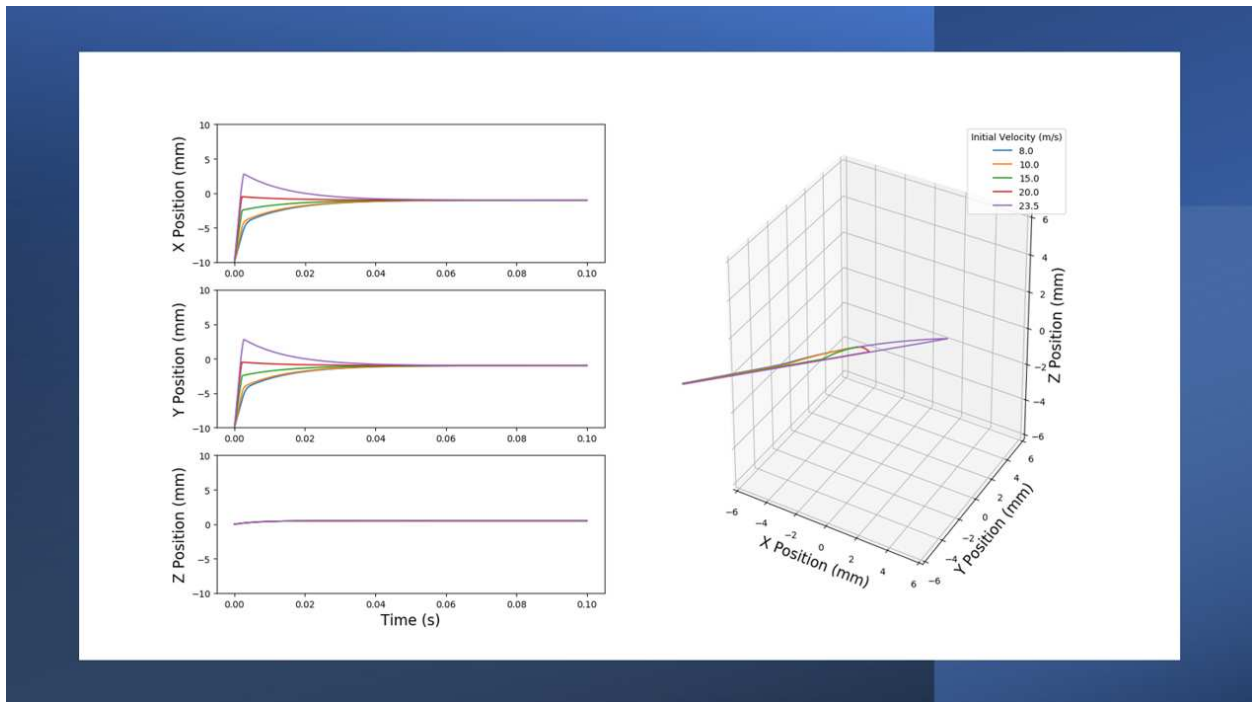


Figure 2.11: Trappable Velocity Simulation Plot: A visualization of simulated atoms falling into our trapping potential. Very little force is needed to maintain the vertical position contrasting the larger force needed for slowing and capturing the fast horizontal velocity.

An example plot can be found in Figure 2.11. From these simulations we found that when we increased the horizontal laser intensity it would increase the trapping velocity without the need for much increase in the vertical laser intensity. The vertical laser is a major source of background signal during trap runs; by maintaining the same signal from this laser but increasing our trapping velocity, we are able to increase our signal to noise ratio for atoms in the trap.

A final consideration that we simulated was the ballistic trajectories of our slow atoms. Our atomic beam is highly collimated, but there is a long path to the trapping region. It takes slower atoms a significantly longer time to reach the trapping region and it is prudent to simulate these trajectories taking into account the effects of gravity. We used kinematics to simulate ballistic trajectories along our vacuum system geometry, and rejected those that did not make it through our apertures along the beamline. Our simulations showed that the slowest atoms would not make it all the way to our trapping region, even if we increased the size of our apertures. However this window of atoms had such a low population of the total beam flux when compared to the total number of atoms expected that it was not seen to be a problem. Some of the simulated trajectories are shown in Figure 2.12, with stops showing the restricting apertures in our system. After this simulation we decided to set up our trapping lasers intersecting approximately 1-2mm lower than the center line of our atomic beam in order to enhance the capture of the slow atoms and slightly reduce the background signal of the fast atoms. We set up our imaging and laser systems with these details in mind; the center of the atomic beam is still within the field of view of our imaging system and any atoms slowed using the Zeeman slower will be visible. We also set up our magnetic field zero to overlap with this point.

A Zeeman slower would change the initial conditions for some of the atoms that should make it to the trapping region. Fast atoms that would usually not be captured will now exit the slowing region at a trappable velocity much closer to the trapping region. These changes were not accounted for in the ballistic trajectory simulation. This is not a problem however, these atoms will only increase our trappable atom population. Any atoms leaving the slower will leave at a set exit

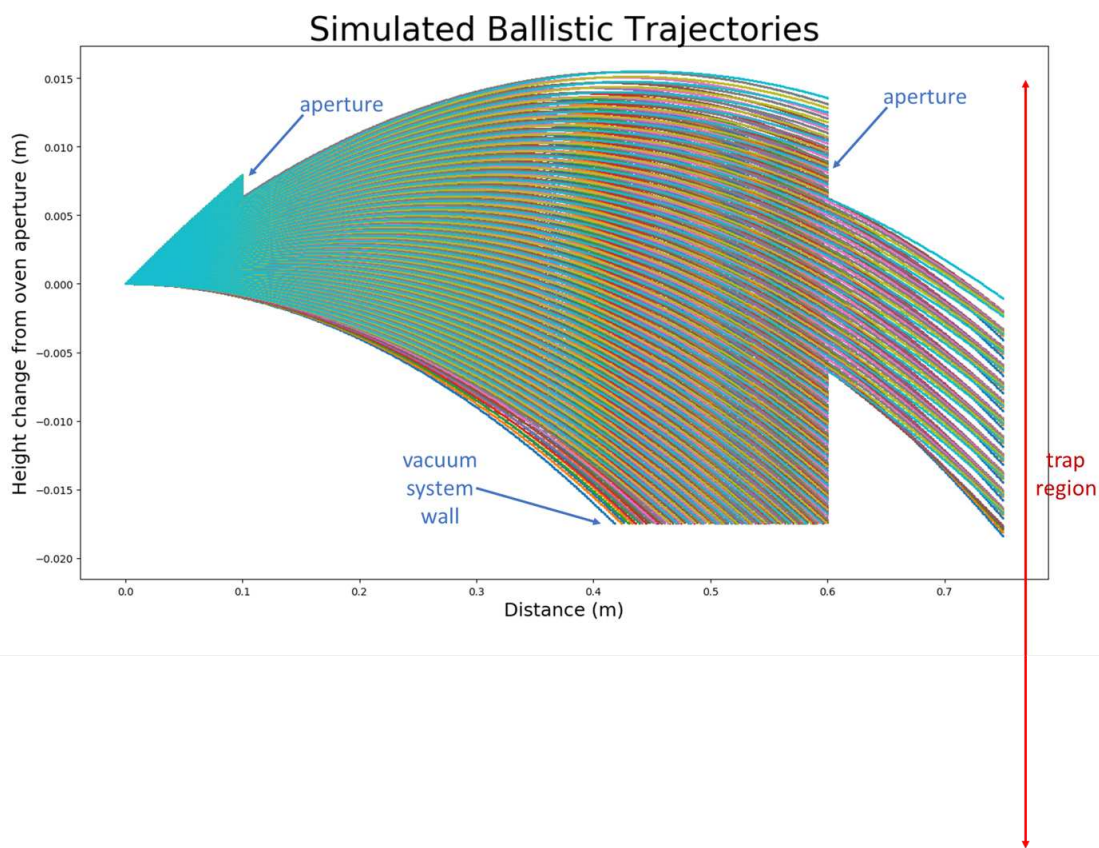


Figure 2.12: Ballistic Trajectory Simulation Plot: Simulated trajectories originating from the atomic beam aperture. Initial positions and launch angles were simulated along the exit of the oven with velocities in the range of 5m/s - 20m/s. Paths that impacted apertures or the walls of the vacuum system are rejected. We center the magneto-optical trap 1-2mm below the axis of the atomic beam in order to account for this and still have significant overlap with the main axis of the atomic beam.

velocity which can be adjusted by changing the laser detuning. We can tune the Zeeman slower to have just the right exit velocity for the slowed atoms to fall right into the trap.

2.5 Nonlinear Optics

In order to generate 221nm light needed for the experiment, we use second harmonic generation (SHG) in Lithium Triborate (LBO) to convert 886.8nm light to 443.4nm light followed by a second SHG setup in Beta-Barium Borate (BBO) to convert to 221.7nm light. When designing a frequency doubling laser system, following procedures for optimization of the power conversion between

the different laser harmonics is paramount. The conversion process takes place inside specially designed crystals with high nonlinearity coefficients. For an applied electric field inside a crystal, the polarizability, \mathcal{P} , is given by the matter equation, [43]

$$\mathcal{P} = \kappa(\mathbf{E})\mathbf{E} = \kappa_0\mathbf{E} + \chi^{(2)}\mathbf{E}^2 + \chi^{(3)}\mathbf{E}^3 + \dots \quad (2.18)$$

where κ_0 is the linear dielectric susceptibility, and $\chi^{(2)}$, $\chi^{(3)}$, etc, are the nonlinear dielectric susceptibility coefficients. These coefficients are expressed as tensors of rank 2, 3, etc. The $\chi^{(2)}$ term is only nonzero in crystals that are acentric, while the $\chi^{(3)}$ term is found in all crystals. [43] Typically, $\chi^{(2)} \gg \chi^{(3)}$, and our setup utilizes the action of $\chi^{(2)}$, which is responsible for SHG. The propagation of two monochromatic light waves of frequencies ω_1 and ω_2 can combine in the crystal to form light waves with the sum and difference frequencies given by:

$$\omega_{3,4} = \omega_2 \pm \omega_1 \quad (2.19)$$

For the special case when $\omega_1 = \omega_2$, we have second harmonic generation (SHG), where $\omega_3 = 2\omega_1$. Nonlinear effects are generally only observed when these waves are in phase with one another. In such a case we can define a wave vector difference:

$$\Delta\vec{k} = \vec{k}_3 - 2\vec{k}_1 \quad (2.20)$$

Nonlinear effects are most prominent when this difference $\Delta\vec{k} = 0$, which we call the phase-matching condition. In the simplest case of phase-matching, both \vec{k}_1 vectors propagate in the same direction as \vec{k}_3 . The vector notation becomes redundant and so this case is called scalar (collinear) phase-matching. This conditions needed for phase-matching then becomes:

$$n_3\omega_3 = n_1(2\omega_1) \Rightarrow n_3 = n_1 \quad (2.21)$$

where n_i is the index of refraction. In general, the refractive index is a function of frequency, $n = n(\omega)$, so we must find a way to vary the refractive index in order to meet the phase-matching condition for a particular wavelength. There are two common ways to meet this condition. One is through the use of angle tuning, and the other is temperature tuning. In many systems both of these conditions are used, however the temperature tuning in SHG is usually only utilized in high-power fixed-frequency pump lasers, or as a final correction to angle tuning.

Optically anisotropic crystals have optical properties that are not the same in every direction of propagation. We can utilize this behavior in order to satisfy angle tuning for the phase-matching condition. The traits of optically anisotropic crystals arise from anisotropy in the force of neighboring atoms in the lattice. This allows electromagnetic waves to propagate at different speeds as the electric field oscillates in various crystal plane orientations. This behavior manifests itself as different refractive indices along separate crystal axes. [44] Nonlinear crystals used for SHG are inherently optically anisotropic and there are two main categories: uniaxial and biaxial crystals. Uniaxial crystals have a single symmetry axis that we call the optical axis, while biaxial crystals have two symmetry axes. The single symmetry axis in uniaxial crystals gives rise to two different indices of refraction. Consider a light wave traveling in the \hat{k} direction that makes an angle θ with the optical axis. The plane containing \vec{k} and the optical axis is called the principal plane. If the electric field is oscillating in the principle plane, then we call that an extraordinary wave. If the electric field is oscillating perpendicular to the principle plane is called an ordinary wave. An ordinary wave will always travel with the same index of refraction n_0 , independent of the angle θ . As θ varies from 0° to 90° , the index of refraction of the e-wave varies from n_0 to n_e , and is given by an ellipse of the form

$$\frac{1}{n_e^2(\theta)} = \frac{\cos^2(\theta)}{n_0^2} + \frac{\sin^2(\theta)}{n_e^2} \quad (2.22)$$

This ellipse is shown schematically in Figure 2.13. We can orient a uniaxial crystal such that a photon can take on any refractive index that exists on the surface of this ellipse. Angle tuning is the process by which we orient this angle in order to meet the phase-matching condition.

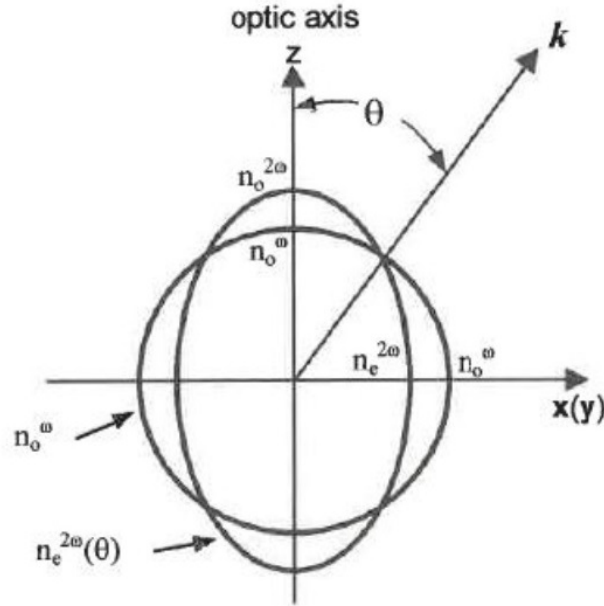


Figure 2.13: Refractive Index Ellipse: In anisotropic crystals, the effective refractive index can take on values between the ordinary and extraordinary indices by varying the angle of propagation through the crystal following the refractive index ellipse equation (Eq 2.22). At the intersection point the refractive indices are equal and the angle θ is called the phase matching angle.

Angle tuning techniques are separated into distinct types. In the "home-made" doubling cavities in the lab, we utilize what is called Type I⁽⁻⁾ phase-matching, or "ooe" phase-matching. In this type of three-wave mixing, the two waves at the fundamental frequency have polarizations along the ordinary wave direction and the harmonic (frequency doubled) wave polarization oscillates in the extraordinary direction. We use angle tuning to match the refractive index of the doubled photon to the ordinary refractive index of the fundamental photon.

For different types of crystal symmetry groups, there are different effective nonlinearity expressions based on the geometry of the crystal. For the calculations in our home-made cavities, I used expressions found in reference [43]. A more general approach can be found in reference [45]. For biaxial crystals, the process is much the same after fixing one of the crystal axes. In order to choose which axis should be fixed, and in what direction, you look to maximize these effective nonlinear expressions using experimentally obtained values for the nonlinearity coefficients of the crystal.

In order to choose parameters needed for the cavity design and crystal specifications, we must optimize the power generation in SHG. The SHG power is given by the expression: [46]

$$P_2 = KP_1^2lk_1h_m \quad (2.23)$$

where P_i is the power of each beam, l is the crystal length, k_1 is the fundamental wave number, and K and h_m are dimensionless parameters which I will discuss in the following paragraphs. All of these are expressed in SI units. This treatment includes consideration for double refraction as well as several different focusing regimes. It is beneficial to define a *focusing parameter*, $\xi = l/b$, where l is the crystal length and $b = k_1w_0^2$ is the confocal parameter. Our design is in the strong focusing limit, where $\xi \gg 1$. There is also a double refraction parameter given by $B = \rho\sqrt{lk_1}/2$ where l and k_1 are defined as before, and ρ is the walk-off angle, the angle between the wave vector and the Poynting vector. With these parameters defined, an h_m parameter can be defined in the strong focusing limit as:

$$h_m = \frac{\sqrt{\pi}}{2B\sqrt{\xi}}\tan^{-1}(\xi) \quad (2.24)$$

This function reaches a maximum when $\xi \approx 1.392$. This sets the optimum waist size in the crystal, which drives the enhancement cavity design. Our cavity design does not meet this criteria, so we optimize for the smallest round spot size in the crystal that we can. Our first doubling cavity (from 887nm to 443nm) utilizes a 1.5cm LBO crystal. With 650mW of incident light, we were able to generate 100mW of 443nm light. This cavity conversion efficiency out-performs the commercial Wavetrain doubler. Doubling for the second stage, 443nm to 222nm, utilizes a 1cm Brewster face BBO crystal. The home-made cavity is more problematic and the performance is not ideal. We use a bowtie configuration for our cavities [47] which have two distinct waists, a large one and a small one. At least one of these waists is always elliptical. In order to get optimum performance from the cavity you must mode match the laser beam to the large waist using multiple lens systems. We had difficulty obtaining an optimized input coupler mirror for our BBO cavity. We were only able

to obtain 1mW of 222nm light. We decided to design this cavity with a round large waist which led to an elliptical small waist in the crystal. At the time, we believed that this would allow us to couple more power into the cavity and get better output power from the BBO conversion process. We now believe that decision to be ill advised and would suggest others to optimize for a round waist in the crystal for the best performance. With a cavity redesign and a proper input couple, we believe that our BBO conversion efficiency performance would be improved.

K is a parameter that depends on the fundamental laser wavelength and crystal parameters. It is expressed as:

$$K = \frac{8\pi}{\epsilon_0 c n^3 \lambda_1^2} d_{eff} \quad (2.25)$$

where ϵ_0 is the permittivity of free space, c is the speed of light, n is the phase-matching refractive index, λ_1 is the fundamental wavelength, and d_{eff} is the effective nonlinearity parameter of the crystal, expressed in m/V . d_{eff} itself is defined in terms of the crystal angles chosen to meet the phase-matching condition as well as the nonlinear coefficients given along each crystal axis. For biaxial crystals, you are given a choice as to which crystal planes are used in the nonlinear conversion process. In practice, this choice is clear, there is generally one nonlinear coefficient that is larger and therefore more efficient than the others. Our first doubling cavity uses a LiB_3O_5 , Lithium Triborate (LBO) crystal, which is biaxial. Our second cavity uses a $\beta\text{-BaB}_2\text{O}_4$, Beta-Barium Borate (BBO) crystal, which is uniaxial. The d_{eff} coefficient for these crystals for "ooe" phase matching are given by:

$$\begin{aligned} d_{eff,LBO} &= d_{32} \cos\phi \\ d_{eff,BBO} &= d_{31} \sin\theta - d_{22} \cos\theta \sin 3\phi \end{aligned} \quad (2.26)$$

The effective nonlinear coefficient for LBO is given for doubling in the "XY" plane of the crystal by setting the crystal angle θ is to 90° , the angle ϕ is the calculated phase matching angle. For BBO, the angle θ is the calculated phase matching angle, while the angle ϕ is set to maximize the coefficient. The angle ϕ breaks the inversion symmetry of the crystal, which gives photons

traveling through the crystal a preferred direction for maximum conversion. In practice if the doubling conversion efficiency is underperforming by a significant amount, it may be that the crystal is installed backwards.

Chapter 3

Experimental Apparatus and Techniques

3.1 System Overview

In this chapter I will present all of the experimental equipment we found necessary for our investigations into the cooling and trapping of silicon. A block diagram of the experimental setup we have developed is shown in Figure 3.1. I will begin by presenting our considerations with respect to the atomic beam source in Section 3.2. I will then discuss the design and construction of a variable pitch Zeeman Slower in Section 3.3. Sections 3.4 and 3.5 present the vacuum chamber design and collection optics. Section 3.6 will demonstrate the different laser systems that are needed. Finally in Section 3.7 I explain our saturated absorption spectroscopy setup used for obtaining all of our Doppler-free tellurium and iodine spectra for frequency references. Much of the design, construction, and implementation of these systems was performed by myself.

3.2 Silicon Atomic Beam

Our initial atomic beam setup was adapted from a system used by Roger McGowan in our lab for light force manipulation of an aluminum atomic beam. [47] It utilized direct ohmic heating of a heater element that held a graphite oven which we machined in house. It was loaded from the top and the beam was extracted through a small conical hole drilled into the side. This hole acted as a very thin walled aperture, giving the atomic beam a wide angular spread as discussed in Section 2.3 and shown in Figure 2.5. Hot silicon vapor is extremely corrosive, and typically destroyed the heating element in a few days of experimentation. After a failure in the water cooling lines of this source, we decided to upgrade the system with a source purchased from Veeco.

Our silicon atomic beam source is a commercial high temperature molecular beam epitaxy (MBE) source from Veeco (model number: 10-HT). This source can operate to 2000°C and is equipped with water cooling. The source was purchased with a tungsten crucible and a graphite

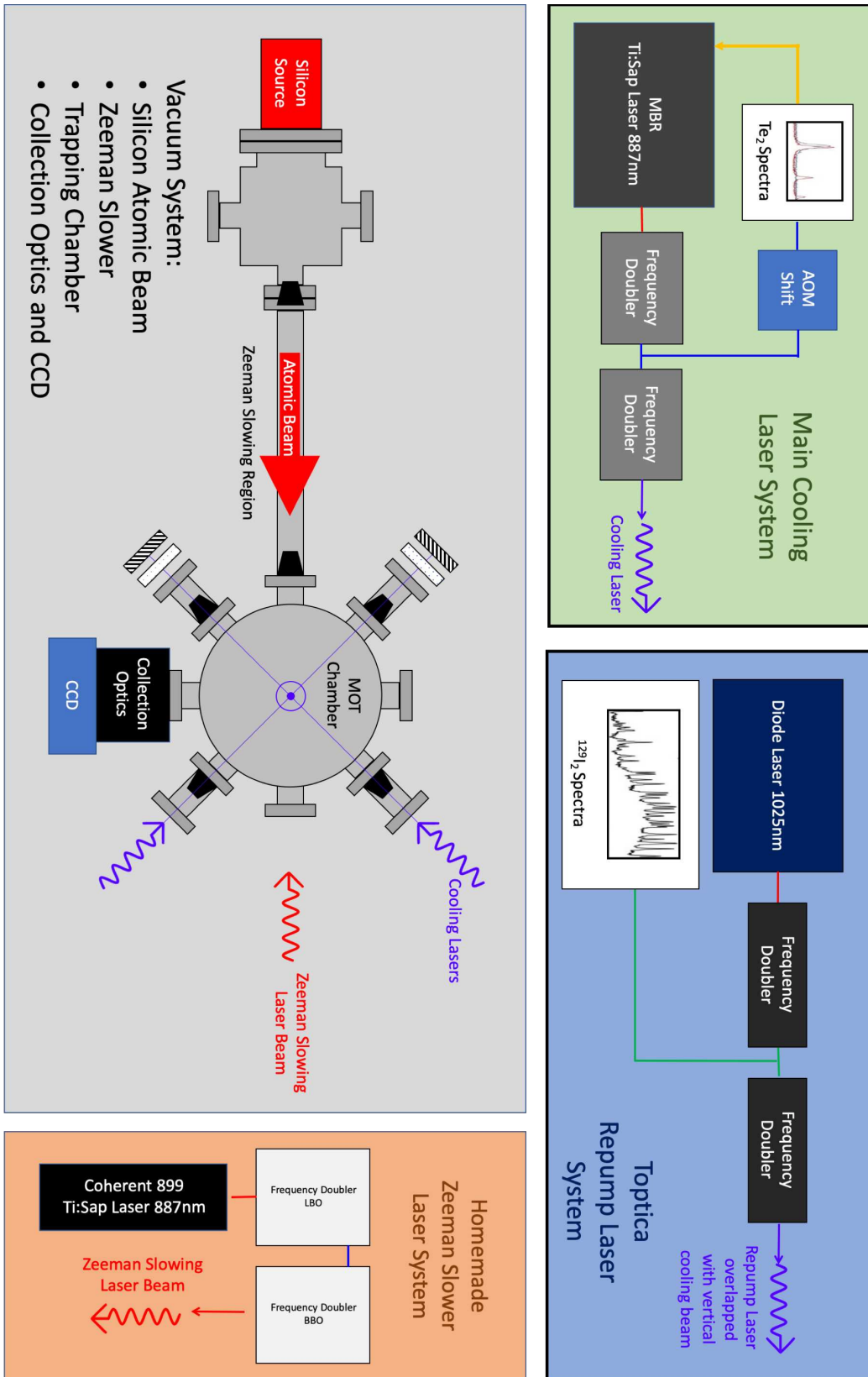


Figure 3.1: Full Experiment Block Diagram

liner. A graphite cap with a 1mm hole was used to provide collimation for the silicon beam. The source is mounted horizontally in our experiment. There is an extensive outgassing procedure for installing this source. First the source is slowly stepped up to operating temperature with no liner or crucible. Ample time is needed at each temperature step for this initial outgassing to maintain good operating pressure while contaminants are expelled from the system. Due to the fact that there is a minimal thermal mass without the crucible installed, the temperature can be fairly unstable in comparison to beam running conditions. This procedure is repeated after installation of the crucible, and again for the installation of the liner. After all of these pieces have been sufficiently outgassed, silicon is loaded into the liner and topped with the cap. We generally loaded approximately 0.5-1 gram of highly pure silicon wafer strips into the liner.

The original design worked well for ~ 100 hours before we began to see a drastically reduced silicon signal in our test chamber. Upon removal, the liner and crucible fell apart with a long crack along the side and small cracks at the end of the liner. The liner was dark in appearance and the remaining silicon seemed to have permeated the liner walls when we checked the weight. We then purchased a new crucible and liner from Veeco and machined a new cap. This new oven lasted for less than a dozen hours over two run days before the heating filaments shorted out, causing the system to become unusable. When removed, we found that this new cap and liner had completely split along the cross section of the crucible and liner. The silicon then came in contact with and destroyed the heating filaments. While the original liner looked solid when it failed, the newer liner was different in appearance. It had a layered structure along the cross section. The liner had a speckled appearance and a gray color rather than the darkness seen in the original liner.

Through further investigations, we found that graphites used in MBE sources are fairly porous with connected holes, to facilitate pumping out impurities in MBE applications. However, for our silicon source, we need graphite of high density and unconnected pores, so that the corrosive molten silicon will take longer to deteriorate the sides of the liner. We decided that it would be best if we machined our own ovens. From our previous experience with high temperature ovens, we decided that the tungsten crucible was not needed and that we would build our source entirely out

of high density graphite. This graphite came from POCO Specialty Graphites and Materials. The product that we used is called DFP-2, there is a newer version called DFP-3-2. This graphite is characterized by its relatively high density, which causes it to have less connected pores, a feature that we believe is needed to use the oven properly in this configuration. Our design is shown schematically in Figure 3.2.

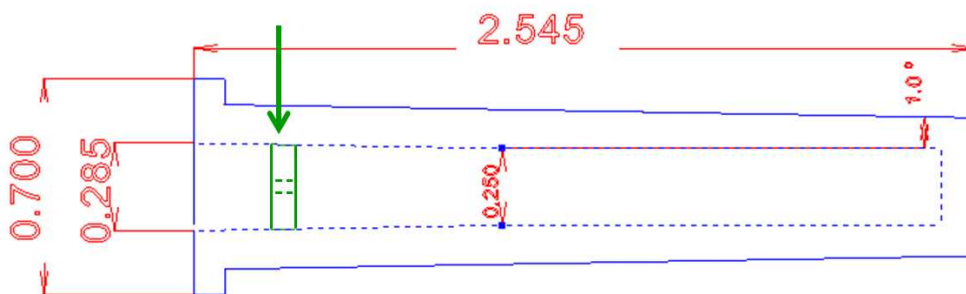


Figure 3.2: Silicon Oven Schematic: The oven is machined from graphite to match the mounting of the Veeco HT-10. The green arrow indicates the location of the cap, which was machined separately. Dimensions are in inches.

The interior of our oven has a 1° taper for the first inch of depth, followed by a straight cut to the end. The taper was matched on our fabricated cap, so that the cap could be placed at $1/4''$ from the opening of the oven and would fit in snugly. The placement position of the cap is shown in the design schematic in green. The cap itself has a length of 2mm and a hole diameter of 1mm, which should allow for effusive flow. [41] The outer taper is set to 1° in order to match the support structure designed by Veeco to hold the oven.

Silicon has a very high melting point at 1425°C . With the geometry that was needed for our operation, and after the failure of the second purchased oven, we were careful to not exceed this temperature. Up until this point we had been outgassing our oven to 1600°C and running at 1425°C . For future runs we decided to keep our operating temperature at least 20°C below the melting point. The original crucible and liner temperatures were initially checked with a pyrometer and were

found to be the same as the set point on the controller. With our home made oven design it was more critical to ensure this running condition with the pyrometer. We found that we generally ran the controller at a set point of 1315°C to maintain an oven temperature of $\sim 1405^\circ\text{C}$, with a vapor pressure 3.40×10^{-4} Torr. [48] We did not observe any failures while maintaining this condition.

The longitudinal velocity distribution of an effusive source such as this one takes the form: [41]

$$\Phi(v) \propto v^3 e^{-\frac{mv^2}{2kT}} \quad (3.1)$$

The most probable velocity of the distribution is $v_p = \sqrt{\frac{3k_B T}{m}} \approx 1200\text{m/s}$ for 1400°C . Figure 3.3 shows this velocity distribution, which has been verified in our system by laser spectroscopy. Trapping velocities in a magneto-optic trap are typically $\leq 20\text{m/s}$, which is only $\sim 10^{-7}$ of the total beam flux. In the beginning of our magneto-optical trap (MOT) trials, this was seen as a possible feature of the system, as the ultimate goal of the experiment was the trapping of only a single atom. However, as discussed later, this low flux ultimately kept us from seeing a trap signal.

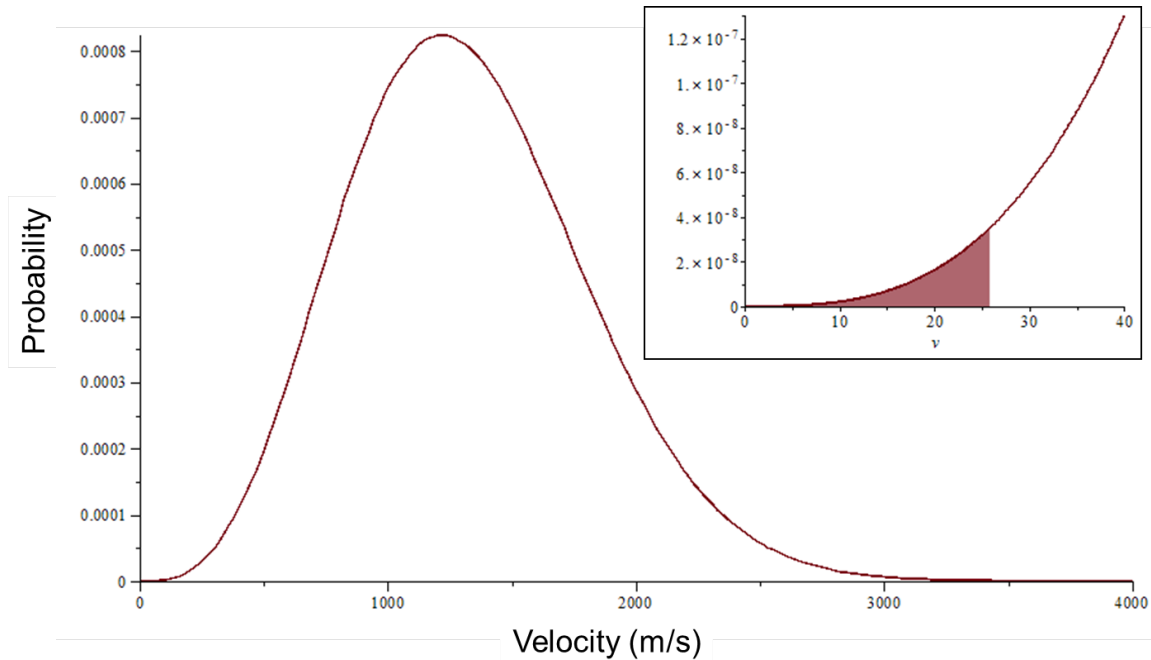


Figure 3.3: Silicon Velocity Distribution: Plotted is the silicon atomic velocity distribution at 1400°C . The inset shows the expected portion of the distribution at trappable velocities.

3.3 Variable Pitch Zeeman Slower

In order to increase the flux of trappable silicon atoms into our trap region, we must find some way to pre-cool the atomic beam. Zeeman slowers are typically used in magneto-optic trap (MOT) experiments whose atoms are generated from a beam source. This is particularly true for atoms with high melting points. Atoms may be slowed from recoils from a counter propagating laser. Many recoils are needed in order to decelerate the atomic beam by a usable amount. A laser at fixed frequency will only be on resonance for a particular velocity, due to the Doppler shift. Zeeman slowers are built in order to keep the laser on resonance with a constantly decelerating atom by compensating for this changing Doppler shift with a tailored magnetic field. A magnetic field profile is created that will match the Zeeman detuning with the expected Doppler detuning from an adiabatically decelerating atom. From this interaction, it is possible to keep the atom in resonance with the decelerating laser for many thousands of transitions. Zeeman slower design and theory is well established in the literature, [36, 42] and the parameters for our design are summarized in Table 3.1.

Table 3.1: Important parameters of our constructed Zeeman slower.

v_r , recoil velocity	6.4 cm/s
$s_0 = I/I_{sat}$, saturation parameter	0.1
λ , slowing laser wavelength	221.74 nm
δ , detuning from atomic resonance	-448 MHz
L , Zeeman Slower length	27 cm
Γ , atomic scattering rate	$4.54 \times 10^7 \text{ s}^{-1}$
v_{enter} , Zeeman slower entrance velocity	200 m/s
η , efficiency factor	0.55
Operating Current	120A

The standard way to create this magnetic field profile is to build a tapered solenoid coil, whose taper generally follows the field profile needed for the decelerating atom. This design suffers from heavy resistive load as well as a high inductance. The resistive load gives rise to significant heating which must be mitigated, usually by using a water-cooling scheme. Our Zeeman slower is based off a novel design first seen in Robert Scholten's group using a variable pitch Zeeman slower. [42]

This slower mitigates the high resistive load and high induction, but still generates a considerable amount of heat due to the fact that it must be run at high current. It is also important to state that safety considerations must take high priority when running a coil at the currents required for operation.

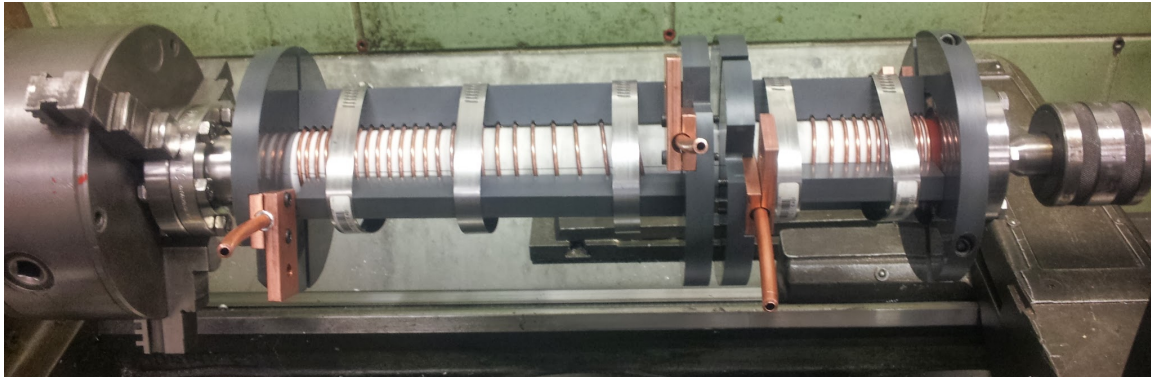


Figure 3.4: Constructed slower mounted on a lathe

When designing our Zeeman slower, the largest design constraint was due to the amount of space available. In addition to this the coil winding cannot be too tight in order to accommodate the size of the $\frac{1}{8}$ " diameter copper refrigerator tubing used to carry the current. The Maple worksheet that was used to finalize the design can be found in Appendix A. Our slower has an effective length of 27cm for the magnetic field profile, however the actual geometric length needed was close to ~ 35 cm.

Once the Zeeman slower design was finalized, the variable pitch path was printed out on paper and fixed to the outside of a 1.5" diameter vacuum tube that had been coated with a dielectric paint. Figure 3.4 shows the Zeeman slower mounted on a lathe during construction. Copper refrigerator tubing with $\frac{1}{8}$ " diameter was wound on the stainless steel tube following the design on the paper. Dark HDPE plastic clamps were constructed to hold the copper coil in place at 3 points equidistant around the circumference of the tube. These clamps were machined on a CNC mill with slots that followed the designed pitch. The slower is cooled by water circulating through the copper tubing.

Up to 120A of current was applied, which produced peak fields of ± 300 Gauss at the entrance and exit of the slower. The coil overheated when run with currents ≥ 130 A, limited by the flow rate of the cooling water. Figure 2.6 shows the magnetic field profile for 120A, with the ideal field superimposed on the image.

3.4 Trapping Chamber

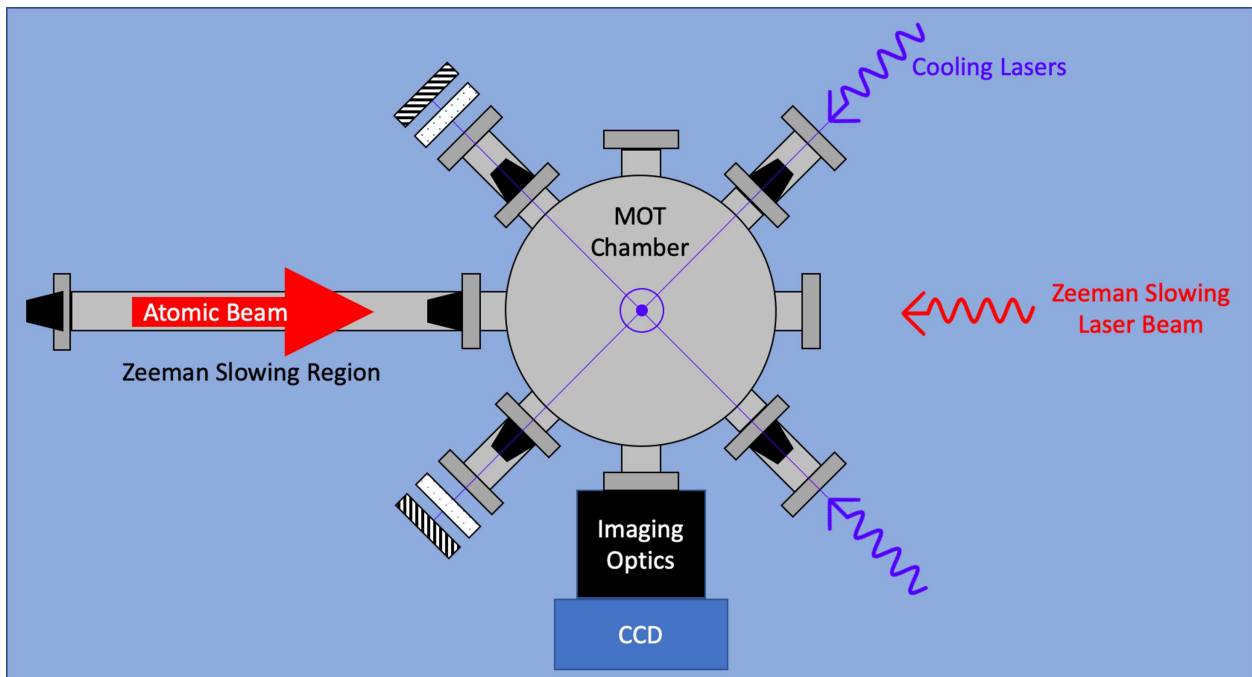


Figure 3.5: Top View of the Trapping Chamber: Atoms from our beam source enter the trapping chamber after exiting the Zeeman slower region. A window on the far side allows for Zeeman slowing laser light, shown in red, to enter and scatter off the atoms during their travel. Counter propagating laser beams, shown in blue, apply the optical cooling force. Imaging optics mounted to the side collect fluorescence from the trap and project onto a CCD camera.

Our trapping volume is built from an eight-way cylindrical chamber and parts utilizing an ultra-high vacuum stainless steel conflat construction. A base pressure of 10^{-8} Torr is achieved using two turbomolecular pumps, one near the atomic source region and one near the trapping region. During high temperature operation this pressure rises to $2-5 \times 10^{-7}$ Torr. Atoms travel down the Zeeman slowing region and enter the chamber from the side. Blackbody light coming from the

oven producing the atomic beam is reduced with light baffles placed at the entrance and the exit of the slower. These light baffles were cones machined from aluminum and coated with a thin layer of flat black spray paint from Krylon. These were allowed to outgas in air before being installed in the system and we found this paint to have minimal outgassing once installed in the system.

Cooling light to form the magneto-optical trap (MOT) enters through 3 ports and is retro-reflected in order to have 6 counter-propagating beams. These entered the main chamber through 4" long vacuum nipples which also had light baffles installed to cut down on stray light entering from those ports. The windows were AR coated for 221.7nm with a 10° wedge to prevent back reflection and further reduce unwanted scattered light. Imaging optics mounted to the side collect atomic fluorescence and were installed to image the trap region onto a CCD camera. This is all shown schematically in Figure 3.5. The vertical laser beam is able to address the transverse velocity distribution of our atom beam, while the 45° and Zeeman slower beams can be used to address longitudinal distribution. Initially this was done with a PMT mounted on the port opposite of the CCD camera. This was uninstalled after we found that the CCD system had much greater sensitivity and a lower noise floor.

MOTs are known to be fairly robust against potential mismatch of laser intensities for forward and reverse laser beams. The magnetic field gradient needed to for a magneto-optical trap was originally created using anti-Helmholtz coils mounted directly to the outside of the MOT chamber. Modeling showed that our expected reflected power coupled with the weak field gradient of 4G/cm would offset the trap center enough for atoms to move to the edge of our viewing region. The atoms would continue to move so that they left the intersection of the six laser beams, making the setup impossible to form a trap. An increased magnetic field gradient would mitigate these problems. Thermal issues as well as power concerns became an impediment in increasing this field gradient with the installed hardware. We decided to redesign the field using a set of permanent magnets.

After some simulations, we found that we could build a structure to hold a set of magnets at the proper radius and separation. This set of permanent magnetic field coils is shown in Figure 3.6. Not shown in the picture are a second set of magnets that were press fitted to the under-side of the

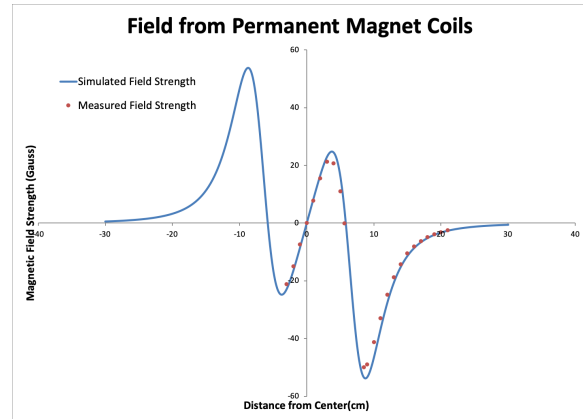


Figure 3.6: Permanent Magnetic Field Coils: On the left is a picture of the constructed permanent magnetic field coils. On the right is the expected and measured radial field of the coils.

coil forms. The forms for the magnet holders were machined on a CNC mill and spray painted with flat black paint from Krylon. The magnets were then press-fitted into the forms. The posts and mounting hardware were machined by hand on a lathe and mill, respectively. Care was taken to machine the parts so that they would facilitate pumping in order to prevent any virtual leaks in the vacuum system. The entire structure was then rigidly mounted on the inside of our trapping chamber. Figure 3.6 also shows the expected field from these coils. Our simulations showed that this should be sufficient to form a trap in the intersection of the beams, viewable with our imaging system.

3.5 Collection Optics and CCD

Our CCD camera is an Andor iXon EMCCD. This camera has electron multiplying capabilities that reduce the readout noise to almost zero. Coupled with a 3-stage Peltier cooled CCD chip to reduce thermal noise. We have enough sensitivity to detect single photons. An optical system was constructed in order to collect fluorescence ion the region where we expect the MOT to form, shown in Figure 3.7. The $f=10\text{cm}$ collection lens is mounted on the inside of the trap chamber port and the 222nm filter is mounted directly to the vacuum flange holding the collection window.

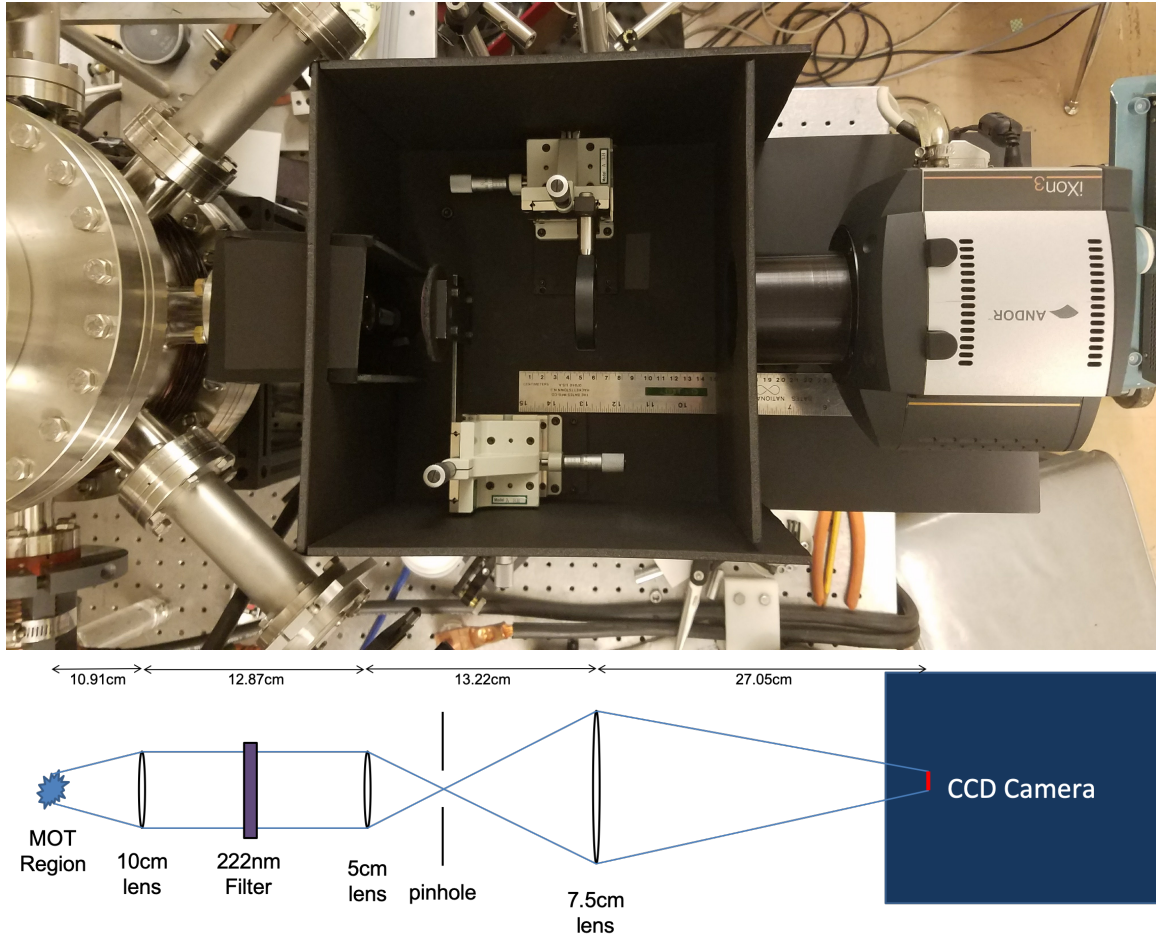


Figure 3.7: CCD collection optics and design schematic: Fluorescence in the trapping region is passed through a 222nm filter and imaged onto a CCD camera. 3-axis micrometer translation stages give excellent control of the imaging system. All the optics are mounted in a dark box that is covered and wrapped with dark cloth to reduce background light to negligible levels. This setup is sensitive enough to detect single photons inside the vacuum chamber.

Light leaving the chamber through the filter is then focused using a fixed 5cm lens through a pinhole mounted on a 3-axis translation stage. The $f=7.5\text{cm}$ reimaging lens is mounted on a 3-axis translation stage and focuses light that passes through the pinhole onto the CCD imaging plane.

With our atomic beam running at $\sim 1400^\circ\text{C}$, our system had a significant amount of blackbody light that contributed to the background. During our investigations, we took a series of images as we ramped up the temperature of the oven. The count data was fitted to a blackbody spectrum as a function of temperature. We had expected to find that this light was from the buildup of UV

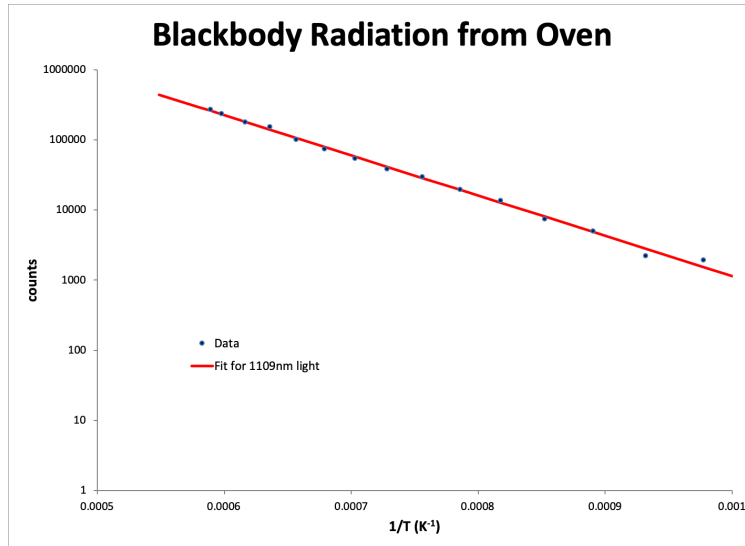


Figure 3.8: Blackbody spectrum of our collection optics setup.

from the blackbody. As shown in Figure 3.8 this was not the case. Our background light was not transmission of UV light through our transmission filter, but came from light whose wavelength was $\sim 1.1\mu\text{m}$. We then tested the filter transmission. This data can be found in Figure 3.9. Our major background contribution from the oven is due to a very small leakage of this $\sim 1.1\mu\text{m}$ light. In discussions with several filter companies, suppression of this transmission was not feasible. We discussed possibly stacking two of these filters to further suppress this background, however it would also decrease our signal at the wavelength of interest.

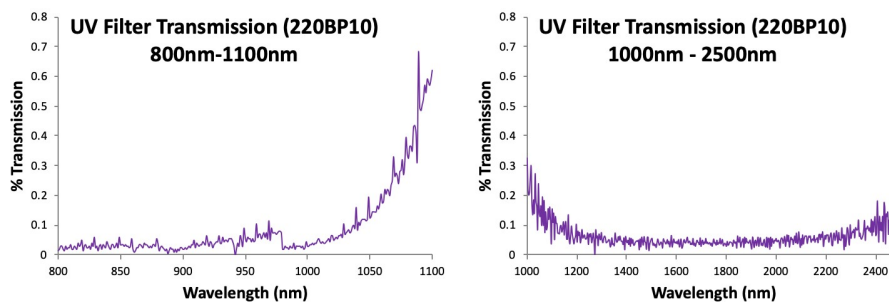


Figure 3.9: Transmission of our UV filter

Extensive testing was done in order to determine the focal position as well as the depth of field of the optical imaging setup to ensure that it was focused on the center of the trapping region. The focusing was performed by pasting a grid on a magnetic field probe. The probe was then used to find the magnetic field zero and then offset by half of the width of the probe to place the grid at the zero point of the magnetic field. The grid was then illuminated using the main cooling laser. Using this as a zero point, the position of the grid was varied using a 3-axis micrometer translation stage to map out the focusing condition of the optical system. If the focus was not centered at the zero point, the last lens in the optical system was moved to a new position using a separate micrometer. The focus was mapped again using the same method. This process was iterated until proper focusing was achieved. The final focusing map is found in Figure 3.10.

In order to analyze our atomic beam performance, we must first analyze how many photons are arriving on our CCD chip. The CCD gives a readout in count number. This count number has been padded with a zero offset that is equal to a count of 100 per collection bin. In practice however, this bias will be subtracted off with appropriate background subtraction. This will also remove any background light due to scattered light from the temperature of the beam source. Depending on the collection settings, the count number corresponds to a certain number of detected electrons at the A/D converter. This information is provided by the manufacturer in the system performance report and the values for our readout setting are shown in Table 3.2

Table 3.2: Sensitivity at 1 MHz 16-bit Readout

PreAmp	Electrons per Count
1.0x	24.2
2.4x	9.8
5.0x	4.4

In addition this detected electron number has been enhanced by an electron multiplier, whose gain is set by the user. These electrons have been produced with a particular quantum efficiency that is dependent on wavelength. The QE curve from the camera specification sheet is shown in Figure 3.11. In our UVB camera, and out wavelength of interest of 222nm, the QE curve shows an

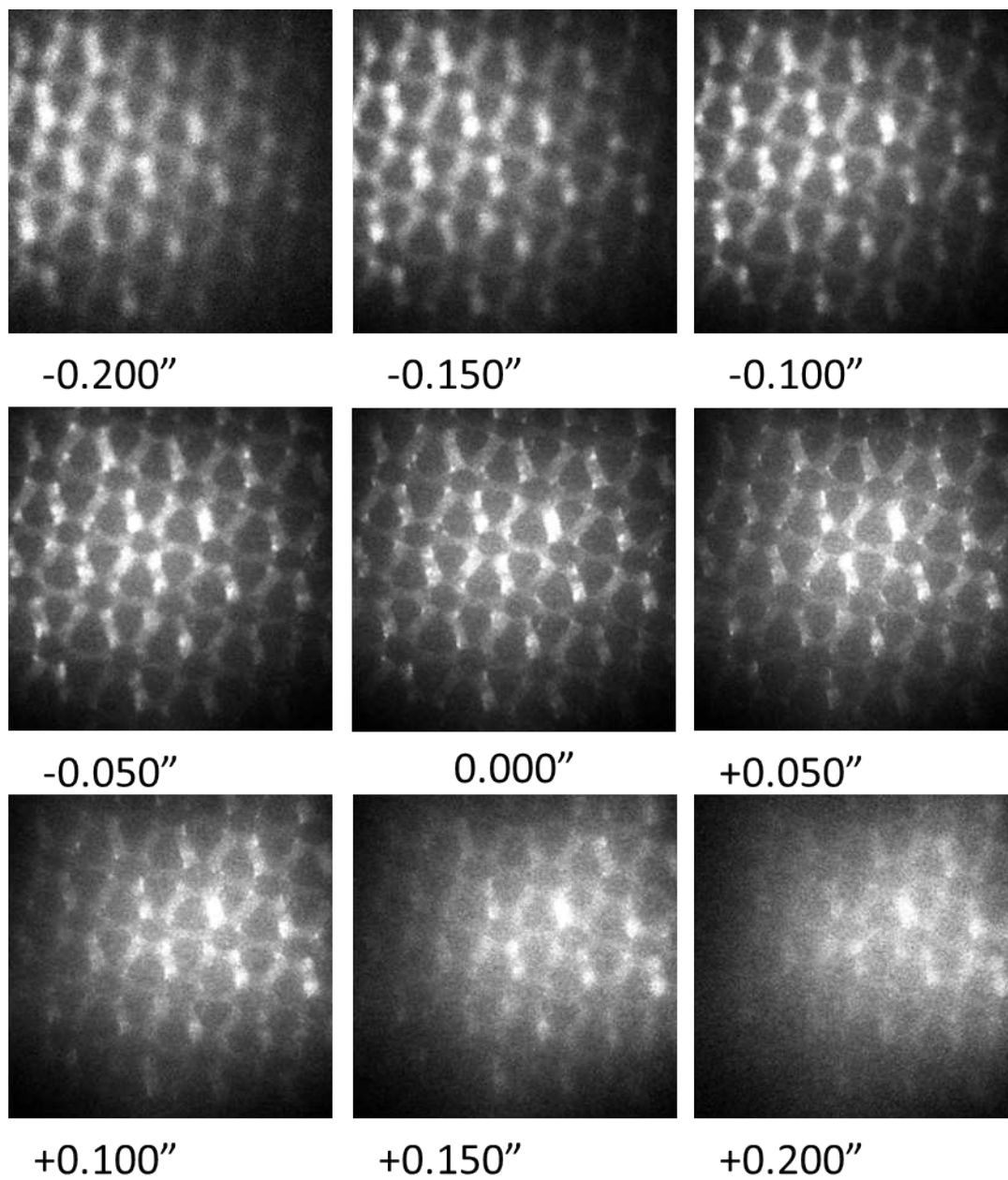


Figure 3.10: Images to determine the depth of field and focus of the CCD optics.

Quantum Efficiency (QE) Curve

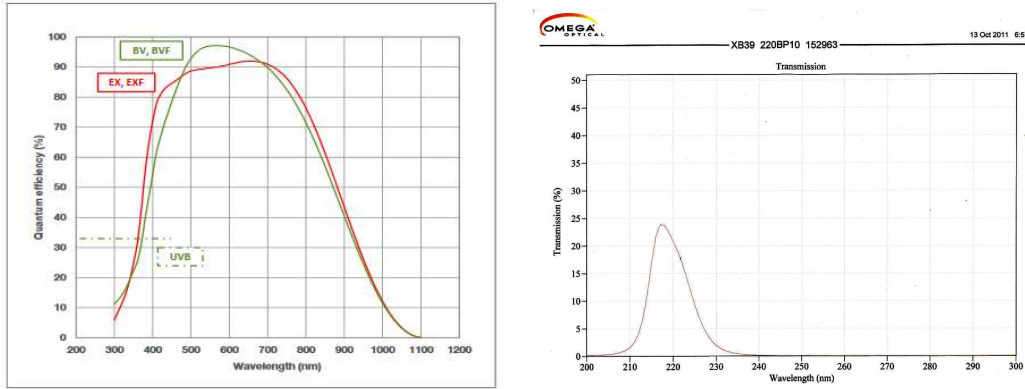


Figure 3.11: On the left we have the efficiency response of our UVB CCD chip. On the right we have the specified transmission data on our UV filter.

efficiency of approximately 32%. This information is said to come from the chip manufacturer and tested at 25° C. The 32% is an average value and the best measurement provided for the efficiency. The function for converting from counts to photons incident on the CCD array is:

$$photons_{incident} = \frac{(counts - background) \cdot sensitivity}{Gain_{EM} \cdot QE_{CCD}} \quad (3.2)$$

Our collection optics setup is shown in Figure 3.7. This setup was designed so that light in the solid angle collected by the first lens is collected completely by subsequent lenses. The collection efficiency due to the solid angle collected by the first lens is:

$$\frac{\Omega}{4\pi} = \frac{Area}{4\pi \cdot D^2} = \frac{\pi r^2}{4\pi \cdot D^2} = \frac{r^2}{4D^2} \quad (3.3)$$

in this equation $D = 10.9\text{cm}$ is the distance from the first lens to the trap center and $r = 1.25\text{cm}$ is the radius of that lens. This give an efficiency of $\Omega/4\pi = 3.29 \times 10^{-3}$.

Also included in the setup is an interference filter, placed so that light passing through the filter is highly collimated. Figure 3.11 shows transmission data provided by the manufacturer for this filter. At 222nm, we have a transmission of approximately 17.5%. Combining all of these factors with the incident photon expression from Equation 3.2, we have:

$$\begin{aligned}
\text{photons}_{emitted} &= \frac{(\text{counts} - \text{background}) \cdot \text{sensitivity}}{\text{Gain}_{EM} \cdot QE_{CCD} \cdot T_{filter} \cdot \frac{\Omega}{4\pi}} \\
&= 4750(\text{counts} - \text{background}) \left(\frac{\text{sensitivity}}{\text{Gain}_{EM}} \right)
\end{aligned}
\tag{3.4}$$

3.6 Laser Systems

Figure 3.12 shows the level structure for atomic silicon. The main cooling transition occurs at 221.74nm, has a saturation intensity of $86.7 \frac{mW}{cm^2}$, and a natural linewidth of 7.2MHz. It also has a weakly coupled repump transition at 256.26nm with similar saturation intensity and linewidth. In order to produce a magneto-optical trap (MOT) with silicon, there is a need for several continuous wave lasers with tunable wavelengths in the deep ultraviolet region with powers on the order of 10s of mW. Direct lasing in the ultraviolet is difficult to produce, and the options in most systems are not tunable. In order to overcome these limitations, we employ direct lasing using tunable sources in the infrared, and then follow that laser source with two stages of second harmonic generation using nonlinear crystals.

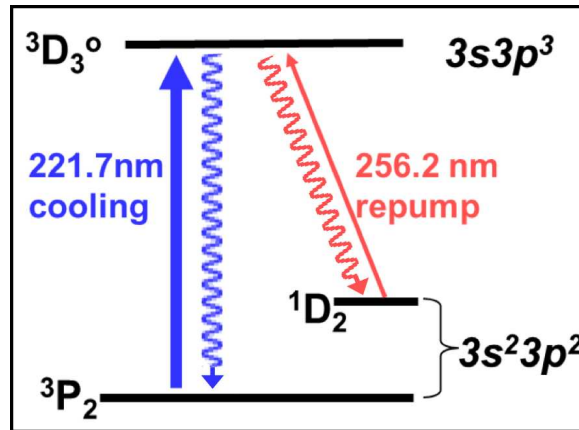


Figure 3.12: Silicon Energy Levels

3.6.1 Cooling Laser

Our main cooling laser system utilizes a Coherent MBR Ti:Sapphire master laser, pumped by an 18W Verdi Pump laser, and followed by two tandem Spectra-Physics Wavetrain frequency doubling modules. During installation we were told that this was the first frequency quadrupling system of its kind that had been installed by the manufacturer. When operating for purposes of the MOT, we typically pump the MBR with 13.5W of Verdi Power, giving approximately 2.5W of power at 887nm. This is mode matched into the first Wavetrain system and produces approximately 600mW of 443.5nm light. 20-30mW of this light is split off for use in a saturation absorption setup, described in section 3.7, and to an interferometer for calibrating scan widths. The remaining 570mW is mode matched into the second Wavetrain doubling cavity, giving us 80-90mW of laser light at 221.74nm for use in the MOT. Our MOT beam has a $1/e$ spot size of ~ 3.2 mm. Overlapping the beams is accomplished by alignment cards that were made while testing the magnetic field zero and the imaging setup. The beams were first overlapped on the magnetic field zero. Circular cards were then placed snugly inside plastic flange caps and mounted onto the windows of the system. The beams were then outlined on each of the cards to be used as alignment jigs.

The nonlinear crystal needed in order to reach our 222nm wavelength is called Beta-Barium Borate (BBO). This crystal is susceptible to damage when operating in this wavelength regime. We believe that the damage is mostly on the surface of the crystal and we have found that we get extended lifetime when purging our crystals with oxygen gas during operation. With this purge gas, we are able to run for ~ 40 hours at high power before we begin to see decreased performance. At this point, the crystal will generally only give out a maximum of ~ 2 mW of power, regardless of the amount of pump power we send into the crystal. When this happens we turn down the power, move the crystal so that the light hits a different point on the face of the crystal, and then perform a full realignment. When operating the system at low power the crystal can last for hundreds of hours, so for general diagnostics and alignment we typically run our system with ~ 5 mW of power.

3.6.2 Repump Laser

The main repump laser is a system produced by Toptica Photonics. A single frequency external cavity diode laser (ECDL) head is amplified in a tapered-amplifier to produce $\sim 500\text{mW}$ of 1025nm light. This is mode matched into a frequency doubling cavity that produces $\sim 250\text{mW}$ of light at 512.5nm . $10\text{-}20\text{mW}$ of this light is split off for frequency referencing and scan width calibration. The remaining power is mode matched into the next frequency doubling cavity to produce approximately 30mW of power at the repump transition at 256.25nm . This beam is then expanded to match the size of the main cooling beam, $w_0 \sim 3.2\text{mm}$. The repump beam is overlapped with the vertical cooling beam and retroreflected onto itself. The repump laser wavelength has negligible reflection from the 221nm laser mirror coating so they are easily overlapped.

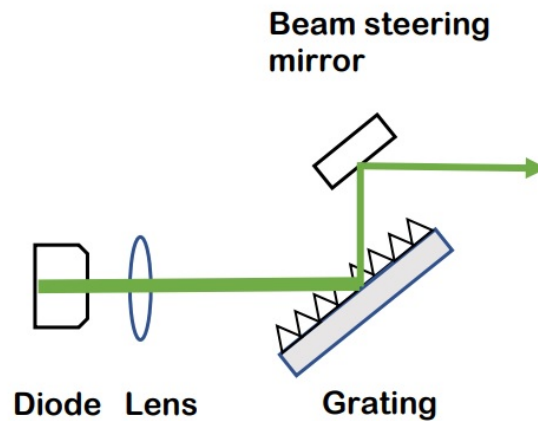


Figure 3.13: External Cavity Diode Laser Schematic: A simple schematic showing the elements in an external cavity diode laser. A laser diode alone does not have the frequency discrimination to be an effective tunable single frequency laser for our purposes. However by creating a laser system utilizing the appropriate frequency discriminating elements, external cavity diode lasers can be tuned for highly precise and accurate single frequency operation.

A simple schematic of an ECDL laser is shown in Figure 3.13 along with the factors contributing to single frequency operation. ECDL lasers have several wavelength selecting pieces in order to force single frequency operation. The first selection comes from the diode itself, which can lase over several nanometers. The next selection comes from the Littrow-mounted diffraction grating.

For different angles of operation, the grating will back reflect particular wavelengths of light with a frequency width of $\sim 50\text{GHz}$. Internal resonator modes based on the cavity created from the length of the diode typically have frequency widths on the order of 10GHz and spaced by $\sim 64\text{GHz}$. The final mode selection is from the cavity defined by the distance between the end of the diode and the diffraction grating itself. These modes have a width on the order of 100kHz and spaced by $\sim 9\text{GHz}$. The external mode with the most initial gain will cause the gain of the other modes to decrease until the laser operates in a single frequency defined by this external mode. It is the job of the user to overlap all these competing modes in order to select the frequency of interest.

In practice, these modes of operation will not line up nicely in frequency space. The entire ECDL system is temperature controlled, and each individual element will shift asynchronously in frequency as a function of temperature. Because of this, there will exist a temperature set point such that all of these elements will overlap in frequency space. It is the job of the user to find this temperature set point.

The laser system is controlled by an electronics box that houses control systems for this thermal stability. In addition to the thermal controllers, the electronics also contain systems for coherent single frequency scanning of the laser. The external and internal modes of the laser will shift in frequency as a function of current, but these modes will also shift at different speeds. This can lead to mode competition and multi-mode operation, meaning that the laser will not be operating at a single frequency. Feed forward circuits in the control electronics can compensate for this by slowly changing the external cavity length controlled by a small piezoelectric material mounted to the grating. Properly tuned, this feed forward system can allow the laser to scan for over 30GHz of continuous single frequency operation. The response of the following frequency doubling cavities is fast enough to hold these cavities on resonance with the master laser for the duration of the scan.

3.7 Saturated Absorption Spectroscopy

All of our reference and locking spectra are generated using a Saturated Absorption (SA) Spectroscopy setup. A schematic of the optical setup is shown in Figure 3.14. [49] The technique is

useful for obtaining spectra that is free from Doppler broadening effects without cooling the sample. First, a strong beam (called the pump beam) is passed through a cell in order to saturate atoms along the path into the excited state. Then, a pair of beams (probe beams) at the same frequency as the pump beam is sent through the cell propagating in the opposite direction. One of these beams is used as a reference, while the other beam is overlapped with the pump beam.

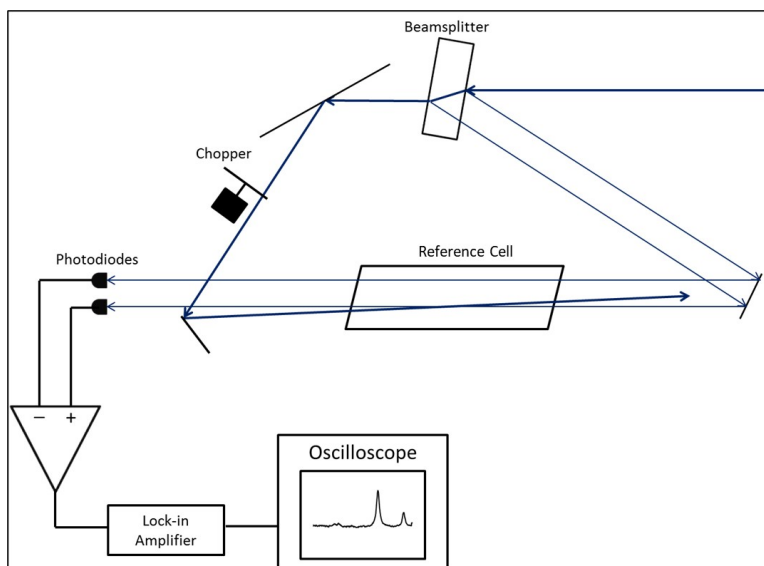


Figure 3.14: Saturated Absorption Spectroscopy Setup

This pair of beams is then sent to a pair of photodiodes and the signal is read out on an oscilloscope. The molecular resonances that we are interested in are rather weak, so we use Lock-in amplification in order to resolve them. When the laser passes over a transition resonance, the pump beam will saturate molecules along its path in the excited state. The overlapping probe beam will see a decrease in signal, showing up as a dip on the oscilloscope. The other reference beam will not see a decrease in signal, but will see the Doppler broadened spectra. This is used to subtract off any laser noise, as well as the Doppler broadening of the resonance of interest. Because the pump beam and the probe beams are counter propagating, the dip will occur only for molecules that have a near zero velocity along the direction of the beam axis. These molecules still have a velocity based on the temperature of the sample, however this velocity is perpendicular to the

laser propagation direction. With this technique you are able to observe the natural linewidth of the transition at temperatures much higher than needed in order to observe Doppler-free spectra.

Chapter 4

Experimental Investigations and Results

In this chapter I will discuss the data gathered over the course of the experiment and the analysis that followed. Section 4.1 discusses the verification of the silicon transition frequency and the development of a tellurium reference used for locking the laser. Section 4.2 explains how we characterize our atomic beam by probing along different directions. Section 4.3 explains the absolute frequency reference used for the main cooling transition. Section 4.4 considers the repump transition uncertainty and our development and identification of molecular reference spectra with a survey of hyperfine spectra in the region for two molecular isotopes of Iodine. Section 4.5 explains our attempts at creating a magneto-optical trap (MOT) and discusses the implementation of improvements to the attempt. Finally, Section 4.6 reevaluates relevant trapping parameters and discusses our testing of the Zeeman slower under different power, current, and polarization conditions, as well as what we expect from simulations of the system.

4.1 Silicon Spectroscopy

As discussed in Section 3.2, our atomic beam has a broad distribution of velocities in the longitudinal direction. In order to get an accurate measurement of the atomic transition frequency, we must minimize any effects from atomic motion from our atomic beam source. In the transverse direction however, the velocities follow a regular Gaussian distribution with a very narrow spread in the velocity spread.

The vacuum system was set up so that a laser beam could enter the trapping chamber from the bottom, transverse to the longitudinal atomic beam motion. This laser was retroreflected back onto itself from a port on the top of the chamber. The arrangement is shown in Figure 4.1. A photomultiplier tube (PMT) mounted on one of the side ports was used to collect the fluorescence emitted by the excited atoms. (This PMT was later replaced by the CCD camera system) The orthogonality of the laser beam and the atomic beam was checked with the PMT signal. If the

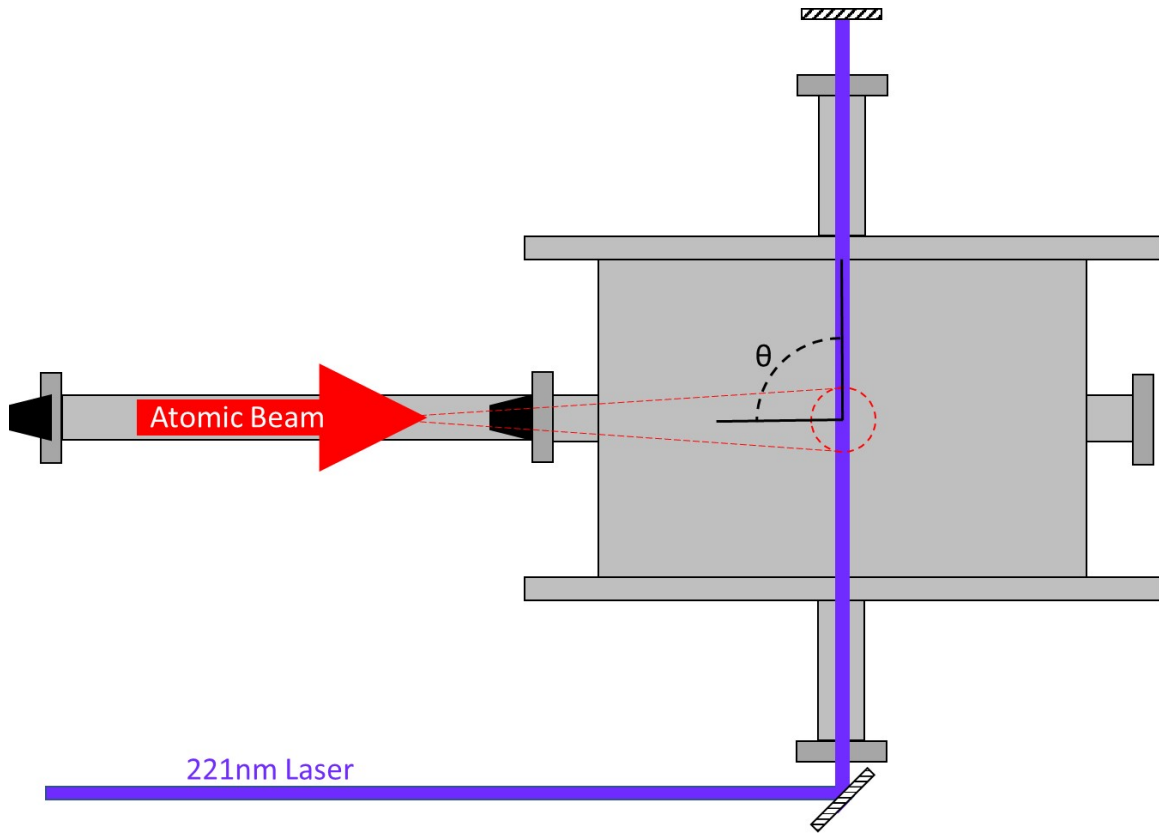


Figure 4.1: Transverse Beam Geometry: Silicon spectroscopy setup with transverse laser beams.

laser beam and its retroreflection were not perfectly perpendicular to the atomic beam, then there would be a small longitudinal Doppler shift introduced into the spectrum. This would lead to a double-peaked signal when the laser was scanned across the resonance, due to the opposite longitudinal Doppler shifts from the two laser beams. The incident angle of the laser beam and its retroreflection was adjusted, and a second frequency scan was taken. This procedure was iterated until the two peaks started to merge and the narrowest line was obtained. In order to ensure that we had minimized the linewidth, we took a series of runs with the retroreflected beam on, and with the retroreflected beam blocked. If the runs with the retroreflected beam on had a larger full-width-at-half maximum (FWHM) than the runs with the retroreflected beam blocked, then we adjusted the angle of the incident beam, realigned the retroreflection, and then repeated a series of runs until these widths had no observable difference. A silicon spectrum obtained in this way is shown in Figure 4.2. The spectrum was fitted with a Gaussian profile, and a FWHM of 122

MHz was obtained. The Gaussian linewidth arose from atoms leaving our atomic beam source with a small amount of transverse velocity, dictated by the geometry of the exit channel. The line fitting to obtain the transverse velocity spread of the atomic beam will be discussed in detail in Section 4.2.3.

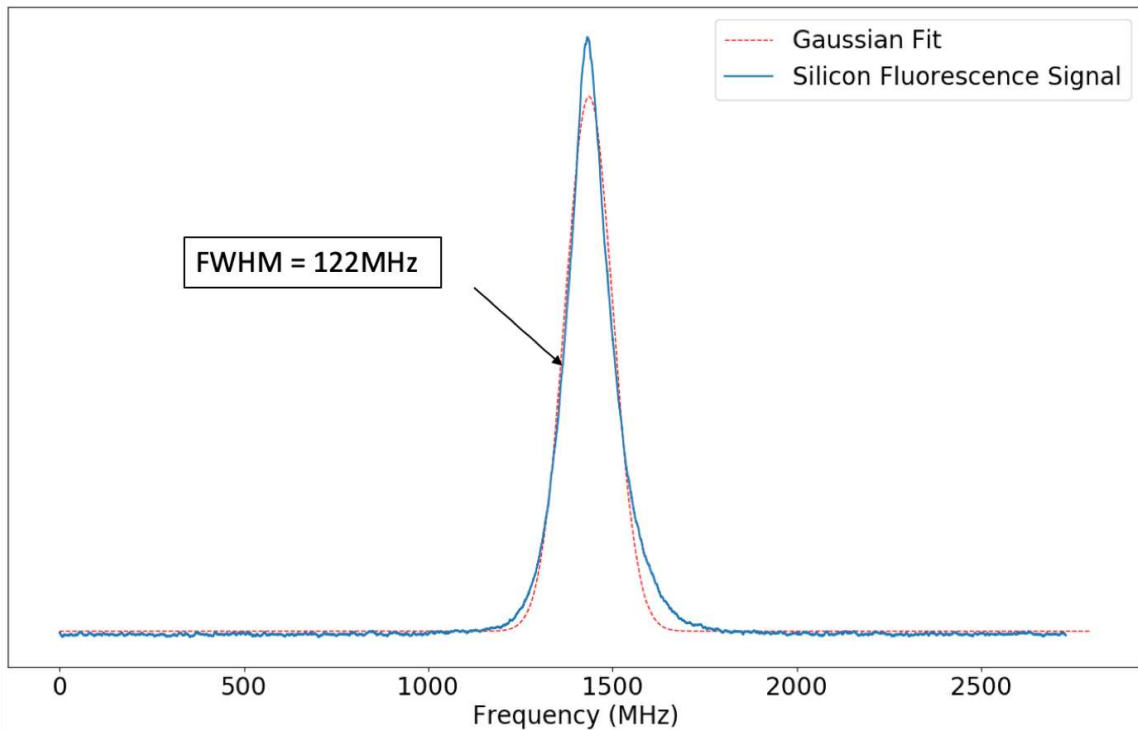


Figure 4.2: Transverse Silicon Fit: Shown is data taken from a photomultiplier tube and a fit of that data, showing that our atomic beam has the divergence given from the geometry of the system. This peak has a full width at half maximum (FWHM) of 122MHz, corresponding to a velocity spread of 27m/s.

One could also find the Doppler-free resonance value by purposely misaligning the vertical beam and its retroreflection in order to split the signal into two distinct peaks. The natural resonance would then exist between these two peaks. Using this method proved somewhat problematic and was only used as a double check for our wavelength measurements.

We verified the silicon transition wavelength by measuring the fundamental laser wavelength with a home-made wavemeter utilizing a traveling Michelson interferometer with phased-locked fringe multiplication. [50] The instrument had a precision of 30MHz that was translated into

120MHz, or 0.004cm^{-1} in the deep ultraviolet. We found that our measured value was in agreement with the NIST tables. [30]. We were able to reliably set the laser at the proper frequency for operations and experiment without issue.

The Gaussian width in the detection region is larger than the natural linewidth of 7.2MHz, dictated by the geometry of the system and the oven exit channel. Nevertheless it allowed us to locate the silicon transition line center to within 2MHz precision. This would be important when we performed the MOT investigation, where we would need to detune the cooling laser precisely by one to several natural linewidths to the red of the transition.

4.2 Characterization of the Silicon Atomic Beam Source

4.2.1 Temperature Considerations

In order to characterize the performance of our atomic beam source, there are several things that we must investigate. We first need to verify the temperature set point of the commercial MBE source made by Veeco. The Veeco Source has a freestanding thermocouple near the wall of the crucible. It uses this sensor in a feedback loop to maintain constant operating temperature of the source. Our vacuum system is set up to have a line of sight view to the beam source. We can see the face of the source through a windowed port in the trapping region. This is useful for several reasons, including initial aiming of the atomic beam, as a port for laser light needed for the Zeeman slower system, and for temperature confirmation of the source, among others. We use an optical pyrometer with a calibrated filament to confirm that our temperature was accurate. Our window has an anti-reflection coating for 222nm light; this was not an issue for the temperature confirmation. Later in the experiment we had a mirror installed nearby outside this port for steering the Zeeman beam down the path of the beam. This mirror had a highly reflective coating for a 45° incident angle 222nm beam. These mirrors are mostly transparent in the visible regime, but it did give us erroneous temperature measurements when using our pyrometer. Once we began our Zeeman studies it was imperative to remove this mirror when temperature confirmation was needed.

When we initially installed the source, we used a crucible, liner, and cap designed and manufactured by the company. When testing the accuracy of this setup, we found the temperature to be very accurate. Later on, when we began fabricating our own crucible and cap, there was significant deviation from the set point. The incremental change in temperature with the set point was accurate, but there was an offset of approximately 80°C . The source would run hot when compared to the set point. This was not unexpected, the difference is due to the crucible construction. Our design is more robust than the Veeco fabricated crucible with thicker walls. The temperature offset was very consistent over many runs for the same crucible.

4.2.2 Atomic Flux Verification

After establishing the temperature, we measured the atomic flux. Due to the geometry of our system, when atoms reach our detection region they have a high longitudinal velocity and a small but measurable transverse velocity. Atoms show a Doppler broadened resonance in the lab frame. If we wish to measure the flux of all atoms through the detection region, it is advantageous to use the transverse laser excitation geometry discussed in Section 4.1.

In this investigation, the setup was the same as in Figure 4.1, but we replaced the PMT with the CCD system and collection optics discussed in Section 3.5. The system is set up to address only atoms that pass through the detection region. Atoms in resonance with the laser will fluoresce and this fluorescence will be collected and imaged onto the CCD camera focusing plane. Image data was collected in 1s exposure times. We always scanned the laser from lower to higher frequencies, which we refer to as from "red" to "blue". Each CCD time frame corresponded to different laser frequency and fluoresced with atoms of a corresponding Doppler detuning in the transverse direction. In order to accurately measure this transverse motion, the laser must be perfectly perpendicular to the atomic beam ($\theta = 90^{\circ}$) so that the spectra was not artificially broadened due to the very large longitudinal velocity. The alignment procedure was discussed in Section 4.1.

When the laser beam was at an angle to the atomic beam, the signal was altered. Consider the case when $\theta \gtrsim 90^{\circ}$. The incident laser beam was tilted forward slightly along the moving

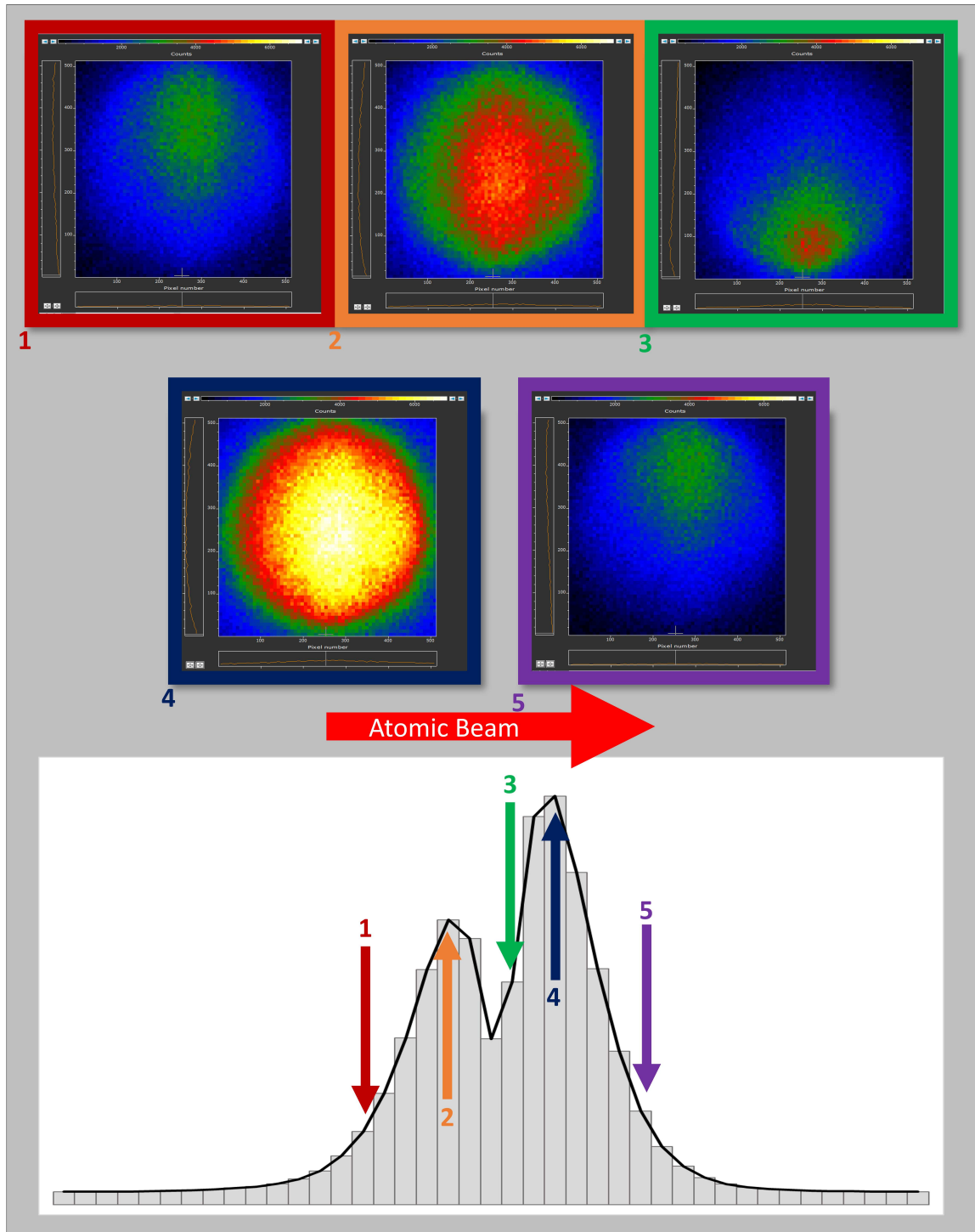


Figure 4.3: Misaligned CCD Spectra: The spectra at the bottom of the figure is found by summing the total counts across the CCD array as we scan through the atomic resonance. The upper images are the raw output from the CCD frame as we scan through the resonance. For this scan, we have θ greater than 90° , allowing for the retroreflected laser beam to come into resonance with atoms at the top of the frame and moving downward, followed by the forward beam coming into resonance with atoms at the bottom of the frame and moving upward. The retroreflected peak is reduced in size due to power losses as it passes through the window, a waveplate, reflection losses of the mirror and back.

atoms and was Doppler shifted down in frequency by the atoms. Therefore it would come into resonance with the atoms at a higher laser frequency than the true atomic transition frequency. The opposite happened with the retroreflected beam. It was up shifted in frequency by the atoms, and would come into resonance at a lower laser frequency. The forward and retroreflected laser beam resonant peak would split in frequency, as seen in Figure 4.3 for the case of $\theta \gtrsim 90^\circ$. In frame 1 we see the downward traveling retroreflected laser begin to come in resonance with atoms moving in the upward direction. In frame 2 we see a maximum signal from the retroreflected laser. These atoms have zero transverse velocity along the direction of the retroreflected beam. Frame 3 corresponds to the true natural resonance, where we see a dip in the signal, as the resonance from the retroreflected laser moves downward and off the screen. As the retroreflected resonance leaves, the forward beam resonance starts at the bottom of the CCD interacting with atoms moving downward. Frame 4 shows this resonance peak from the forward beam, corresponding to atoms with zero transverse velocity along this beam's direction. As we continued scanning we see the resonance move off the top of the CCD image.

When the laser beam is perfectly perpendicular to the atomic beam ($\theta = 90^\circ$), these two resonances will meet in the center at the same laboratory scan time, at the unshifted atomic frequency, and we see an integrated CCD signal as in Figure 4.4. If the atomic beam is perfectly perpendicular to the laser beam, then we should measure a minimum Doppler broadened width. We do not expect any power broadening in the peak, so this width should be the same if we scan with just the forward beam as if we scan the forward with the retroreflected beam. With the retroreflected beam included, we get the added benefit of confirming that atoms moving in both the upward and downward directions are counted and the visual diagnostic of these resonances meeting in the middle of the CCD array. However, for our flux verification calculations we only use the forward beam, due to uncertainties in the retroreflected power. We choose to sum all of the signal counts on the CCD to generate a frequency spectra. After background subtraction we are left with a signal, shown in Figure 4.4, that shows the signal of all the atoms passing through the detection region in one second. By adding together these counts, we are integrating the signal across all detected transverse

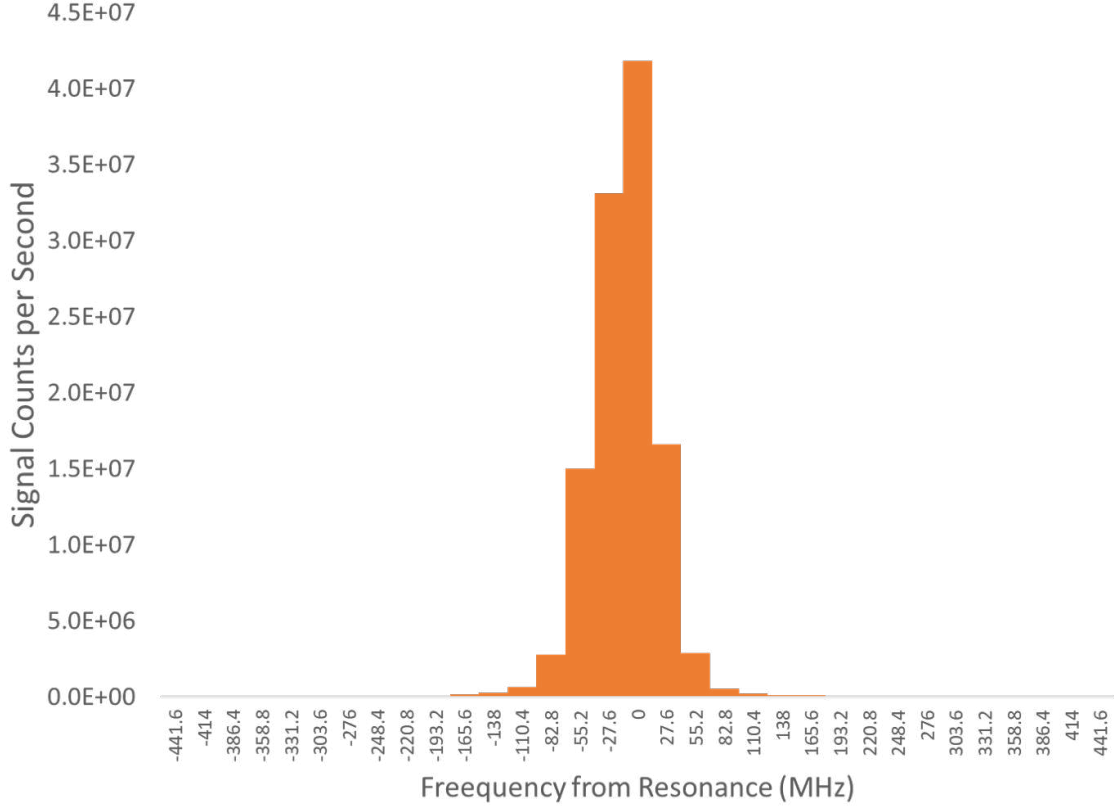


Figure 4.4: Beam Flux Verification Spectra: This figure shows a typical dataset used for beam flux calculations. For our flux verification calculations we only use the forward beam, due to uncertainties in the retroreflected power.

velocities. This gives us the number of counts generated by atoms moving through the laser in the detection region. The volume of that region is given by

$$V = h_{CCD} \cdot A_{laser} = h_{CCD} \cdot \frac{\pi w_0^2}{2} \quad (4.1)$$

where h_{CCD} is the height imaged by the CCD, A_{laser} is the area of the laser beam, and w_0 is the laser spot size. We choose to expose our CCD in 1 second increments so that our signal is normalized with respect to time. From this we calculate the total number of counts per cubic centimeter per second that are detectable in the beam. Equation 3.4 allows us to convert this value to number of photons emitted per cubic centimeter. We next calculate the expected number of photons from a single atom on resonance using Equation 2.1. This allows us to calculate the total

number of atoms per volume. Finally, these atoms are moving longitudinally and the mean value of the velocity is given by

$$\langle v \rangle = 2 \left(\frac{2k_b T}{m} \right)^2 \int_0^\infty v^4 e^{-\frac{mv^2}{k_b T}} dv = \frac{3}{4} \sqrt{\frac{2\pi k_b T}{m}} \quad (4.2)$$

where k_b is Boltzmann's constant, T is the absolute temperature, and m is the mass of the particle. For our operating temperature, 1388°C, this value for silicon is 1315 m/s. Finally we can calculate the flux

$$\Phi_{exp} = \frac{N_{atoms} \cdot v_m}{V} \quad (4.3)$$

Table 4.1: Values Used for the Flux Calculation

P , Vapor Pressure	2.47×10^{-4} Torr
A_s , Source Area	$\pi(0.05\text{cm})^2 = 7.85 \times 10^{-3}\text{cm}^2$
l_0 , Distance to Detector	75cm
M , Atomic Mass	28amu
T , Temperature	1388°C
Expected Flux	$1.85 \times 10^{10} \frac{\text{atoms}}{\text{cm}^2\text{s}}$

The theory behind calculating the flux of an effusive oven source like ours was outlined in Section 2.3. The molecular beam flux can be written as

$$\Phi = 1.118 \times 10^{22} \frac{P A_s}{l_0^2 \sqrt{MT}} \frac{\text{atoms}}{\text{cm}^2\text{s}} \quad (4.4)$$

where P is the vapor pressure in Torr, A_s is the source area in cm^2 , l_0 is the distance to the detector in cm, M is the atomic mass in amu, and T is the temperature in Kelvin. [41] Parameters used for our calculation can be found in Table 4.1. The vapor pressure is a function of temperature, and there is a convenient online calculator for determining the pressure value for many atoms and some molecules found in Reference [48]. We ended up performing this test many times, and repeatedly

saw the detected atomic flux was always low from the theoretical value. A selection of runs and their calculated versus theorized values are shown in Table 4.2.

Table 4.2: Results for atomic beam flux measurements compared to expected values

Dataset	Measured Flux ($\frac{atoms}{cm^2s}$)	Flux Reduction ($\frac{Measured}{Ramsey}$)
2-17-2017/si_5	1.50×10^{10}	0.813
2-17-2017/si_6	1.26×10^{10}	0.682
2-28-2017/si_1	8.01×10^9	0.434
3-2-2017/si_1	7.24×10^9	0.392
3-3-2017/si_1	5.27×10^9	0.285
3-7-2017/si_1	4.88×10^9	0.264
3-7-2017/si_2	4.23×10^9	0.229
3-15-2017/si_1	4.73×10^9	0.256

We see in this data that the observed flux is reduced rather quickly and then begins to stabilize. We attribute this to the molten silicon flowing into the walls of our crucible and creating a layer of silicon carbide on the surface of the crucible. This reduces the amount of free silicon atoms while also creating a surface that no longer reacts with the remaining silicon at the operating temperature.

4.2.3 Velocity Distribution Measurements

After determining the total flux, we need to check that the atomic velocity distribution is behaving as expected. When analyzing atomic beam velocity distributions, there are two separate distributions that can give information about the atomic beam performance. There is the longitudinal velocity distribution along the direction of travel of the beam as well as the transverse velocity distribution along the direction perpendicular to the travel. In the transverse direction, we expect Doppler broadening of the atomic resonance, which should result in a Gaussian lineshape. [41] The spread in this direction shows us how well we are able to collimate our atomic beam. Figure 4.5 shows the geometry of our beamline relevant to the transverse distribution measurement. The limiting aperture occurs at 60cm after the atomic beam source with a diameter of 1.27cm. Figure 4.2 shows a fit to data taken at a temperature of 1388°C. At this temperature, the mean value of the forward velocity is 1315m/s. From the geometry of the limiting apertures we expect a

velocity spread of $\Delta v = 27.5\text{m/s}$. The frequency width that we expect from this velocity is given by $\Delta\nu = \Delta v/\lambda = 120\text{MHz}$ which matches well with our Gaussian fitted value of 122MHz as shown in Figure 4.2.

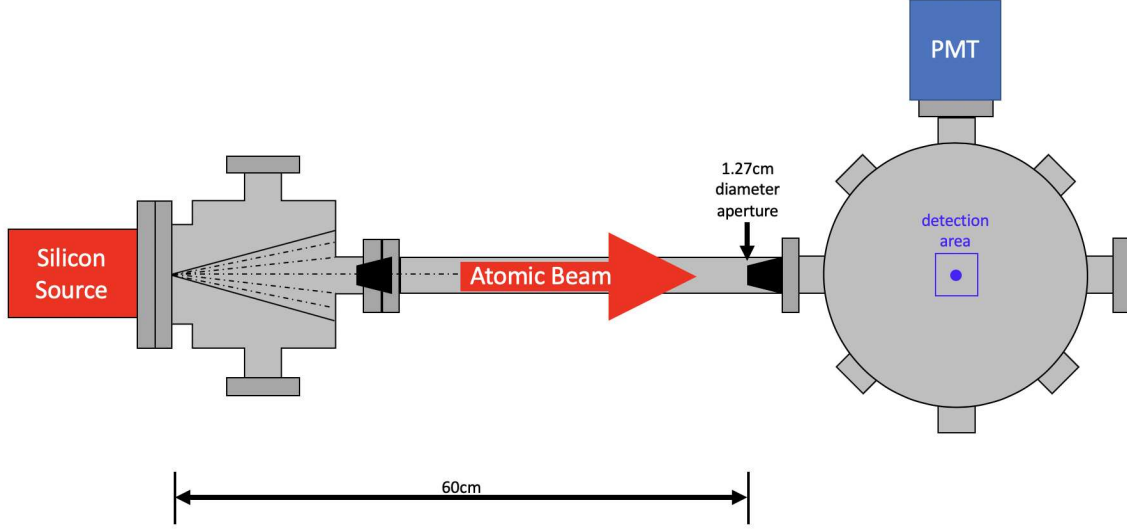


Figure 4.5: Atomic Beam Geometry in the Horizontal Plane: This figure shows the location and size of the limiting aperture in our atomic beam.

In order to probe the longitudinal velocity distribution, we needed to scan a laser through our main cooling resonance at an angle in order to see the longitudinal Doppler profile. Our vacuum system has a windowed port at 45° to the direction of the atomic beam travel. We used this port to scan our laser, and detected fluorescence on our CCD imaging system. We expect our velocity distribution to follow the form of Equation 2.7. The detected signal on the CCD would be proportional to this equation times the travel time across the viewable area of our CCD, $t_{trav} = \frac{1\text{cm}}{v}$, where v is the velocity of the atom being addressed. This give us a detected signal of the form

$$\mathcal{S} = \mathcal{A} v_d^2 e^{\frac{-mv_d^2}{2kT}} \quad (4.5)$$

where m is the mass, k_B is Boltzmann's constant, T is the absolute temperature, $v_d = \left(\frac{v_l}{\cos \theta}\right)$ is the detected velocity and v_l is the longitudinal velocity of interest, and \mathcal{A} is a constant that depends

on the atomic flux. For this analysis we left \mathcal{A} as a free parameter and only analyze the velocity distribution as a function of temperature. A typical fit is shown in Figure 4.6 and the peak location agrees well with the temperature readings from the optical pyrometer.

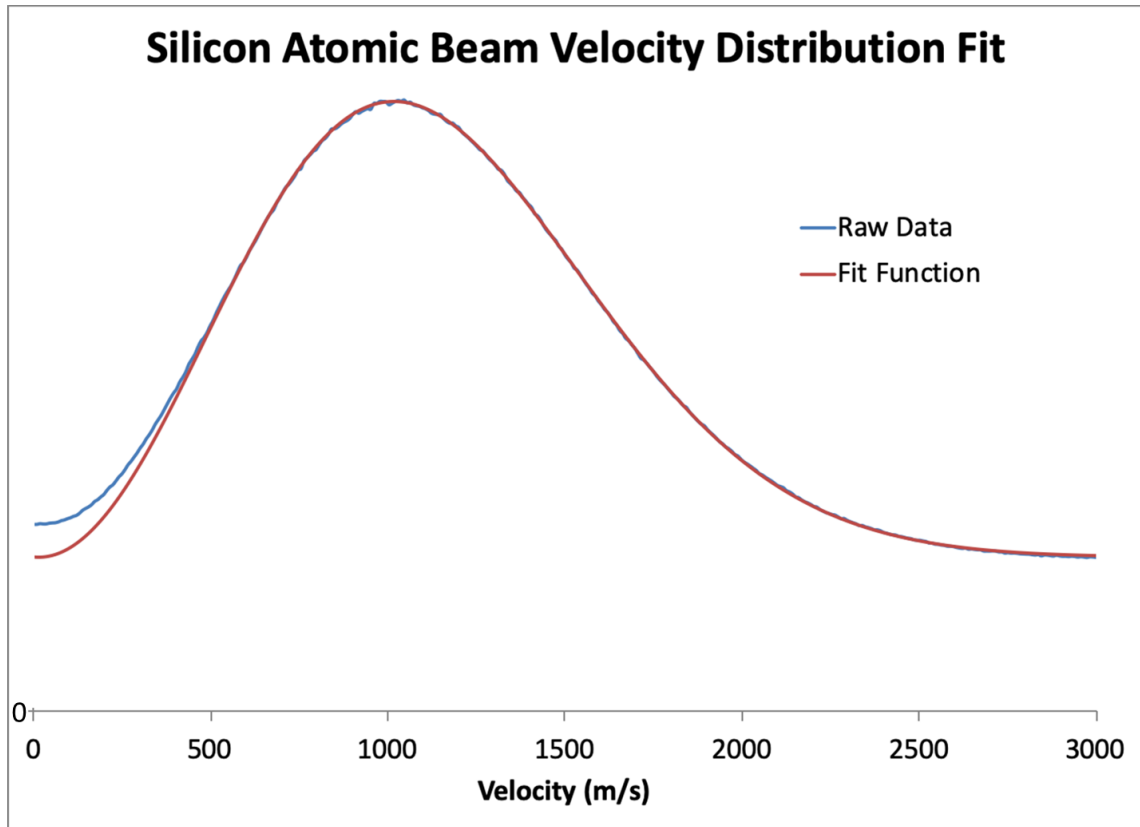


Figure 4.6: Silicon Atomic Beam Velocity Fit: Shown is data taken from a CCD and a fit of that data, showing that our atomic beam has a temperature of 1409°C. This temperature agrees with our optical pyrometer reading.

4.3 Frequency Control of the Cooling Laser System

Precise frequency control of the cooling laser is needed for forming a MOT. The red detuning from line center needs to be set at a fixed amount that is generally on the order of the natural linewidth of the atom to be trapped. In many MOT experiments, the frequency reference of the cooling laser is provided by using saturated absorption spectroscopy [51] on a spectral cell containing a gas of the atom to be trapped. Typically a small portion of the cooling laser is split off and

sent through an acousto-optic modulator (AOM) for the reference beam in the gas cell. This signal can then be processed and fed back into the laser to hold the frequency at a particular detuning for periods long enough to perform experiments. A gas cell is unfortunately not feasible with silicon due to its high melting point. There is also a lack of available AOMs in the spectral region of our cooling and repump transition wavelengths. We need to find independent frequency references in order to lock and reference our laser systems.

4.3.1 Molecular Te₂ Reference Investigation

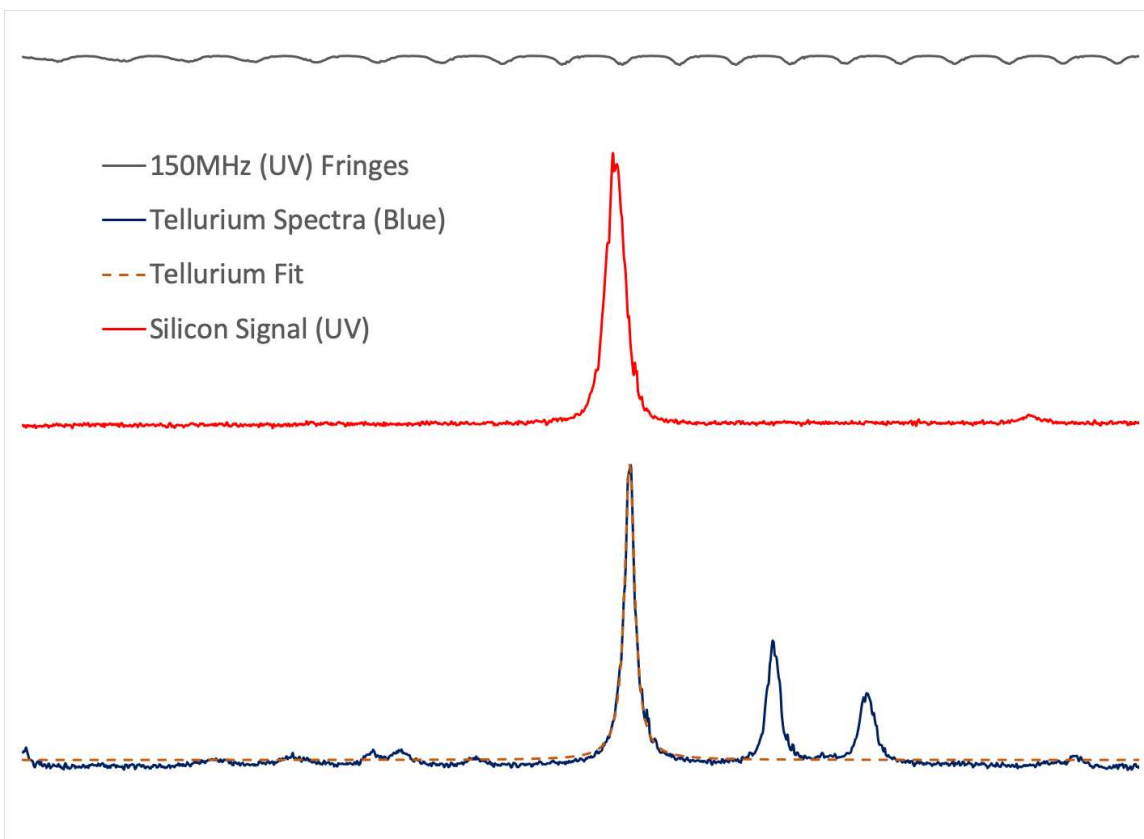


Figure 4.7: Tellurium and Silicon Offset Analysis: Shown is an average over 8 runs that we used to fit the linewidth of our tellurium peak of interest. This data was also used to calibrate the correct offset setting for the acousto-optic modulator.

Since our laser systems employ two stages of frequency doubling to reach our wavelength of interest, we have access to three different wavelength regimes for reference spectra. We chose to

use our second harmonic output for reference spectra. There are many different candidates with well known spectral features in the region, something that our DUV wavelength does not have. AOMs are readily available and robust in this spectral regime as well.

The first stage second harmonic generation in our cooling laser system has a wavelength of 443.48nm. In the blue spectral region, diatomic Tellurium gas has many molecular lines that can be used as frequency references. We initially purchased an isotopically pure molecular cell of $^{130}\text{Te}_2$ for our search for references. Tellurium is a solid metal at room temperature. We built an oven using insulating firebricks around clam shell heaters to heat the cell to the 540°C temperature needed to produce a vapor for the saturated absorption setup. This cell did not have any resonances in the spectral region needed for referencing and locking the silicon cooling transition. We replaced this cell with one that had a natural isotope mix of tellurium. This cell had several lines near half the frequency of the silicon transition, and we found one line that we could reach by acousto-optically shifting our reference beam so that it overlapped the cooling transition. Figure 4.7 shows the tellurium spectra in the region, as well as the shifted tellurium spectra used to lock the laser.

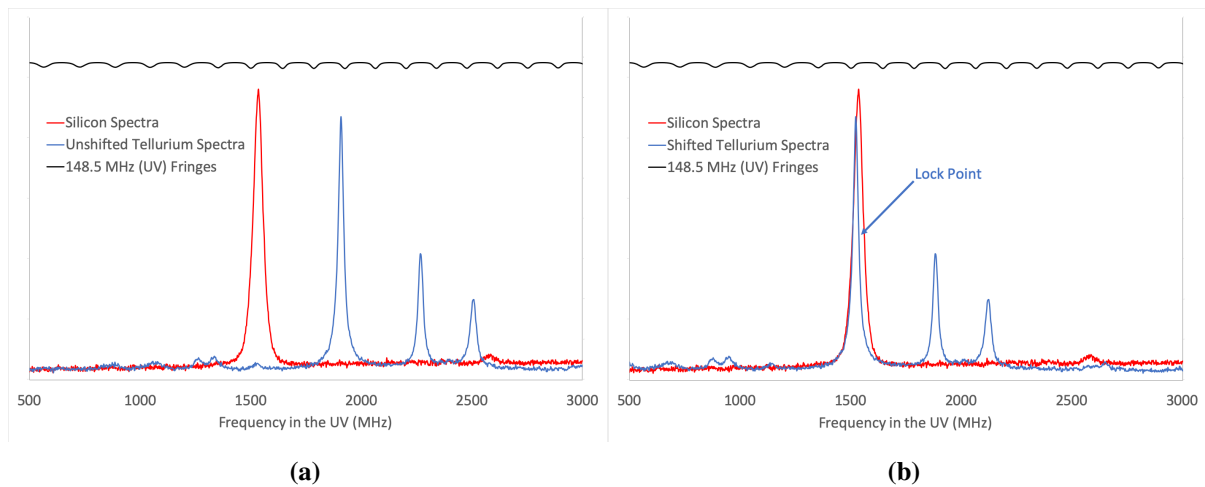


Figure 4.8: Te_2 Spectra: (a) A plot showing the unshifted Te_2 spectra in the region of the silicon peak. The horizontal axis has been scaled to show frequency changes in the UV regime that has been calibrated using fringes from a confocal cavity, shown above the spectra. (b) A plot showing the placement of the tellurium peak when shifted by double passing the blue beam through an acousto-optic modulator (AOM).

We need to determine the exact value of the frequency offset between the tellurium transition and the silicon transition. We use the half maximum value on the high frequency side of the transition as the laser lock point. The slope of a Lorentzian at this point is the maximum value divided by the full width. Figure 4.8 shows an average of 8 runs that we used to establish the FWHM of the tellurium line of interest, as well as establish the proper shift frequency for our lock point. The frequency needed for this overlap is 192.95MHz, corresponding to a detuning from the silicon resonance by $-13\text{MHz} = -1.8\Gamma$. The interferometer fringes above the spectral plots come from a 1 meter long confocal cavity that is temperature controlled. It is very stable with a free spectral range of 72.2433816(66) MHz in vacuum. [52] This interferometer was used for all of our frequency calibrations, with corrections for the refractive index of air in our lab conditions.

4.3.2 Locking the Cooling Laser to the Tellurium Reference

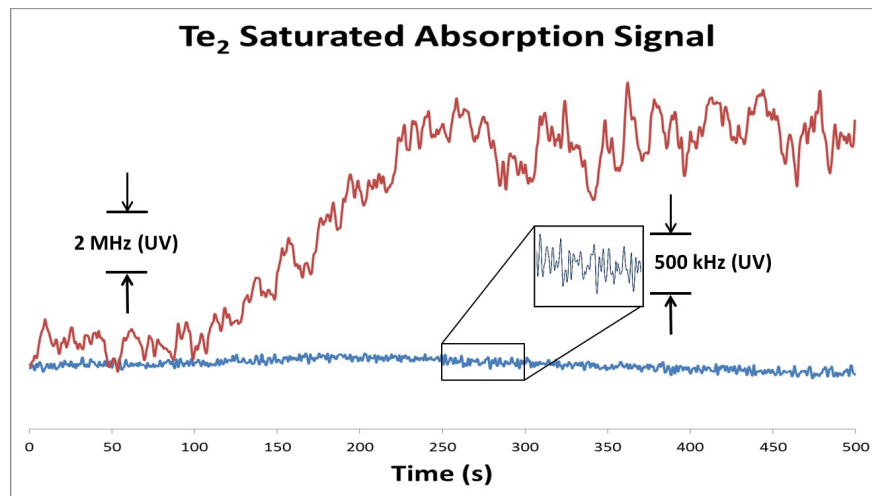


Figure 4.9: Te₂ Lock Signal: The red trace shows the signal from the Tellurium SA setup when the laser is allowed to drift on its own while the blue trace shows the signal when the lock is engaged.

In order to lock the laser, the Tellurium peak signal was processed. We choose to lock on the half maximum point on the high frequency (blue) side of the peak, as indicated by the arrow in Figure 4.7. We biased the signal with a DC voltage so that the lock point occurs at 0 Volts. We then send this voltage to a simple PI amplifier and feed this output into the scan control of the

master Ti:Sapphire laser control box. When the laser begins to drift to higher frequencies, the signal from the Tellurium cell feeds lower voltage into the scan control, which will push the laser back to the lock point. When the laser begins to drift to lower frequencies, the signal from the Tellurium cell feeds higher voltage into the scan control, which will push the laser back to the lock point. By controlling the gain of the feedback signal, we can control how tightly the laser stays on the lock point. If this gain is too high, then the laser corrects too quickly, which can lead to higher oscillations on the locking signal. If the gain is too low, then the laser will drift too far away from the lock point for the signal to totally correct the frequency drift, and we lose the lock. For the magneto-optical trapping, I needed this lock to hold for a minimum of 500 seconds while I scanned through the repump transition. In practice, the lock was able to hold for up to an hour. A typical lock stability plot is show in Figure 4.9. The cooling laser frequency is controlled to $\sim 500\text{kHz}$, sufficient for holding the detuning of the MOT.

4.4 Repump Transition Investigation

In our cooling scheme, there is a weakly coupled transition linking the 3D_3 excited state to a lower lying 1D_2 metastable state. As discussed in Section 2.1, there is sufficient coupling to our cooling excited state to limit the trap lifetime. We decided that this state would need to be addressed. A laser tuned to the correct frequency can excite atoms in the 1D_2 state back to the 3D_3 excited state where it can be addressed by our main cooling laser again, closing this potential leakage channel. With the inclusion of this repump transition, our cooling cycle is now closed, and the trap lifetime should be limited only by collisions in the trap region.

Table 4.3: Silicon Energy Levels for the Repump Transition, and their Uncertainties

Excited State Wavenumber	$45,321.848\text{cm}^{-1}$
Excited State Wavenumber Uncertainty	$\pm 0.005\text{cm}^{-1}$
Ground State Wavenumber	$6,298.850\text{cm}^{-1}$
Ground State Wavenumber Uncertainty	$\pm 0.006\text{cm}^{-1}$
Repump Transition Wavenumber	$39,022.998\text{cm}^{-1}$
Combined Transition Uncertainty	$\pm 0.008\text{cm}^{-1}$
Combined Transition Uncertainty	$\pm 240\text{MHz}$

Since this transition has never been observed, we need to find an absolute frequency value as well as an appropriate uncertainty in order to decide the frequency regime to explore in our system. Table 4.3 reports the vacuum values of the energy levels and the appropriate uncertainties from reference [53]. In 1967, Radziemski and Andrew teamed up with Kaufman and Litzén to do a reanalysis of the arc spectrum data used in the NIST tables for silicon lines found in reference [54]. This new set of data has greater internal consistency, and it shows in the reduced reported uncertainties for the energy level designations. Taking the difference of these levels will give us a transition frequency, and combining the uncertainties in quadrature will give us a frequency spread in which to search. In order to ensure complete overlap during our experiment we doubled this uncertainty in our investigations to $\pm 500\text{MHz}$.

To ensure that we hit our repump transition, we use an absolute reference in order to know our position in frequency space. Due to limited power in the DUV output from our laser, it is advantageous to isolate a portion of the first SHG cavity output to use as a reference. This wavelength is approximately 512.52nm. Molecular spectra of $^{127}\text{I}_2$ are known to high precision and accuracy in the region and are very useful as a frequency reference. [55] In order to leverage this precision, we initially used a $^{127}\text{I}_2$ cell in a saturated absorption setup with lock-in detection to search for reference hyperfine transitions in the region of interest. We first identified lines in the $^{127}\text{I}_2$ spectra from the spectral atlas [55] to ensure the accuracy of our I_2 spectra and line identifications. The procedure for identification of these lines will be presented shortly.

Once this accuracy was established, we found there was a gap in the spectral region where we were interested in probing for the repump laser. The peaks that we did find were too far away to shift any lines near the region of interest using an AOM. We then used a cell with $^{129}\text{I}_2$ in our scans, and found several candidate lines to use as frequency markers. We linked the atlas of $^{127}\text{I}_2$ to $^{129}\text{I}_2$ by performing a dual scan of both isotopes simultaneously. A plot of the spectra of $^{127}\text{I}_2$ and $^{129}\text{I}_2$ in the repump region is shown in Figure 4.10. We performed a high resolution survey of transitions of $^{129}\text{I}_2$ in the region of $\pm 17\text{GHz}$ (UV) from the expected repump transition frequency

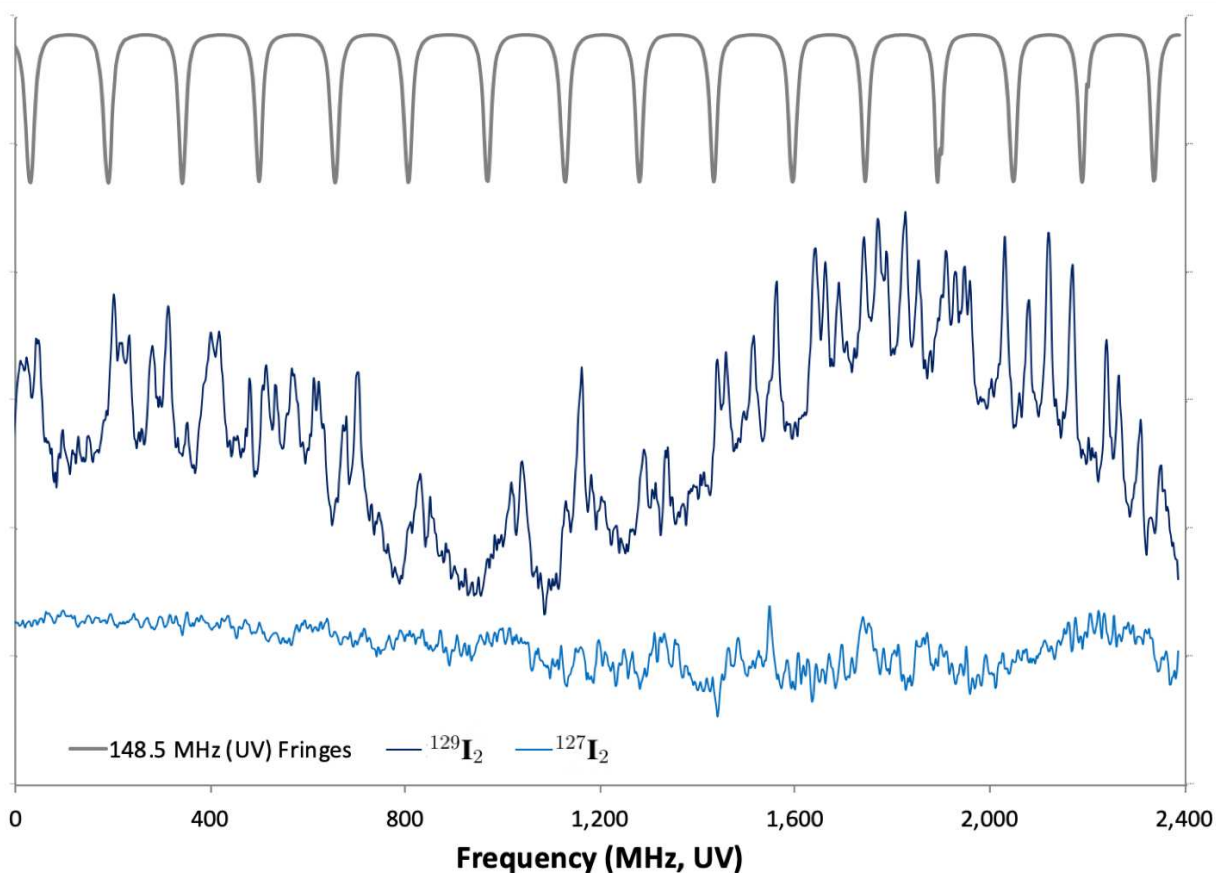


Figure 4.10: $^{127}\text{I}_2$ and $^{129}\text{I}_2$ Spectra using the first harmonic output of the Repump Laser in the region of interest. Note that the frequency scale is in UV values for comparison with the repump transition. The laser frequency range in this scan is actually half, 1200MHz.

in our attempts to identify the transitions. Plots of spectra within $\pm 2\text{GHz}$ of the expected repump transition can be found in Appendix B.

4.4.1 $^{129}\text{I}_2$ Spectra and Referencing the Repump Laser

The following is a discussion on how we identified the molecular lines of $^{129}\text{I}_2$ using the established notation for molecular transitions. It draws largely from References [56] and [57] with some calculations done by our group using data from Reference [58].

We took molecular transition coefficients from Reference [56] and re-scaled them with the appropriate power $l + 2m$ of reduced mass ratio, as described in Reference [57]. We took these coefficients and calculated the frequency of equivalent lines in the $^{127}\text{I}_2$ system. We checked this

for several lines in the region and found good agreement with the spectra that we observed. We used these parameters to identify the transition in Figures 4.10 and 4.11 to use as a frequency marker for our repump transition. Our identification of the line can be found in Table 4.4.

An alternate check was performed using the Dunham constants for $^{129}\text{I}_2$ from Reference [57] and using the centrifugal distortion constant from Reference [56] for the X state and the four centrifugal distortion constants from Reference [58]. Mass ratios for the X state were not corrected for in this calculation because the difference should not be large for low J values, as in our identified transition. When performing this check we found agreement with the previous method to within 0.03cm^{-1} . Due to this discrepancy we extended our frequency uncertainty to $\pm 500\text{MHz}$ for our initial test, eventually expanding the search to $\pm 2\text{GHz}$.

Table 4.4: Iodine-129 Spectroscopic Constants for Silicon Repump Transition Marker

Branch	R ($J \rightarrow J+1$)
J'' , Ground State Total Angular Momentum	26
ν'' , Vibrational Ground State	1
ν' , Vibrational excited state	52
Term Symbol	R(26) 52-1 $^{129}\text{I}_2$

Within this transition there are 28 hyperfine peaks that we can use to monitor our scan region. The molecular term symbol (even or odd J) allows us to calculate a central frequency for the transition, which we then use to experimentally verify frequency shifts for the different hyperfine components. In Figure 4.11 we identify a hyperfine component with a frequency value of 19511.4992cm^{-1} to be used as the center of our exploratory scan, with a $\pm 500\text{MHz}$ (UV) search window indicated on the plot with red arrows.

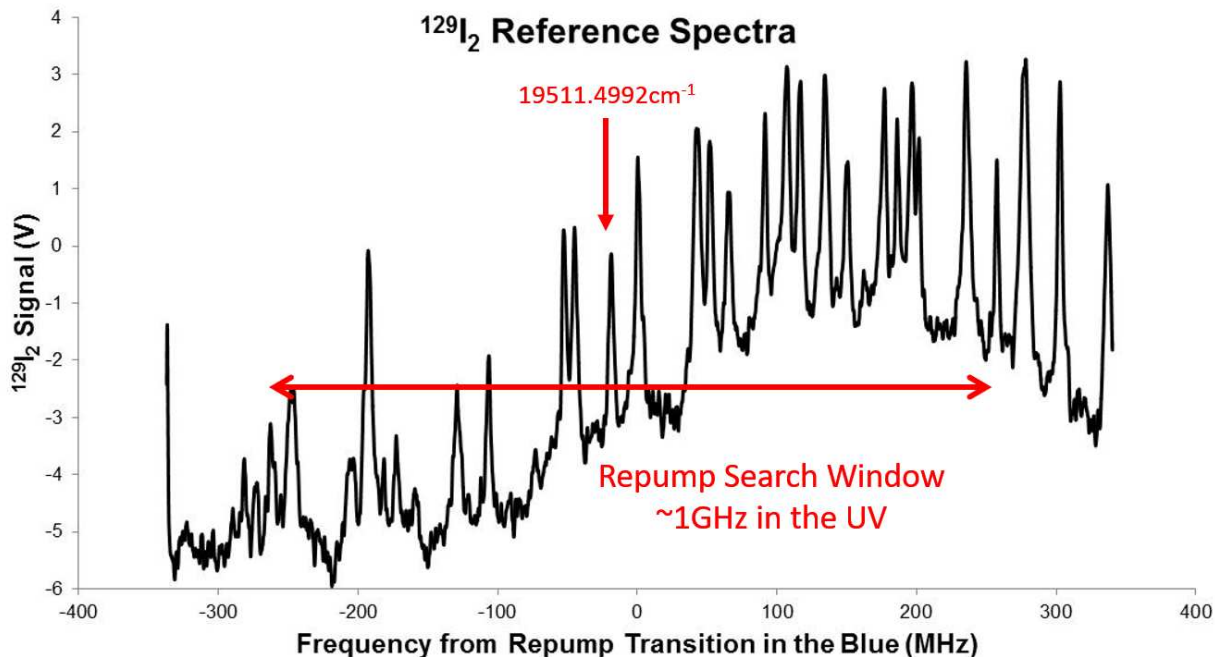


Figure 4.11: $^{129}\text{I}_2$ Reference Spectra using the first harmonic output of the repump Laser. Our repump search window nearly overlaps with the Iodine line identified in Table 4.4

4.5 Magneto-Optical Trap Investigation

Once we had developed our spectrographic references, we began trying for the magneto-optical trap. A literature review showed that detuning values for stable traps vary widely, from some with detunings as small as half the natural linewidth to a dozen linewidths and more. Systems that can handle high detunings typically have easily attainable laser power at the cooling wavelength with low values of saturation intensity. That is not the case for silicon. The difficulty in attaining high laser power leads to an extra layer of control needed in order to form a stable trap. In order to maintain a high enough intensity, our laser spot size is smaller than in most traps. Extra care must be taken to ensure that the laser beams not only cross each other in the trap region, but also overlap with the magnetic field zero. A list of relevant trap parameters for silicon can be found in Table 4.5.

While the high saturation intensity and difficulty of attaining high power lasers at such short wavelengths is a disadvantage for the silicon system, the high photon momentum is a considerable boon. Higher detuning levels will lead to a reduced scattering rate, however the high photon

Table 4.5: Relevant Trap Parameters for Silicon

λ , Vacuum Transition Wavelength	221.74nm
τ , Natural Lifetime	22.0ns
Γ , Spontaneous Emission Rate	$4.54 \times 10^7 \text{ s}^{-1}$
$\Delta\nu$, Natural linewidth	7.23MHz
I_{sat} , Saturation Intensity	$86.8 \frac{mW}{cm^2}$
v_r , Recoil Velocity	$6.4 \frac{cm}{s}$
w_0 , laser spot size	3.2mm

momentum will allow for the scattering force to still be considerably high. These effects combine to allow us to choose trap detunings that are comparable with other near-resonant systems in order to maintain the same scattering force needed to form a trap.

Continuing the calculations discussed in Sections 3.2 and 4.2, we can calculate the rate R at which atoms at trappable velocities will enter the trap region from the atomic beam. In addition to this information, we need to calculate an expected loss rate of trapped atoms. We can then determine the steady state atom number N_s in the trap ($N_s = R\tau$ where τ is the trap lifetime). The following paragraphs discuss these calculations with a summary of values in our system in Table 4.6.

Trap number dynamics evolve following a simple rate equation:

$$\frac{dN}{dt} = R - \frac{N}{\tau} \quad (4.6)$$

where N is the number of atoms in the trap, R is the rate at which those atoms are loaded into the trap, and τ is the time constant associated with trap losses. The solution takes the form:

$$N(t) = N_s(1 - e^{-\frac{t}{\tau}}) \quad (4.7)$$

where $N_s = R\tau$ is the steady state number of atoms in the trap. The flux calculation from Section 4.2.2 multiplied by the trap capture area will give us the total number of atoms hitting the trap region. If we multiply that by the trappable fraction of atoms we can get our loading rate. Our main cooling laser beams are oriented $\pm 135^\circ$ from the direction of propagation of the atomic

beam. Thus the projected cross section seen by the atomic beam is larger than the cross section of the laser beam by a factor of $\sqrt{2}$. This effective area is given by

$$A_{eff} = \sqrt{2}A_{laser} = \sqrt{2}\frac{\pi w_0^2}{2} \quad (4.8)$$

This will give us the total number of atoms per second in A_{eff} for the entire atomic beam, including all velocity groups. There is a limit to how fast atoms can approach the trap potential without escaping the other end. This capture velocity is given by

$$v_c = \sqrt{\frac{2Fd}{m}} \quad (4.9)$$

where v_c is the capture velocity, F is the force on the atom, d is the diameter of the laser beam, and m is the mass of ^{28}Si . The force is the scattering rate given in Equation 2.1 times the photon momentum, $\hbar k$. [59] For our calculations, we set the total detuning $\delta = 1.62$ natural linewidths (typical MOT experiments use detunings ranging from 0.5 to several natural linewidths) and the saturation parameter $\frac{I}{I_{sat}} = 0.4$, giving a capture velocity of 25m/s, similar to other trapping experiments. [59] Integrating the velocity distribution from zero to 25m/s will give us the fraction of trappable atoms in the beam, multiplying this by the total flux will give us the loading rate, R . For our loading calculations we use a value lower than our expected for the atomic flux, $1.0 \times 10^9 \text{atoms}/(\text{cm}^2\text{s})$ to calculate the expected loading rate of atoms in the trap as a worst case scenario. This gives $R = 32 \text{atoms/s}$.

There are several loss mechanisms that the trap can experience. The largest will be from atoms relaxing to the 1D_2 metastable state from the upper $^3D_3^o$ state of the cooling transition. Atoms in this state will be transparent to the cooling light and will exit the trap. The branching ratio for this transition is theorized to be $\sim 1:5700-7200$, as discussed in Section 2.1. The lifetime of the cooling transition is 22ns, which means the atom should decay into the metastable state in $\sim 0.13-0.16\text{ms}$. Thus $N_s = 0.004$ atoms without repumping. However, if we have a repump laser beam in place, that will close this loss channel. Collisions with gas in the trap chamber would be the next likely

loss mechanism, and we can calculate what that rate would be. The collisional loss rate depends on collisions with background gas, as well as silicon gas from the atomic beam:

$$\frac{1}{\tau} = n_b \sigma_b \bar{v}_b + n_{Si} \sigma_{Si} \bar{v}_{Si} \quad (4.10)$$

where n is the density of scattering particles, σ is the collisional scattering cross section, and \bar{v} is the average velocity. The subscript denotes whether the source is from the background (b) or from the silicon (Si) beam. We have identified nitrogen to be the predominant background gas in our system using a residual gas analyzer (RGA). Reference [60] calculates $\sigma_b = 3.8 \times 10^{-14} \text{cm}^2$ for their rubidium trap with a predominantly nitrogen background and states that it is consistent with $\sigma_b = 3.3 \times 10^{-14} \text{cm}^2$ reported for Na-N₂ collisions. For our calculations we will use $\sigma_b = 3.5 \times 10^{-14} \text{cm}^2$. We can calculate the background particle density using the ideal gas law:

$$n_b = \frac{N}{V} = \frac{P}{kT} \quad (4.11)$$

where P is the pressure of the background gas, k is Boltzmann's constant, and T is the absolute temperature. The mean velocity is given by the expectation value of the velocity of a Maxwell-Boltzmann distribution:

$$\bar{v} = \sqrt{\frac{8kT}{\pi m}} \quad (4.12)$$

The flux of the atom beam is directly measured, and is equivalent to the value of $n_{Si} \bar{v}_{Si}$. Values of the measurement are given in Table 4.2, we will use a value slightly higher value as a limit $\Phi = n_{Si} \bar{v}_{Si} = 2 \times 10^{10} \text{ atoms}/(\text{cm}^2 \text{s})$ to conservatively estimate trap losses from the silicon beam in the calculation. When interacting with a laser field, atoms exist in a superposition state between the ground and excited state that behaves as a dipole. Therefore we use a theoretical equation for resonant dipole-dipole scattering for the silicon scattering cross section: [59]

$$\sigma_{Si} = \pi \left(\frac{4C_3}{m_{Si} v_c \bar{v}_{Si}} \right)^{\frac{2}{3}} ; \quad (4.13)$$

$$C_3 = \frac{3}{4} \left(\frac{\lambda}{2\pi} \right)^3 \hbar \Gamma \quad (4.14)$$

were C_3 is the dipole-dipole scattering constant defined above, m_{Si} is the mass of silicon, v_c is the capture velocity, \bar{v}_{Si} is the mean velocity of silicon in the beam defined in Equation 4.2, λ is the transition wavelength, \hbar is Planck's constant divided by 2π , and Γ is the transition rate. The values found in these calculations are found in Table 4.6. As you can see in the table, scattering of silicon from silicon should be negligible.

Table 4.6: Loading and Loss Parameters for a Silicon MOT

Parameter	Value
ϕ , atomic beam flux	1×10^9 atoms/cm ² s
w_0 , laser spot size	3.2mm
A_{eff} , effective trap area	0.23cm ²
v_c , capture velocity	25m/s
v_{frac} , fraction of trappable atoms (no Zeeman slower)	1.39×10^{-7}
R , loading rate	32 atoms/s
P , chamber base pressure	2×10^{-7} Torr
T , chamber temperature	25°C
n_b , background gas density	6.5×10^9 atoms/cm ³
\bar{v}_b , background gas average velocity	475m/s
σ_b , background gas scattering cross section	3.5×10^{-14} cm ²
C_3 , dipole-dipole scattering constant for silicon	1.58×10^{-49} Jm ³
\bar{v}_{Si} , mean velocity of silicon in the beam	1320m/s
σ_{Si} , silicon scattering cross section	1.74×10^{-14} cm ²
$n_{Si} \bar{v}_{Si}$, silicon flux conservative estimate	2×10^{10} atoms/cm ² s
$1/\tau_{Si} = n_{Si} \bar{v}_{Si} \sigma_{Si}$, silicon loss parameter	3.5×10^{-4} s ⁻¹
$1/\tau_b = n_b \bar{v}_b \sigma_b$, background loss parameter	10.8s ⁻¹
τ , loss parameter	9.3s
$N_s = R\tau$, steady state atom number	3 atoms
<i>signal</i> for a single atom ($\delta=1.62\Gamma$, $s=0.54$)	2325 counts/s
expected CCD signal count ($G_{EM}=300$; sens = 24.2 e ⁻ /count)	6.9×10^3 counts/s

The steady state value of atoms in the trap is given by $N_s = R\tau = 3$ atoms with repumping or 0.004 atoms without repumping. We multiply this by the excitation rate for atoms in the trap, we

will get the number of photons emitted into 4π . From Equation 3.4 we get an expression for the total counts observed on the CCD:

$$\begin{aligned} signal &= \frac{photons_{emitted} \cdot Gain_{EM} \cdot QE_{CCD} \cdot T_{filter} \cdot \frac{\Omega}{4\pi}}{sensitivity} \\ &= \frac{photons_{emitted}}{4750} \left(\frac{Gain_{EM}}{sensitivity} \right) \end{aligned} \quad (4.15)$$

From these calculations, our 16-bit CCD array should see a signal of 6900 counts/s when a MOT is formed. With this knowledge in hand, we proceeded to attempt the trap.

The trap procedure is outlined in the following. We set our oven to just below the melting point of silicon, 1388°C. We scan the frequency of the vertical laser beam only, to observe the fluorescent signal from the silicon beam and ensure the atomic beam is operating as expected. We sometimes perform a longitudinal or 45° frequency scan with the laser if we wish for further atomic beam analysis. During these diagnostic scans, we simultaneously observe the signal from our tellurium molecular cell to ensure the integrity of the tellurium peak used for locking and to guarantee that we are setting the correct laser frequency. Before attempting any trapping we take several series of background images with our CCD camera. We take a single image of the background oven light. We scan through short frequency ranges near resonance of each of our laser beams individually to ensure their location, as well as a scan with all the laser beams. This particular verification became a good diagnostic for unforeseen problems with the oven and trap chamber. We also take an image with all the lasers far off resonant to quantify off resonant background signal levels.

We then lock our main cooling laser to a detuning controlled by our acousto-optic modulator (AOM) frequency. This procedure is outlined in Section 4.3. The frequency-locked trapping light is sent into the trapping region. This is followed by the repump laser, which is overlapped with the vertical beam as shown in Figure 4.12. The laser light from the repump laser has negligible reflection from the cooling beam mirror's specific HR coating. These beams were matched in size, but the repump beam is shown smaller in the figure for clarity. During a run, the repump laser is scanned $\pm 500\text{MHz}$ in the UV over 500 seconds centered on our predetermined repump frequency.

This laser's second harmonic output is simultaneously sent through our $^{129}\text{I}_2$ cell to ensure it is covering the correct frequency range and the signal saved on an oscilloscope. We use our CCD to take 1 second exposures over a series of 500 seconds. The trigger for the repump scanning is tied to the trigger signal for starting the camera exposure sequence.

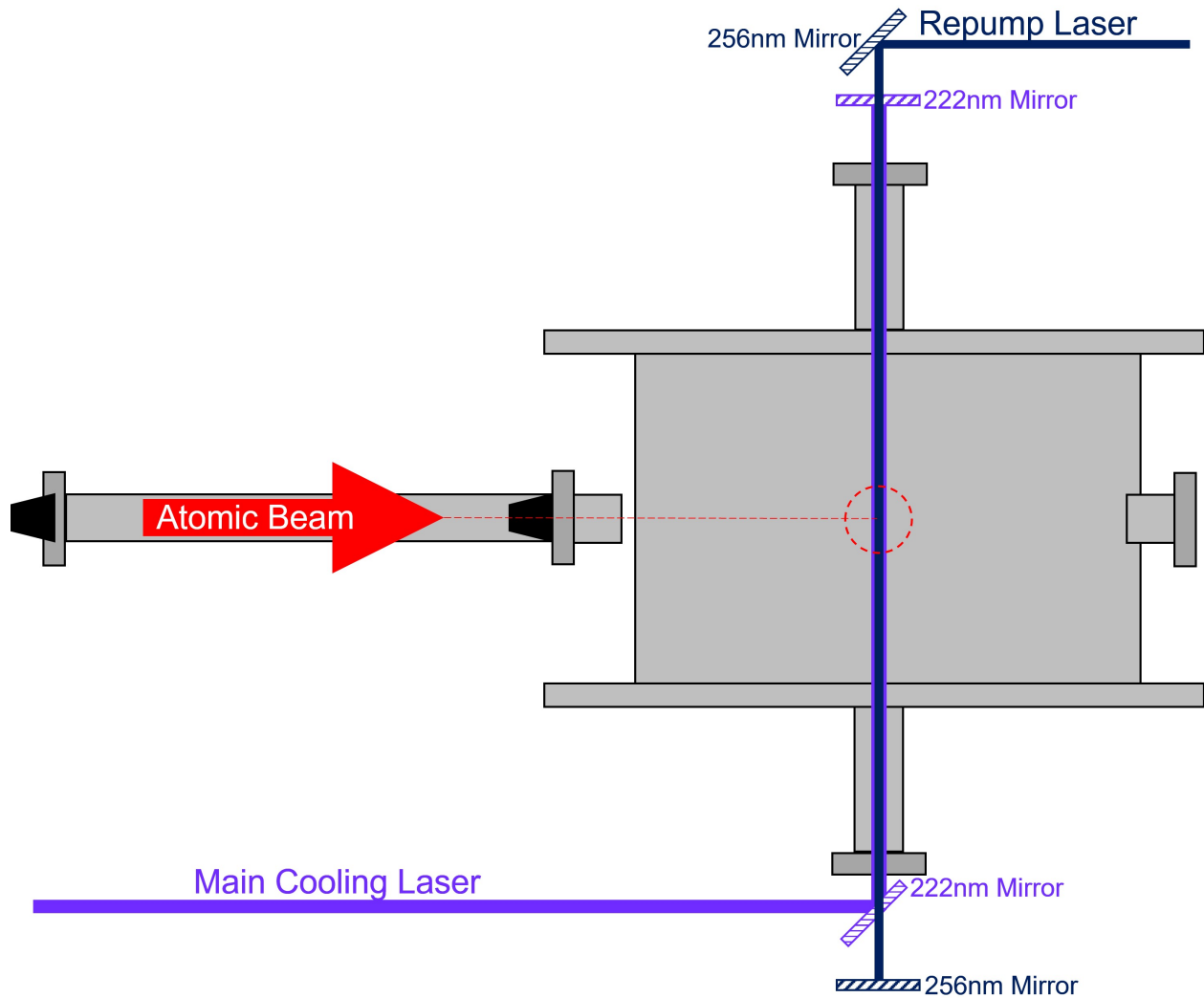


Figure 4.12: Geometry of the repump laser overlap with the main vertical cooling laser. The lasers have matching widths, but are shown here with different widths for clarity. The repump laser has negligible reflection from the cooling laser mirror coating.

For our initial set we chose to lock our laser with detunings ranging from $\frac{\Gamma}{2}$ to 3Γ in steps of $\Gamma/2$ while scanning through the repump transition uncertainty. Each of our horizontal main cool-

ing laser beams had $\frac{I}{I_{sat}} = 0.4$ and our vertical beam had $\frac{I}{I_{sat}} = 0.1$. As discussed in Section 2.4.2, less cooling light intensity is needed in the vertical direction to form the trap, and reducing this intensity greatly reduces the background signal from untrappable atoms in the atomic beam. This background discrimination could also be enhanced by tilting the vertical beam to angle detune the fast atoms completely out of resonance, however our system's limiting apertures in the vertical beam made this impossible in our system. It would also make beam characterization with our vertical beam problematic. Spurious signals from cosmic rays give CCD signals that are comparable to those expected to see in the trap. We marked all candidates and searched for positional coincidence expected for the trap as well as frequency coincidence in the repump laser scan. When none of our attempts passed this criteria in two attempts we repeated the experiment under three more conditions: with the current in the magnetic gradient coils reversed, with the waveplate orientations reversed, and finally with both reversed. When we still did not observe trapped atoms we decided to extend the scan range for the repump transition search. We checked overlapping ranges up to $\pm 2\text{GHz}$ from our original frequency placement for the repump transition and still did not meet our trap criteria. Spectra obtained for $^{129}\text{I}_2$ during this hunt can be found in Appendix B.

This test led us to more complete simulations of our trap conditions, and more refined calculations on our expected trap signal. Initial simulations began in 2 spatial dimensions, along the atomic beam path and perpendicular to it. This was eventually extended to 3 spacial dimensions to simulate the size of the trap ovoid and its capture radius. Parameters considered were entrance velocity and position, laser detuning, laser power, laser spot size, retroreflected laser power loss, trap magnetic field gradient, and gravity. We set the zero point of the system to correspond to the intersection of the laser beams, and placed the magnetic field zero crossing in the same location. We found that for certain parameter sets, the trap could form at a distance of up to $\sim 80\%$ of the laser spot size for weak magnetic field gradients. This is surprising since the intensity of the laser beam at such a position is reduced by more than half. These positions were beyond the edge of the viewing region in our CCD. We decided to retool the collection optics in order to view a larger area, and to increase our magnetic field gradient to pull the trap position closer to the magnetic

field zero point. With these improvements the simulation showed that we should be able to trap atoms up to $\sim 18\text{m/s}$, in line with other magneto-optic trapping experiments. [59] This reduced capture velocity leads to a reduction in the total number of trappable atoms as well as the signal size by a factor of 3.7.

It was this analysis that led to building the permanent magnetic stack outlined in Section 3.4 to increase the MOT B-field gradient and retool our collection optics setup as discussed in Section 3.5. Overlapping the laser beams with the magnetic field zero and focusing the collection optics on that point was a non-trivial task. Adjustable mounting hardware was integrated into the permanent magnet stack and images of a magnetic field probe at the zero point were used to ensure overlap, and the focusing procedure was an iterative process outlined in Section 3.5.

After making these improvements to the system, we repeated the search criteria outlined previously, with the exception of flipping the magnetic field since it is now generated using permanent magnets. Similar scans over the repump wavelength with various cooling laser detunings were done. We did not observe a stable signal from silicon atoms in a magneto-optical trap. A simulation of atomic trajectories at low velocities showed that some of the slowest velocities would not reach the trapping region due to gravity and background reducing apertures placed in the beam line. However these atoms were in such low populations of the total beam flux that it had a negligible effect on our expected trap signal. Direct measurement of the slow atom signal using on axis and 45° laser scans proved problematic due to a residual gas background that made it impossible to resolve the slow atom signal. This can be seen in Figure 4.6. We do not see this background in the longitudinal scans, however measurements in that direction are problematic as the long interaction time with the laser as atoms travel down the system leads to a modified velocity distribution. This effect will be explored in more detail in the next section.

The above MOT runs were done without a Zeeman slower. Low numbers of slow atoms are a problem in many atomic beam experiments, and there are several techniques used in order to increase the flux of these atoms. For our system, we decided to implement a variable-pitch spin-flip Zeeman slower. [42] This technique utilizes a laser beam propagating against the motion of

the atomic beam. Atoms in resonance with the laser will absorb a photon opposite their direction of motion, and then randomly scatter a photon as the excited state decays. Over many photon scattering events, the atom will be slowed along its direction of motion. This will cause a Doppler shift in the atom-laser interaction which will cause the atom to fall out of resonance. In a Zeeman slower, this Doppler shift is offset by a Zeeman shift created with a tailored magnetic field to keep the atom on resonance with the laser. The theoretical details behind the technique can be found in Section 2.4 and the construction details are outlined in Section 3.3. The following section will describe our investigation into our Zeeman slower performance, some interesting signals that we obtained, and our attempts to model the behavior.

4.6 Zeeman Slower Investigation

4.6.1 Zeeman Slower Initial Testing

After finishing with the latest round of magneto-optical trap tests without seeing the formation of a stable trap, we identified that the most helpful improvement would be to increase our slow atom flux. It has been seen in molecular beam sources such as ours, that the flux of slow atoms from a beam source can have a fewer than expected population, typically associated with collisions with the much more highly populated faster atoms. There is precedent for this issue, most famously in the 'Zacharias Fountain' experiments in the early 1950s. [61] We decided to implement a Zeeman slower in order to increase the flux of slow atoms in the trapping region. The theoretical details behind the technique can be found in Section 2.4 and the construction details are outlined in Section 3.3.

The setup for a typical test of a Zeeman slower system is shown in Figure 4.13. A laser is fixed in frequency and sent counter-propagating the atomic beam. As an atom passes through the Zeeman slowing region it will come into resonance with the laser and absorb a photon. It will then scatter a photon in a random direction. After multiple scattering events, the atom will be slowed against the direction of the laser. Due to the change in atomic velocity, the atom will Doppler shift out of resonance with the fixed laser. The Zeeman coil creates a magnetic field that will counter

this Doppler shift with a Zeeman shift. This keeps the atom on resonance with the laser for the remainder of the time spent in the Zeeman slower. With our design atoms should be able to be slowed from an entrance velocity of 200m/s down to a trappable exit velocity of 10m/s.

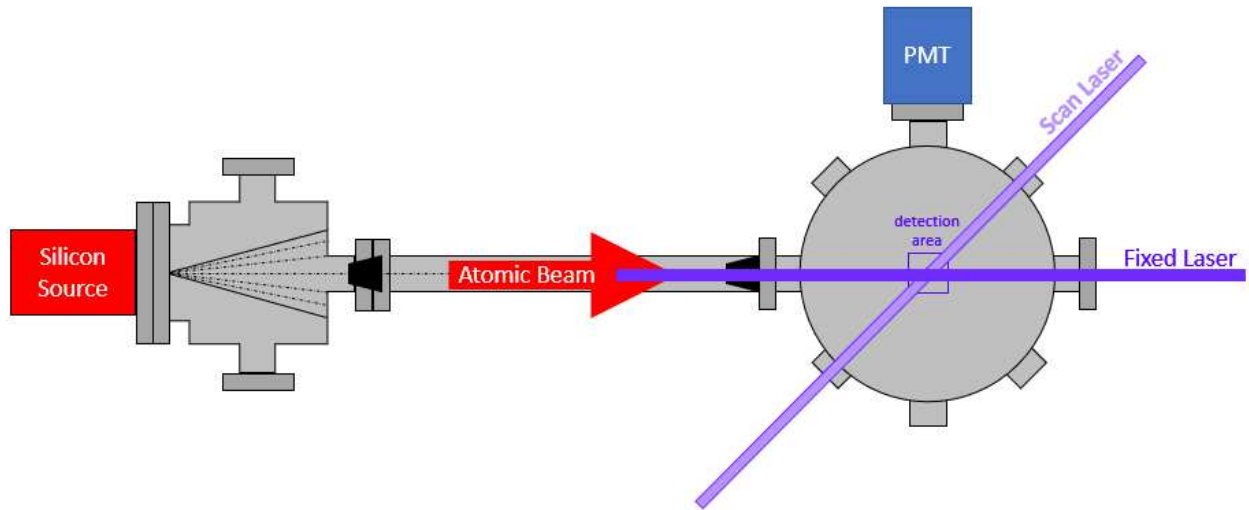


Figure 4.13: Typical Zeeman Slower Testing: In a typical setup, a fixed laser beam is counter-propagated down the Zeeman Slower while an independent scanning laser measures the velocity distribution.

While the Zeeman slower is operating, the velocity distribution is altered from the standard beam distribution. Atoms below the entrance velocity will have their populations emptied and added to the population of atoms leaving at the exit velocity. Normally, an independent tunable laser is used to probe the atomic beam at an angle to measure the velocity distribution in the same way discussed in Section 4.2.3. Unfortunately, our home built laser systems lacked sufficient power to do an independent probe test.

Our initial experimental setup was done using the geometry of the typical setup but with only a single laser. With only one laser, the frequency will be scanned along both paths. For this and all subsequent scans, the total scan frequency was 13.8GHz in the DUV over a scan time of 500s. Equal power was sent to the longitudinal beam and the 45° as an exploratory test. Initially, we

saw no change in the distribution and decided to flip the polarization of the laser from that which is optimal for Zeeman slowing. What we saw is found in Figure 4.14. Around 25-30s there is a strange wiggle in the velocity distribution when the Zeeman current is turned on. This led us to block out 45° beam to isolate the action of the Zeeman slower beam during a scan.

Our next scans are found in Figure 4.15. Using the correct laser circular polarization for the Zeeman slower design, we see that for velocities greater than approximately 500m/s the spectra looks like a typical longitudinal scan without the Zeeman slower. Below 500m/s, there begins a reduction in signal. At 200m/s and below, the signal basically drops to zero indicating that the Zeeman slower is operating correctly. We note that since we use the same laser for cooling and probing, less detected signal means more efficient cooling. However, using the incorrect laser polarization gives rise to an obvious peaking feature at the low velocity end that was not initially expected. This is the result of several processes which I will now explain.

Let us first consider the 0A case. At a particular frequency the laser is in tune with a single velocity class of atoms due to Doppler detuning. As this class of atoms travels down the beam path it will absorb photons from the laser and emit that energy as a photon in a random direction. The transverse motion from the random scattering events averages out and the atom experiences slowing along the path of the laser. This actually changes the velocity class and the Doppler detuning changes. Atoms that were once in resonance with the laser have been pushed off resonance. They will still continue to scatter and slow as they travel down the beam path, but their rates will be reduced lower the longer they travel. By the time they reach the detection region in our setup, they have been pushed far enough from resonance that the signal observed is $\sim 8x$ reduced from what is expected from our beam population measurements. This is happening to a range of velocity classes above and below the initial laser resonance condition, albeit at slightly lower rates at the beginning of the process. As we scan the laser through frequency we can see how all the longitudinal velocity classes will behave. With no magnetic field all the velocity classes behave the same way and the spectra follows the same form as Equation 4.5. The observed signal is the same with

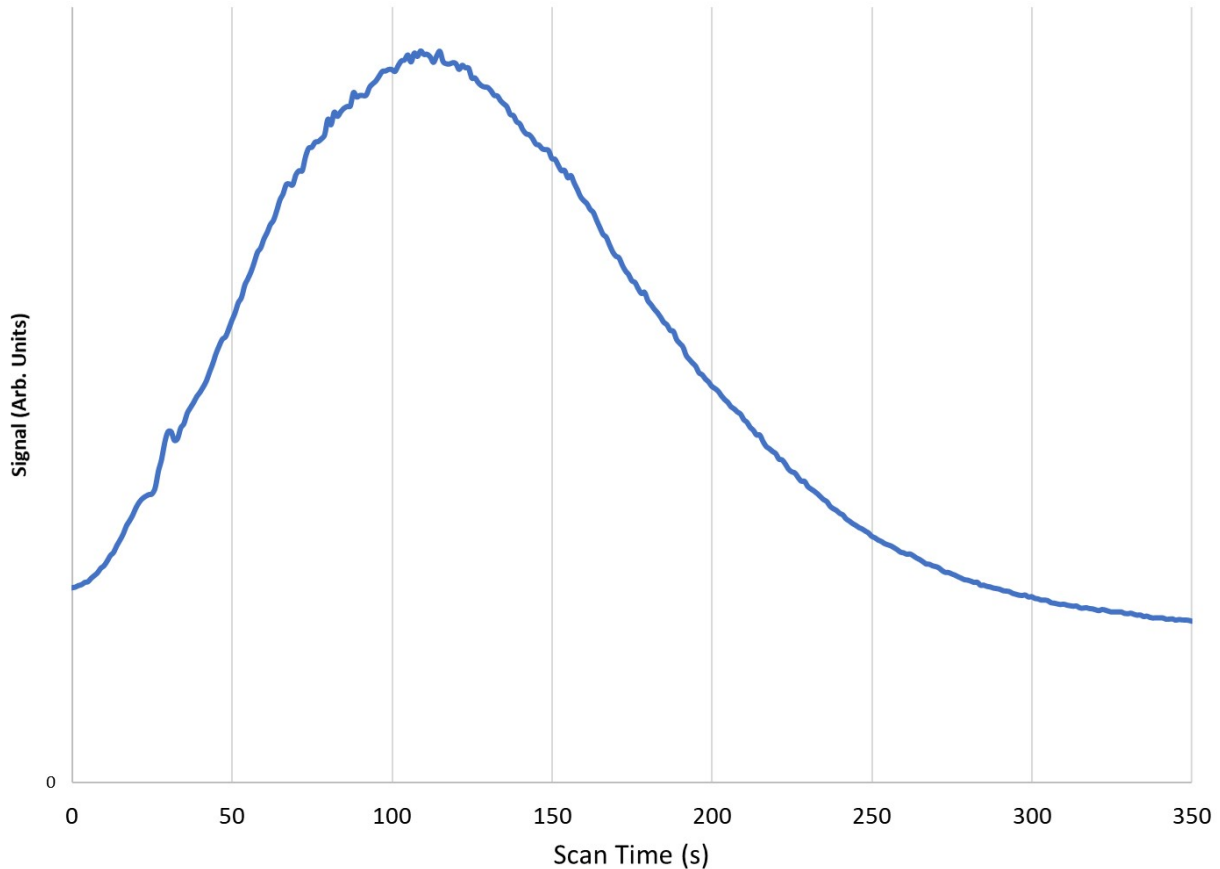


Figure 4.14: Initial Zeeman Slower Test: During our first scans with a single laser along two paths, we saw an artifact at ~ 30 s into the scan that we decided to investigate.

the correct or incorrect polarization, since there is no magnetic field to define an eigendirection for the polarization.

Now let us consider the interesting signals seen when the Zeeman slower is operated with the incorrect polarization. An atom initially in resonance with the Zeeman slower as it enters will scatter a photon and be Doppler shifted out of resonance. Because of the incorrect polarization, the Zeeman slower field now increases the detuning instead of compensating for the Doppler detuning. During its time in the Zeeman slower, this atom has seen much less scattering than in the case of the correct polarization. Thus the overall velocity change is reduced. As it enters the detection region, this atom is much closer to the laser resonance and has a much greater scattering rate, so we see a

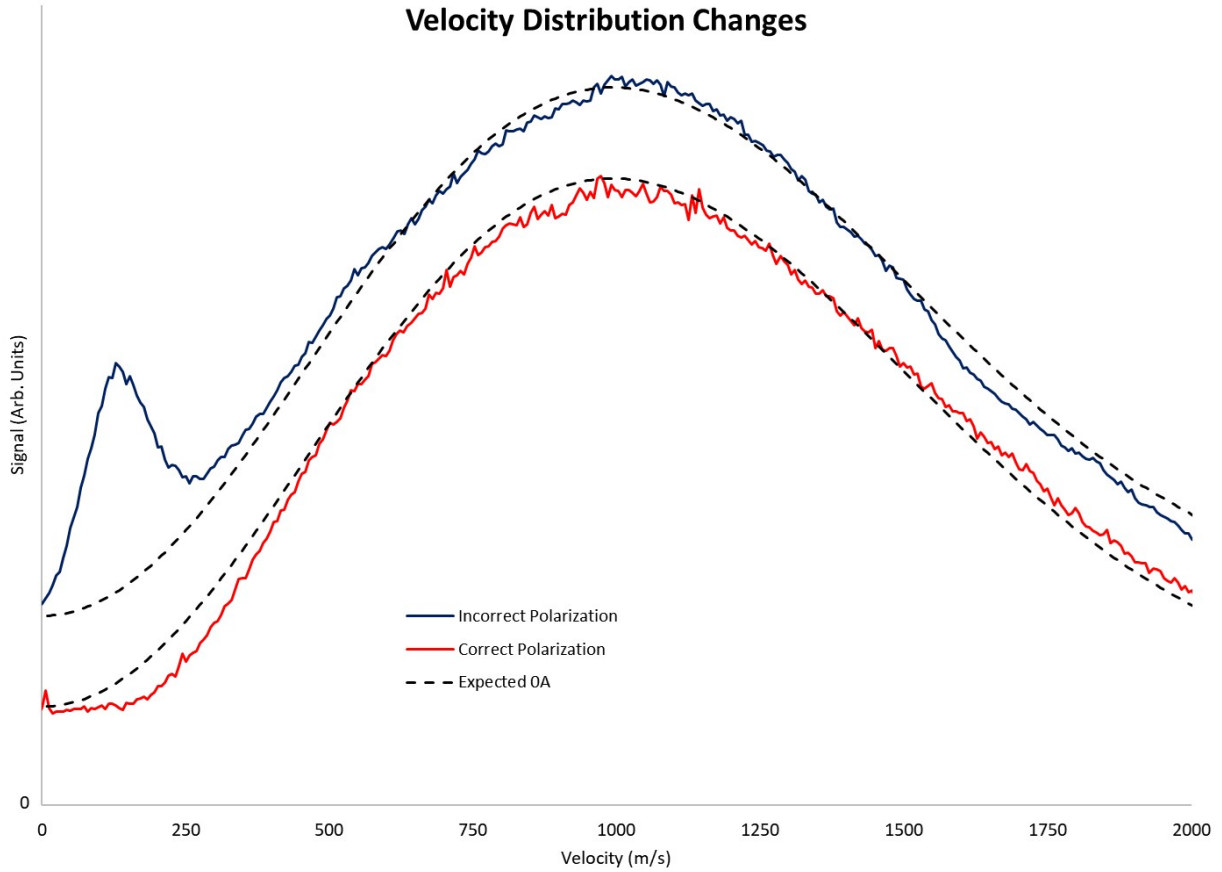


Figure 4.15: Interesting Zeeman Slower Spectra: The spectra are displaced in this plot for clarity. With the incorrect polarization, we see a large peak at the low velocity side of the scan; while with the correct polarization, we see a reduction of signal at the low velocity side of the scan. Both dashed curves are the same function with different offsets for easy comparison to the observed spectra. The correct polarization signal was scaled by 1.25 for easier comparison to the incorrect polarization.

greatly enhanced signal. But that begs the question, why then doesn't this happen uniformly across the entire velocity distribution?

In order to understand this we should reconsider the design characteristics that we imposed on the Zeeman slower. When we use the correct polarization the design called for operation at constant *acceleration*. When we derived the field needed for our Zeeman slower we started with the kinematic relation

$$v_f^2 - v_0^2 = 2az \tag{4.16}$$

Table 4.7: Expected velocity changes in the Zeeman slower running with 120A

v_0 , m/s	v_f , m/s	Δv , m/s
200	10	-190
250	150	-100
300	224	-76
400	347	-53
500	458	-42
750	723	-27
1000	980	-20
1300	1285	-15
1600	1587	-13
2000	1990	-10

The change in velocity is not conserved in the slower for different entrance velocities, v_0 . The atoms in the slower experience constant acceleration and so it is the change in squared velocities that is conserved. Extrapolating from our design to other velocity regimes is straightforward, some select values are shown in Table 4.7. As you can see, as our initial velocity gets higher and higher, the difference in entrance and exit velocities, Δv , gets smaller and smaller until the behavior is practically the same as when we had the current turned off. So as we probe larger and larger velocities in the distribution, it should relax to the zero amp velocity measurement. This agrees with what we see in Figure 4.15.

The more efficient the operation of the Zeeman slower with the correct polarization, less cooling will occur with the wrong polarization. The signal features seen in the incorrect polarization spectra are actually peaks where the slower is working to hold atoms farther from resonance as they pass through the slowing region. This means that they are slowed even less than when there is no field. The slower acts to keep the atoms off of resonance, so that when they reach the detection region they are nearer to the transition line center than they would be if the slower was working correctly. In normal operation, varying the Zeeman laser detuning will vary the exit velocity of atoms in the slower. If we had an independent probing laser set to resonate with atoms in trappable velocities, then varying the Zeeman slower detuning will allow us to optimize the signal for the

maximum number of trappable atoms in the detection region. Since the incorrect polarization has such a distinct feature at the low velocity end, we decided to investigate how this feature varies with different laser powers and different Zeeman slower currents.

4.6.2 Zeeman Slower Investigation with the Incorrect Polarization

The plots shown in the previous section are the only runs that we have with 130A of Zeeman slower current. Due to the tight winding of the slower coil, we had used $\frac{1}{8}$ " copper refrigerator tubing during construction as discussed in Section 3.3. This tubing has a tight rough inner diameter and it was difficult to keep water flow high enough to facilitate cooling the coil. The coil temperature began to run away at the end of these runs and in the future the maximum current that we used was 120A. With this output the coil could run continuously without any temperature problems.

Changing the current changes the observed feature. A summary plot is found in Figure 4.16. As the current is decreased, the peak moves to higher and higher velocity classes. The changes in the spectra as the laser power was varied were not as drastic as those seen in the current dependence, but they do show some interesting features. These features give us a testable response for our simulation work presented in the next section.

4.6.3 Zeeman Slower Simulations

In order to ensure that we understood the physics involved in the slowing process, and in order to show that cooling is taking place as expected, we simulated the Zeeman slower setup using Python. The simulation uses a kinematic approach to calculate the changes in atomic velocities as they travel down the slower. We initially discussed part of this simulation in the beginning of Section 2.4.2. A block diagram for the individual atomic trajectories simulation is shown in Figure 2.8.

We initially fix the laser detuning and pick a starting velocity class and set the position to be at the exit of the oven before it enters the slowing region. The local magnetic field strength is calculated based on the atomic position and current in the slower. Along with the velocity and set laser detuning, the total detuning experienced by the atom from the local environment is calculated.

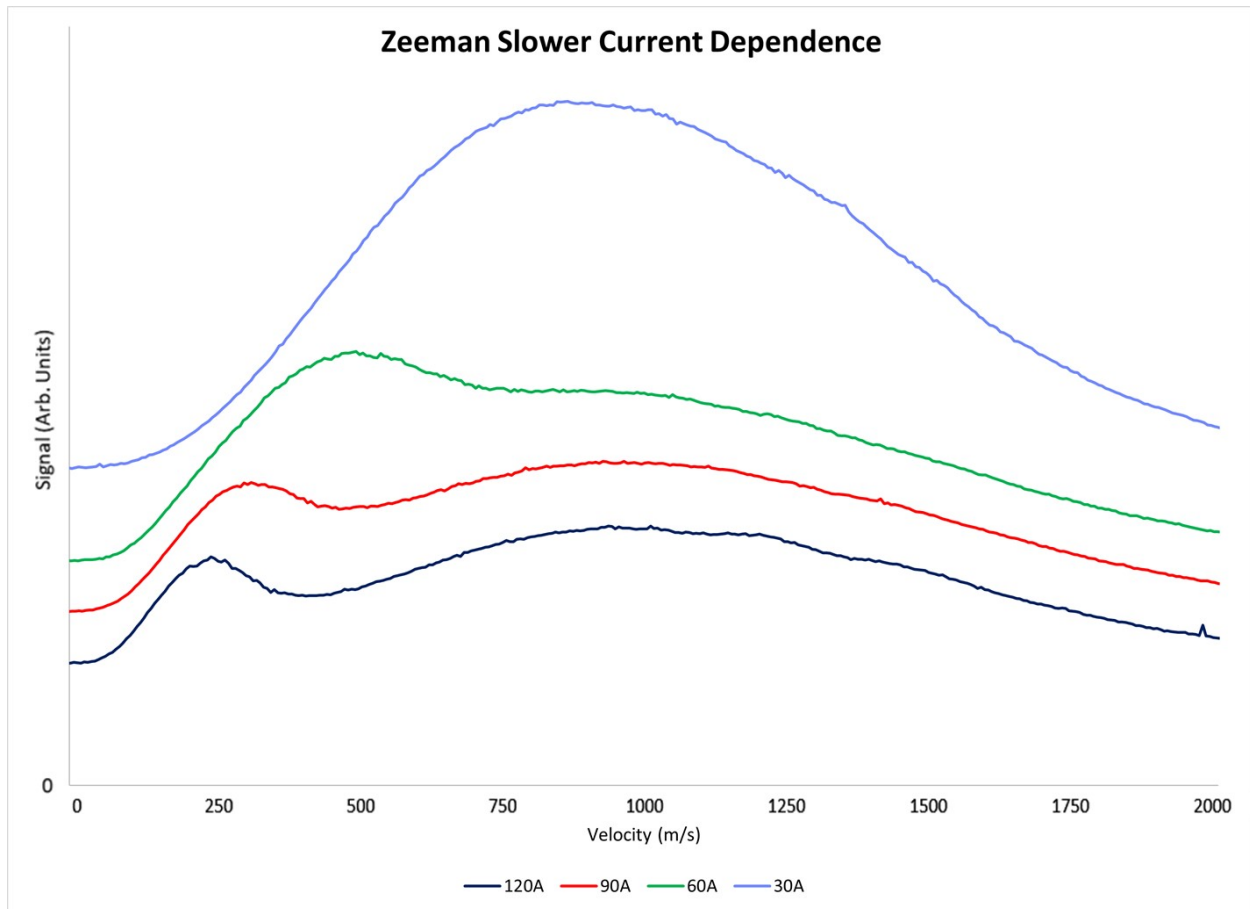


Figure 4.16: Experimental Zeeman Current Dependence: The spectra are displaced in this plot for clarity. As the current is decreased, we see a peaking feature moving to higher velocity classes in the spectra. These spectra were obtained using the incorrect polarization for the Zeeman slower design.

We use this to calculate our scattering rate and the photon momentum to find the scattering force and acceleration experienced by the atom. Using this acceleration, the new atomic position and velocity are calculated. If it has not reached the detection region, the position and velocity are used as new inputs to the algorithm. If the atom has reached the detection region the scattering rate is multiplied by the transit time and the number of atoms in the distribution at the starting velocity to generate the number of photons scattered in the detection region. This is directly proportional to the signal size as discussed in Section 3.5. This is only the signal generated from one velocity class and so we must iterate through velocities.

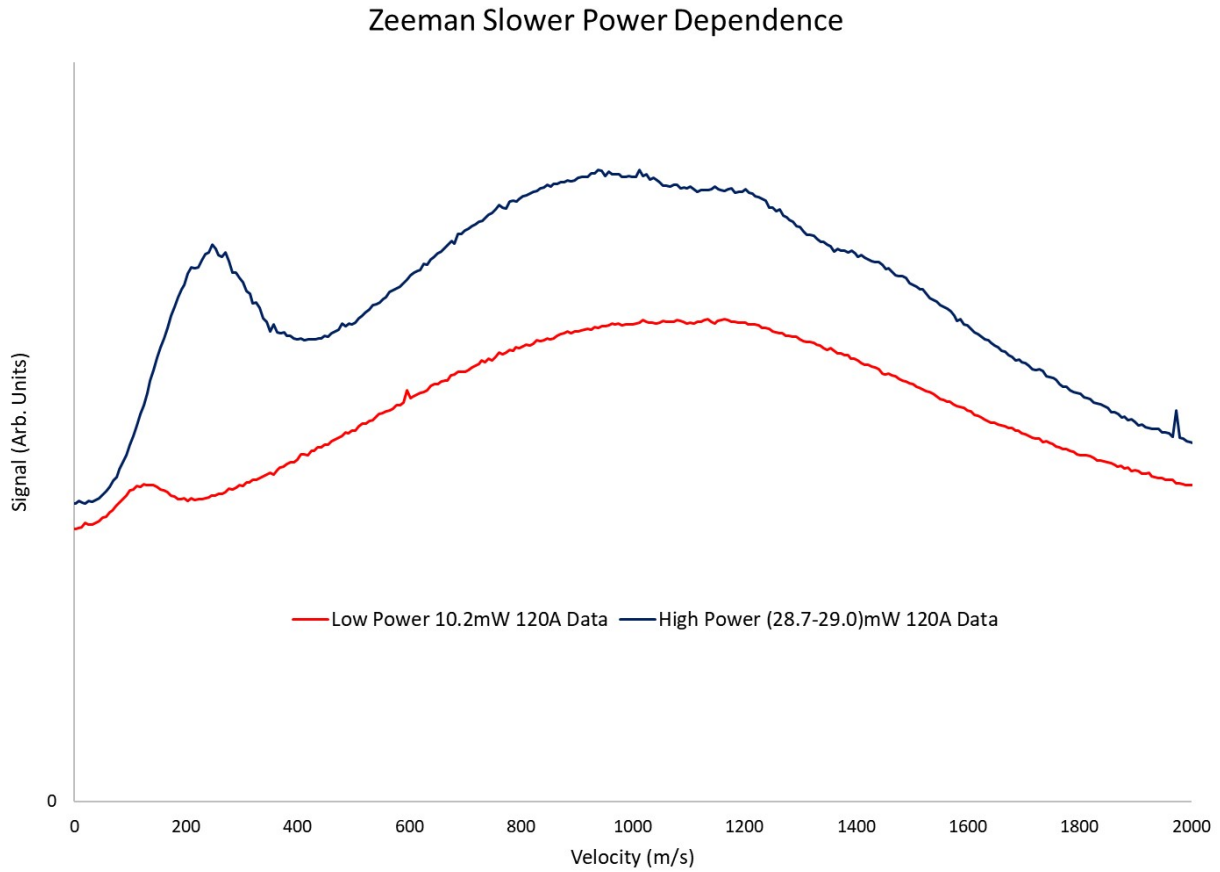


Figure 4.17: Experimental Zeeman Power Dependence: As the power is increased in the Zeeman slowing laser the slower addresses higher velocity atoms due to power broadening.

Simulations iterating through all velocities in the distribution takes a considerable amount of time, and the loop was limited to velocities that fall within $\pm 200\text{m/s}$ of the laser resonant frequency with no noticeable loss in fidelity due to negligible signals from atoms outside this range. A 30m/s simulation floor for the simulated velocity was also used due to the considerably long simulation time for slower atoms. This however also lead to difficulty in simulating low power runs effectively at 120A, but good agreement was found with low power runs for lower currents. The velocity step size in all of the simulations was 1m/s . Changing the velocity step size introduced very minor changes in the simulation.

This velocity iteration was then looped again through many detuning values. A time step of $2\mu\text{s}$ was typically used and maintained fidelity with time steps down to 100ns . Occasionally simulated

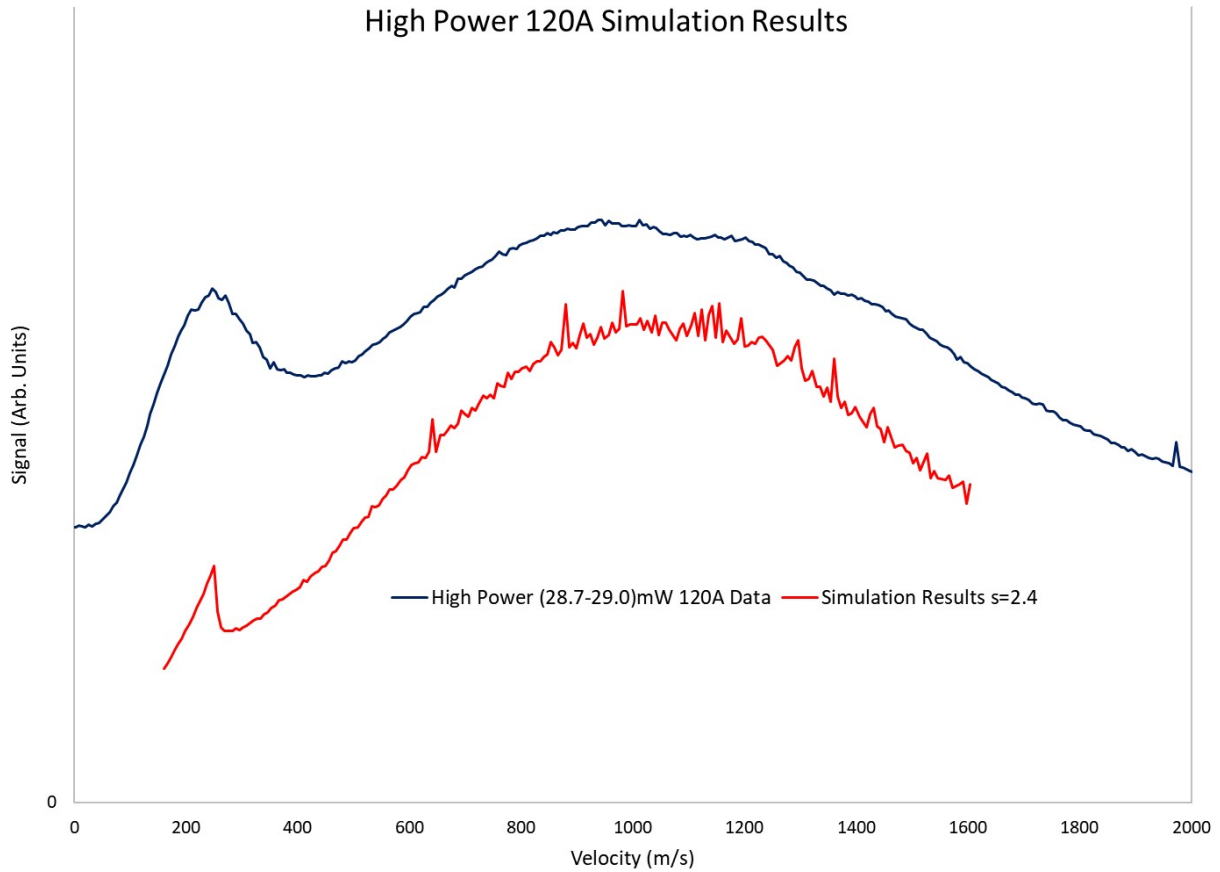


Figure 4.18: High Power 120A Zeeman Simulation Results

detunings would give signals that were much larger than neighboring points. When we changed the simulation time of those particular detunings, slightly varied the detuning value, or slightly varied the velocity stepping, these signals would relax to reasonable values in the spectra. Because of this, we attributed these points to artifacts and accidental resonances in the simulation and do not believe them to be physical. The 0A simulation was particularly problematic due to these outlier points. The onset of these resonances is more pronounced if the simulation is iterated through very fine detuning steps. The detuning steps that gave us the best simulated data corresponded to equivalent detuning steps as seen by the CCD during data runs, 4Γ per step ($\sim 29\text{MHz}$).

Figures 4.18, 4.19, 4.20, 4.21 show the results of some of our simulations. The figures all have the same absolute vertical scale, but are offset for clarity. Our simulation is able to recreate

High Power 90A Simulation Results

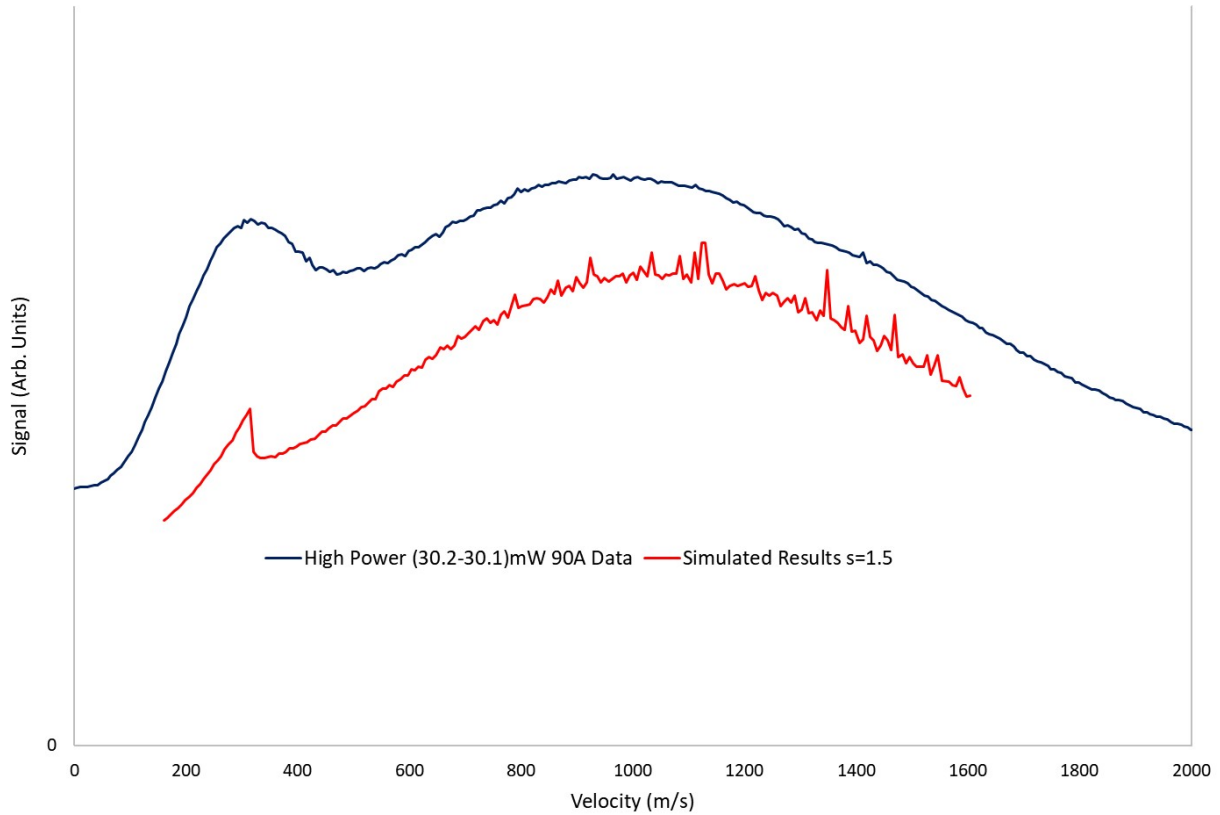


Figure 4.19: High Power 90A Zeeman Simulation Results

the qualitative features of the observed spectra. As we change the current and power, we can see that the peak positions in the simulation agree with our observed data. The extra broadening seen in the observed spectra can likely be attributed to many factors. Our simulation is only in the longitudinal direction and will not show any effects of transverse broadening as the beam is slowed along its path. The variable pitch coil design of the slower could give unexpected off axis fields, particularly near the zero crossing where the pitch spacing gets rather large. Our simulation also only accounts for a single magnetic sublevel and would not include any broadening effects from magnetic substate mixing as the states become degenerate at the magnetic field zero crossing in the slower. Simulation of these effects could be very interesting but are beyond the scope of this thesis.

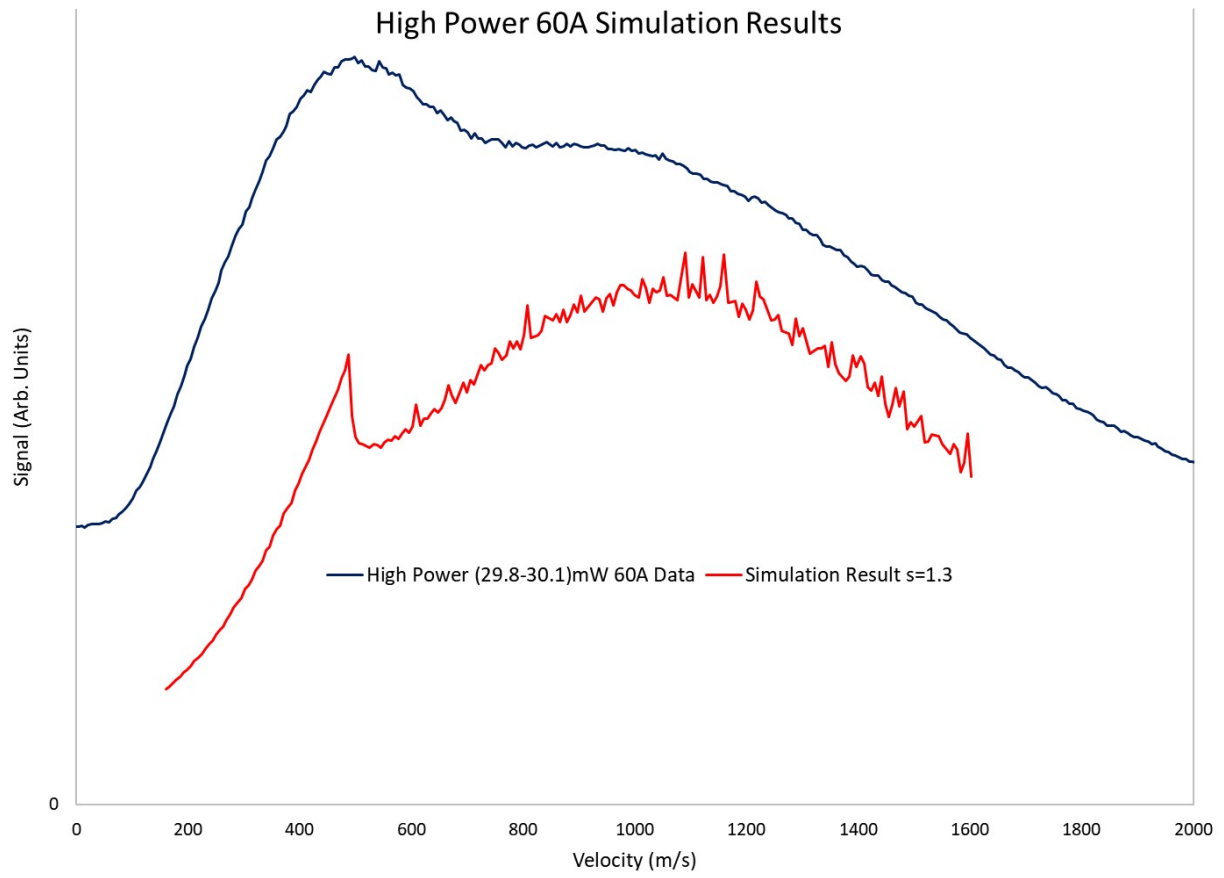


Figure 4.20: High Power 60A Zeeman Simulation Results

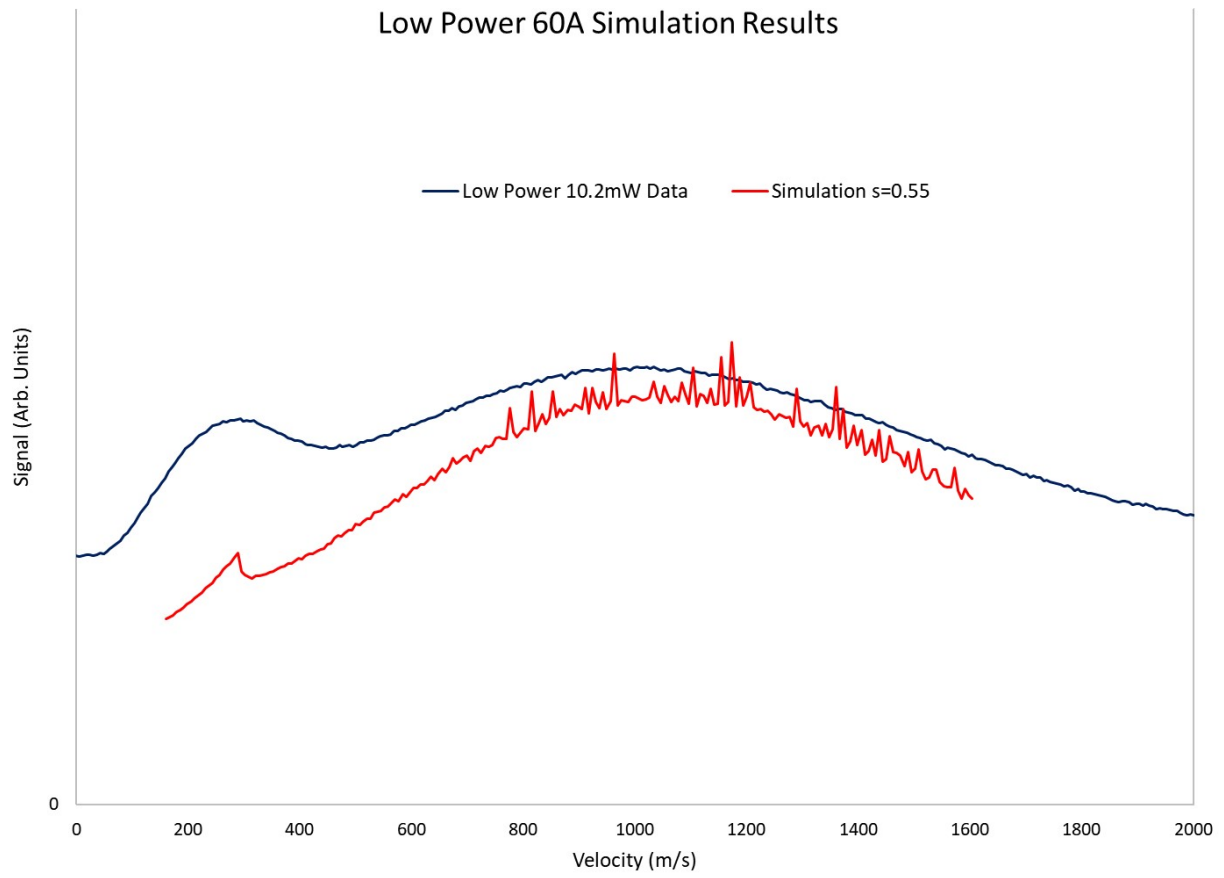


Figure 4.21: Low Power 60A Zeeman Simulation Results

Chapter 5

Conclusions

The laser cooling and magneto-optical trapping of silicon atoms were investigated experimentally. These are the first steps towards the development of a deterministic single ion source suitable for single ion implantation of a Kane quantum computer. We identified the $3s^23p^2\ ^3P_2 \rightarrow 3s3p^3\ ^3D_3^o$ transition at 221.74nm as a cycling transition suitable for laser cooling. We also identified the $3s^23p^2\ ^1D_2 \rightarrow 3s3p^3\ ^3D_3^o$ at 256.26nm as a repump transition coupling a lower metastable state with the upper cooling state. Two deep ultraviolet (DUV) laser systems were implemented to provide the cooling and repump laser light. Both systems utilized two stage second harmonic generation to quadruple the frequency of a fundamental laser to produce the DUV light. The cooling laser system utilized frequency quadrupling of a tunable cw Ti:Sapphire ring laser to produce up to 90 mW at 221.74nm. The repump laser system utilized frequency quadrupling of an external cavity diode laser to produce up to 35 mW at 256.26nm.

A silicon atomic beam source is not available commercially and is very challenging to use. A source operating at 1400°C was developed that produced a beam of free silicon atoms for laser studies. A robust crucible design was developed and implemented that was able to achieve more than 50 hours of run time. We have established operating procedures for the atomic oven. We have identified possible problems to be avoided when selecting materials for the oven crucible construction and established procedures for verification of the oven temperature. We have developed diagnostic tests to check these and other characteristics of the atomic beam in order to properly probe the health of the beam and establish good working conditions for experiments.

Careful spectroscopic studies were performed on the cooling and repump transitions. Frequency references for the UV lasers were investigated in Te_2 and $^{129}\text{I}_2$ with Doppler free saturated absorption spectroscopy, using the first doubling stage output of the cooling and repump laser, respectively. Specific hyperfine components of the molecular transitions in Te_2 and I_2 , suitable

for frequency references, were identified and measured. Locking of the cooling laser on the Te_2 reference was demonstrated.

The optical and magnetic systems for a magneto-optic trap (MOT) was implemented in the silicon atomic beam. A CCD optical system to image the fluorescence from atoms in the MOT was developed and achieved single photon detection capability. MOT trapping of silicon atoms was attempted under several detuning conditions while scanning through the repump transition frequency uncertainty. When a trap signal was not observed we extended our frequency range to $\pm 1.9\text{GHz}$ from the expected repump transition. A Zeeman slower, based on a novel design utilizing a variable pitch helical solenoid, was designed, simulated, and constructed to improve the flux of slow atoms.

Investigations were performed for one dimensional laser cooling, via a Zeeman slower, along the atomic beam motion direction. Atomic beam velocity distribution profiles were observed to be modified when the Zeeman slower was on. The parameter space of Zeeman slower currents, laser power and detuning, was explored. A simulation of the atom motion over the 1m long flight path under the influence of the Zeeman slower with an incorrect polarization laser was carried out and found to agree qualitatively well with the observed results.

For future work, a separate laser system with sufficient power would be able to cool atoms traveling down the Zeeman slower. We have simulated the amount of power needed to establish a MOT and these simulations show that we have sufficient laser power to drive velocity changing transitions and form a MOT with our current experimental setup.

There is potential for a simulation project for modeling the Zeeman slower in three spatial dimensions. The Zeeman slower process is used in a wide array of cold atom experiments to enhance MOT trap populations, however the finer details of its operation are not well understood. Losses due to diffusion in the Zeeman slower could account for the reduction of expected trap signal from calculated atomic population increases. The off axis magnetic fields of the variable pitch helical coil Zeeman slower was not considered in the current thesis. It may be interesting to simulate off-axis effects when reversing the current direction in the coils.

The investigations in this thesis lay the groundwork for development of a deterministic single atom MOT source. This provides the potential for a deterministic single ion source to be used in building a Kane Quantum Computer.

Bibliography

- [1] R. P. Feynman, “Simulating physics with computers,” *International Journal of Theoretical Physics*, vol. 21, pp. 467–488, Jun 1982.
- [2] Wikipedia, “Toffoli gate — Wikipedia, the free encyclopedia.” <http://en.wikipedia.org/w/index.php?title=Toffoli%20gate&oldid=1073642477>, 2022. [Online; accessed 28-April-2022].
- [3] Wikipedia, “Quantum logic gate — Wikipedia, the free encyclopedia.” <http://en.wikipedia.org/w/index.php?title=Quantum%20logic%20gate&oldid=1082838670>, 2022. [Online; accessed 28-April-2022].
- [4] P. Shor, “Algorithms for quantum computation: discrete logarithms and factoring,” in *Proceedings 35th Annual Symposium on Foundations of Computer Science*, pp. 124–134, 1994.
- [5] L. K. Grover, “Quantum mechanics helps in searching for a needle in a haystack,” *Phys. Rev. Lett.*, vol. 79, pp. 325–328, Jul 1997.
- [6] F. Arute *et al.*, “Quantum supremacy using a programmable superconducting processor,” *Nature*, vol. 574, pp. 505–510, Oct 2019.
- [7] E. Pednault, J. Gunnels, D. Maslov, and J. Gambetta, “On "quantum supremacy".” <https://www.ibm.com/blogs/research/2019/10/on-quantum-supremacy/>, Aug 2020.
- [8] P. J. J. O’Malley *et al.*, “Scalable quantum simulation of molecular energies,” *Phys. Rev. X*, vol. 6, p. 031007, Jul 2016.
- [9] C. Hempel, C. Maier, J. Romero, J. McClean, T. Monz, H. Shen, P. Jurcevic, B. P. Lanyon, P. Love, R. Babbush, A. Aspuru-Guzik, R. Blatt, and C. F. Roos, “Quantum chemistry calculations on a trapped-ion quantum simulator,” *Phys. Rev. X*, vol. 8, p. 031022, Jul 2018.

- [10] F. Arute *et al.*, “Hartree-fock on a superconducting qubit quantum computer,” *Science*, vol. 369, no. 6507, pp. 1084–1089, 2020.
- [11] C. Monroe, W. C. Campbell, L.-M. Duan, Z.-X. Gong, A. V. Gorshkov, P. W. Hess, R. Islam, K. Kim, N. M. Linke, G. Pagano, P. Richerme, C. Senko, and N. Y. Yao, “Programmable quantum simulations of spin systems with trapped ions,” *Rev. Mod. Phys.*, vol. 93, p. 025001, Apr 2021.
- [12] E. Knill, R. Laflamme, and G. J. Milburn, “A scheme for efficient quantum computation with linear optics,” *Nature*, vol. 409, pp. 46–52, Jan. 2001.
- [13] M. A. Eriksson *et al.*, “Spin-based quantum dot quantum computing in silicon,” *Quantum Information Processing*, vol. 3, pp. 133–146, Oct 2004.
- [14] Z. Zhang, G. Chen, Z. Diao, and P. R. Hemmer, *NMR Quantum Computing*, pp. 465–520. Boston, MA: Springer US, 2009.
- [15] G. Wendin, “Quantum information processing with superconducting circuits: a review,” *Reports on Progress in Physics*, vol. 80, p. 106001, sep 2017.
- [16] S. Kotler, G. A. Peterson, E. Shojaei, F. Lecocq, K. Cicak, A. Kwiatkowski, S. Geller, S. Glancy, E. Knill, R. W. Simmonds, J. Aumentado, and J. D. Teufel, “Direct observation of deterministic macroscopic entanglement,” *Science*, vol. 372, no. 6542, pp. 622–625, 2021.
- [17] B. E. Kane, “A silicon-based nuclear spin quantum computer,” *Nature*, vol. 393, pp. 133–137, May 1998.
- [18] B. Kane, “Silicon-based quantum computation,” *Fortschritte der Physik*, vol. 48, p. 1023–1041, Sep 2000.
- [19] D. N. Jamieson, C. Yang, T. Hopf, S. M. Hearne, C. I. Pakes, S. Praver, M. Mitic, E. Gauja, S. E. Andresen, F. E. Hudson, A. S. Dzurak, and R. G. Clark, “Controlled shallow single-

- ion implantation in silicon using an active substrate for sub-20-keV ions,” *Applied Physics Letters*, vol. 86, no. 20, p. 202101, 2005.
- [20] M. T. Mądzik *et al.*, “Precision tomography of a three-qubit donor quantum processor in silicon,” *Nature*, vol. 601, pp. 348–353, Jan 2022.
- [21] M. Fuechsle, J. A. Miwa, S. Mahapatra, H. Ryu, S. Lee, O. Warschkow, L. C. L. Hollenberg, G. Klimeck, and M. Y. Simmons, “A single-atom transistor,” *Nature Nanotechnology*, vol. 7, pp. 242–246, Apr 2012.
- [22] Y. He, S. K. Gorman, D. Keith, L. Kranz, J. G. Keizer, and M. Y. Simmons, “A two-qubit gate between phosphorus donor electrons in silicon,” *Nature*, vol. 571, pp. 371–375, Jul 2019.
- [23] L. Fricke, S. J. Hile, L. Kranz, Y. Chung, Y. He, P. Pakkiam, M. G. House, J. G. Keizer, and M. Y. Simmons, “Coherent control of a donor-molecule electron spin qubit in silicon,” *Nature Communications*, vol. 12, p. 3323, Jun 2021.
- [24] J. L. Hanssen, J. J. McClelland, E. A. Dakin, and M. Jacka, “Laser-cooled atoms as a focused ion-beam source,” *Phys. Rev. A*, vol. 74, p. 063416, Dec 2006.
- [25] H. Wollnik, *Optics of charged particles*. Academic Press, 1987.
- [26] R. E. Scholten, R. Gupta, J. J. McClelland, R. J. Celotta, M. S. Levenson, and M. G. Vangel, “Laser collimation of a chromium beam,” *Physical Review A - Atomic, Molecular, and Optical Physics*, vol. 55, no. 2, pp. 1331–1338, 1997.
- [27] S. B. Hill and J. J. McClelland, “Atoms on demand: Fast, deterministic production of single Cr atoms,” *Applied Physics Letters*, vol. 82, no. 18, pp. 3128–3130, 2003.
- [28] S. A. Lee and W. M. Fairbank Jr., “Measurement of the hyperfine structure and isotope shifts of the $3s^23p^2\ 3P_2 \rightarrow 3s^3p^3\ 3D_3^o$ transition in silicon,” *Physical Review A - Atomic, Molecular, and Optical Physics*, vol. 82, no. 4, 2010.

- [29] W. Czajkowski, J. Kluck, S. A. Lee, and W. M. Fairbank Jr., “Near threshold resonance ionization of Si using laser two photon excitation,” *to be published*.
- [30] A. Kramida, Yu. Ralchenko, J. Reader, and NIST ASD Team. NIST Atomic Spectra Database (ver. 5.6.1), [Online]. Available: <https://physics.nist.gov/asd> [2019, May 14]. National Institute of Standards and Technology, Gaithersburg, MD., 2018.
- [31] W. C. Martin and R. Zalubas, “Energy levels of silicon, si i through si xiv,” *Journal of Physical and Chemical Reference Data*, vol. 12, no. 2, pp. 323–380, 1983.
- [32] T. R. O’Brian and J. E. Lawler, “Radiative lifetimes in si i from laser-induced fluorescence in the visible, ultraviolet, and vacuum ultraviolet,” *Phys. Rev. A*, vol. 44, pp. 7134–7143, Dec 1991.
- [33] C. Froese Fischer, “The mchf/mcdhf collection (ab initio mchf calculations).” <http://nlte.nist.gov/MCHF/>.
- [34] D. E. Kelleher and L. I. Podobedova, “Atomic transition probabilities of silicon. a critical compilation,” *Journal of Physical and Chemical Reference Data*, vol. 37, no. 3, pp. 1285–1501, 2008.
- [35] H. Metcalf and P. van der Straten, “Cooling and trapping of neutral atoms,” *Physics Reports*, vol. 244, no. 4, pp. 203–286, 1994.
- [36] W. D. Phillips and H. Metcalf, “Laser deceleration of an atomic beam,” *Phys. Rev. Lett.*, vol. 48, pp. 596–599, Mar 1982.
- [37] P. D. Lett, W. D. Phillips, S. L. Rolston, C. E. Tanner, R. N. Watts, and C. I. Westbrook, “Optical molasses,” *J. Opt. Soc. Am. B*, vol. 6, pp. 2084–2107, Nov 1989.
- [38] E. L. Raab, M. Prentiss, A. Cable, S. Chu, and D. E. Pritchard, “Trapping of neutral sodium atoms with radiation pressure,” *Phys. Rev. Lett.*, vol. 59, pp. 2631–2634, Dec 1987.

- [39] J. T. Verdeyen, *Laser Electronics*. Prentice Hall series in solid state physical electronics, Prentice Hall, 1995.
- [40] M. H. Shah, H. A. Camp, M. L. Trachy, G. Veshapidze, M. A. Gearba, and B. D. DePaola, “Model-independent measurement of the excited fraction in a magneto-optical trap,” *Phys. Rev. A*, vol. 75, p. 053418, May 2007.
- [41] N. Ramsey, *Molecular Beams*. Oxford: Clarendon Press, 1956.
- [42] S. C. Bell, M. Junker, M. Jasperse, L. D. Turner, Y.-J. Lin, I. B. Spielman, and R. E. Scholten, “A slow atom source using a collimated effusive oven and a single-layer variable pitch coil zeeman slower,” *Review of Scientific Instruments*, vol. 81, no. 1, p. 013105, 2010.
- [43] D. N. V.G. Dmitriev, G.G Gurzadyan, *Handbook of Nonlinear Optical Crystals*. Berlin: Springer, second ed., 1997.
- [44] E. Hecht, *Optics*. San Francisco, CA: Addison-Wesley, 4th ed., 2002.
- [45] J. E. Midwinter and J. Warner, “The effects of phase matching method and of uniaxial crystal symmetry on the polar distribution of second-order non-linear optical polarization,” *British Journal of Applied Physics*, vol. 16, no. 8, pp. 1135–1142, 1965.
- [46] G. D. Boyd and D. A. Kleinman, “Parametric interaction of focused Gaussian light beams,” *Journal of Applied Physics*, vol. 39, no. 8, pp. 3597–3639, 1968.
- [47] R. W. McGowan, *Light force cooling, manipulation, and nanometer-scale deposition of neutral aluminum atoms*. PhD thesis, Colorado State University, 1996.
- [48] M. Schmid, “Vapor pressure calculator.” https://www.iap.tuwien.ac.at/www/surface/vapor_pressure, Dec 2018.
- [49] T. W. Hänsch, I. S. Shahin, and A. L. Schawlow, “High-resolution saturation spectroscopy of the sodium *d* lines with a pulsed tunable dye laser,” *Phys. Rev. Lett.*, vol. 27, pp. 707–710, Sep 1971.

- [50] J. L. Hall and S. A. Lee, "Interferometric real-time display of cw dye laser wavelength with sub-Doppler accuracy," *Applied Physics Letters*, vol. 29, no. 6, pp. 367–369, 1976.
- [51] T. W. Hänsch, I. S. Shahin, and A. L. Schawlow, "High-resolution saturation spectroscopy of the sodium D lines with a pulsed tunable dye laser," *Phys. Rev. Lett.*, vol. 27, pp. 707–710, Sep 1971.
- [52] L. Hlousek and W. M. Fairbank, "High-accuracy wave-number measurements in molecular iodine," *Opt. Lett.*, vol. 8, pp. 322–323, Jun 1983.
- [53] L. J. Radziemski, K. L. Andrew, V. Kaufman, and U. Litzén, "Vacuum ultraviolet wavelength standards and improved energy levels in the first spectrum of silicon*," *J. Opt. Soc. Am.*, vol. 57, pp. 336–340, Mar 1967.
- [54] L. J. Radziemski and K. L. Andrew, "Arc spectrum of silicon*," *J. Opt. Soc. Am.*, vol. 55, pp. 474–491, May 1965.
- [55] S. Gerstenkorn and P. Luc, *Atlas du spectre d'absorption de la molécule d'iode, 14800-20000 cm-1 / S. Gerstenkorn et P. Luc*. Centre national de la recherche scientifique Paris, 1978.
- [56] Gerstenkorn, S., Luc, P., and Sinzelle, J., "Study of the iodine absorption spectrum by means of fourier spectroscopy in the region 12 600-14 000 cm-1," *J. Phys. France*, vol. 41, no. 12, pp. 1419–1430, 1980.
- [57] S. Gerstenkorn, P. Luc, and R. J. L. Roy, "Molecular constants describing the transitions of 127,129i2 and 129,129i2," *Canadian Journal of Physics*, vol. 69, no. 10, pp. 1299–1303, 1991.
- [58] J. M. Hutson, S. Gerstenkorn, P. Luc, and J. Sinzelle, "Use of calculated centrifugal distortion constants (D_ν , H_ν , L_ν and M_ν) in the analysis of the $B \leftarrow X$ system of I_2 ," *Journal of Molecular Spectroscopy*, vol. 96, no. 2, pp. 266 – 278, 1982.

- [59] A. M. Steane, M. Chowdhury, and C. J. Foot, “Radiation force in the magneto-optical trap,” *Journal of the Optical Society of America B*, vol. 9, no. 12, p. 2142, 1992.
- [60] U. D. Rapol, A. Wasan, and V. Natarajan, “Loading of a Rb magneto-optic trap from a getter source,” *Phys. Rev. A*, vol. 64, p. 023402, Jun 2001.
- [61] S. Chu, “Nobel lecture: The manipulation of neutral particles,” *Rev. Mod. Phys.*, vol. 70, pp. 685–706, Jul 1998.

Appendix A

Zeeman Slower Field Matching Maple Code

```

> restart;
> # Ideal Field in Tesla
Bideal:=B0+Ba*sqrt(1-z/z0);

```

$$Bideal := B0 + Ba \sqrt{1 - \frac{z}{z0}} \quad (1)$$

```

> B0:=h*delta/(mu);
Ba:=h*v0/(lambda*mu);
z0:=v0^2/(vr*Gamma*eta);
L:=0.27;

```

$$B0 := \frac{h \delta}{\mu}$$

$$Ba := \frac{h v0}{\lambda \mu}$$

$$z0 := \frac{v0^2}{vr \Gamma \eta}$$

$$L := 0.27 \quad (2)$$

```

> Bideal;
vr:=h/(m*lambda);
eta:=(s0/(1+s0))*etal;
s0:=0.1;
h:=6.626E-34;
Gamma:=4.54E7;
ub:=9.274E-24;
mu:=ub;
lambda:=221.74E-9;
m:=28*1.6726E-27;
#etal:=0.5;
#v0:=sqrt(L*vr*Gamma*eta);
v0:=198.89657614667;
etal:=solve(z0=L,etal);
u0:=4e-7*evalf(Pi);
Bideal;

```

$$\frac{h \delta}{\mu} + \frac{h v0 \sqrt{1 - \frac{z vr \Gamma \eta}{v0^2}}}{\lambda \mu}$$

$$vr := \frac{h}{m \lambda}$$

$$\eta := \frac{s0 \eta l}{1 + s0}$$

$$s0 := 0.1$$

$$h := 6.626 \cdot 10^{-34}$$

$$\Gamma := 4.54 \cdot 10^7$$

$$ub := 9.274 \cdot 10^{-24}$$

$$\mu := 9.274 \cdot 10^{-24}$$

```

λ := 2.2174 10-7
m := 4.68328 10-26
v0 := 198.89657614667
ηl := 0.5563786004
u0 := 0.000001256637062

```

$$7.144705629 \cdot 10^{-11} \delta + 0.06408665494 \sqrt{1 - 3.703703702 z} \quad (3)$$

```

> #set detuning so that the field profile is 1/3 positive
delta := solve(1/2*subs([delta=0, z=0], Bideal) = subs(z=0, Bideal),
delta);
Bideal;

```

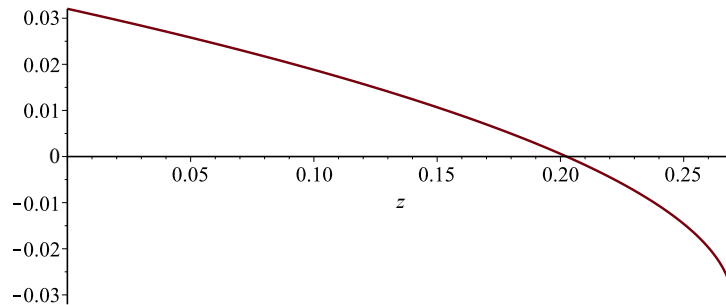
$$\delta := -4.484905206 \cdot 10^8$$

$$-0.03204332746 + 0.06408665494 \sqrt{1 - 3.703703702 z} \quad (4)$$

```

> plot(Bideal, z=0..L);

```

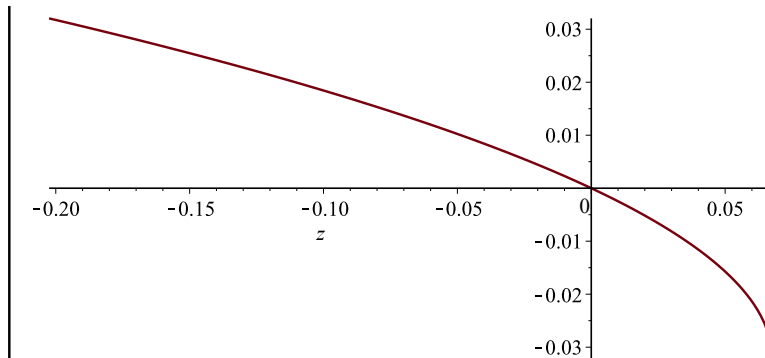


```

> #reset z for zero crossing at z=0
zerocross := solve(Bideal=0, z);
Bideal := subs(z=z+zerocross, Bideal);
plot(Bideal, z=-zerocross..L-zerocross);
zerocross := 0.2025000001

```

$$Bideal := -0.03204332746 + 0.06408665494 \sqrt{0.2500000000 - 3.703703702 z}$$



```

> with(plots):with(LinearAlgebra):
pos_start:=-0.01:
pos_stop:=-0.015:
neg_start:=0.02:
neg_stop:=0.04:
> assume(a,'real',b,'real',c,'real',d,'real',e,'real',f,'real',g,
'real',j,'real',R,'real',p,'real',zp,'real',R>0):
> theta1:=a*p+b*p^2+c*p^3+d*p^4:
theta2:=e*p+f*p^2+g*p^3+j*p^4:
> x1:=R*cos(theta1):
x2:=R*cos(theta2):
> y1:=R*sin(theta1):
y2:=R*sin(theta2):
> z1:=p:
z2:=p:
> rpvec1:=<0|0|zp>-<x1|y1|z1>:
rpvec2:=<0|0|zp>-<x2|y2|z2>:
> dr1:=map(diff,rpvec1,p):
dr2:=map(diff,rpvec2,p):
> rp1:=norm(rpvec1,2):
rp2:=norm(rpvec2,2):
> rp1:=simplify(rp1):
rp2:=simplify(rp2):
> Bdir1:=CrossProduct(dr1,rpvec1):
Bdir2:=CrossProduct(dr2,rpvec2):
> Bdir1:=map(simplify,Bdir1):
Bdir2:=map(simplify,Bdir2):
u0:=Pi*4E-07:
> Bz_pos:=u0*Cur/(4*evalf(Pi))*int(Bdir1[3]/rp1^3,p=pos_start-
zerocross..pos_stop):
Bz_neg:=u0*Cur/(4*evalf(Pi))*int(Bdir2[3]/rp2^3,p=neg_start+0..I-
zerocross+neg_stop):
> Bfit_pos:=subs(R=0.081*2.54/200+1.5*2.54/200,Bz_pos):
Bfit_neg:=subs(R=0.081*2.54/200+1.5*2.54/200,Bz_neg):
> atemp:=-120;
btemp:=2950;

```

```

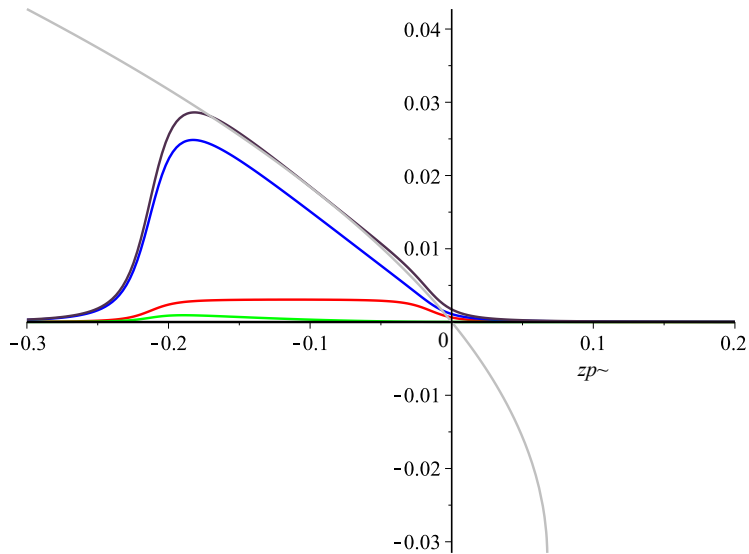
ctemp:=-400;
dtemp:=000;
Curtemp1:=130;
plot([subs([a=atemp,b=00,c=00,d=00,Cur=Curtemp1],Bfit_pos),subs(
[a=00,b=btemp,c=00,d=00,Cur=Curtemp1],Bfit_pos),subs([a=00,b=00,
c=ctemp,d=00,Cur=Curtemp1],Bfit_pos),subs([a=00,b=00,c=00,d=
dtemp,Cur=Curtemp1],Bfit_pos),subs([a=atemp,b=btemp,c=ctemp,d=
dtemp,Cur=Curtemp1],Bfit_pos),subs(z=zp,Bideal)],zp=-0.3..0.2,
color=[red,blue,green,black,violet,gray]);
plot(subs([a=atemp,b=btemp,c=ctemp,d=dtemp,Cur=Curtemp1],
Bfit_pos)-subs(z=zp,Bideal),zp=-zerocross..0,-0.00036..0.00036);
#####
# a = red
# b = blue
# c = green
# d = black

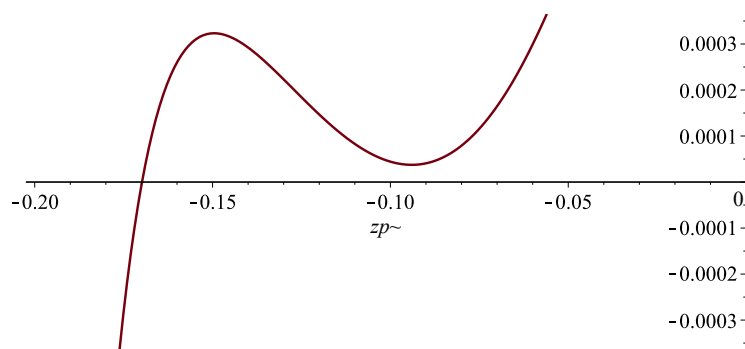
```

```

atemp := -120
btemp := 2950
ctemp := -400
dtemp := 0
Curtemp1 := 130

```





```

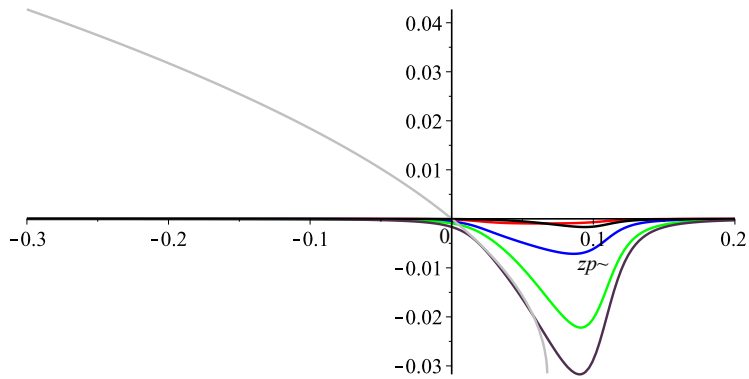
> etemp:=40;
  ftemp:=2000;
  gtemp:=48000;
  jtemp:=30000;
  Curtemp2:=130;
  plot([subs([e=etemp,f=00,g=00,j=00,Cur=Curtemp2],Bfit_neg),subs(
[e=00,f=ftemp,g=00,j=00,Cur=Curtemp2],Bfit_neg),subs([e=00,f=00,
g=gtemp,j=00,Cur=Curtemp2],Bfit_neg),subs([e=00,f=00,g=00,j=
jtemp,Cur=Curtemp2],Bfit_neg),subs([e=etemp,f=ftemp,g=gtemp,j=
jtemp,Cur=Curtemp2],Bfit_neg),subs(z=zp,Bideal)],zp=-0.3..0.2,
color=[red,blue,green,black,violet,gray]);
#####
# e = red
# f = blue
# g = green
# j = black

```

```

    etemp:=40
    ftemp:=2000
    gtemp:=48000
    jtemp:=30000
    Curtemp2:=130

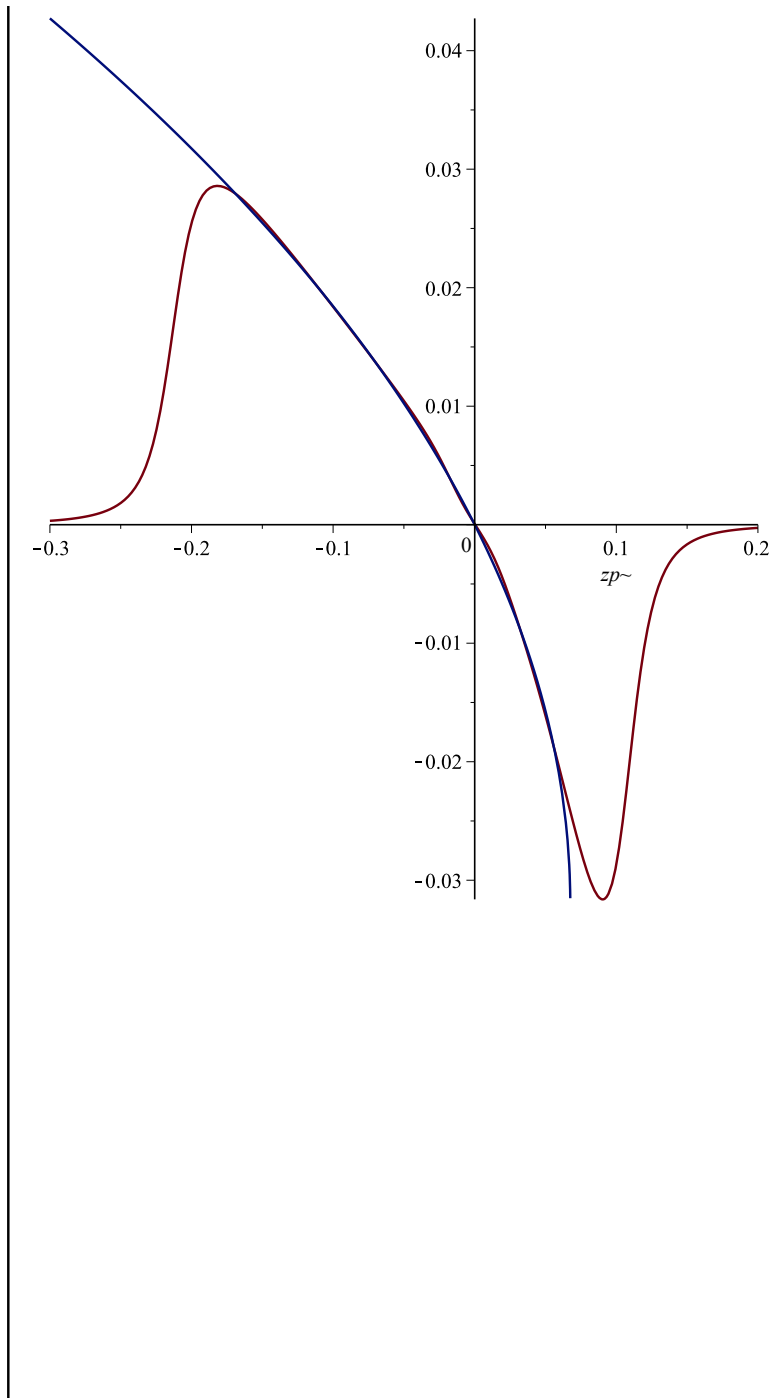
```

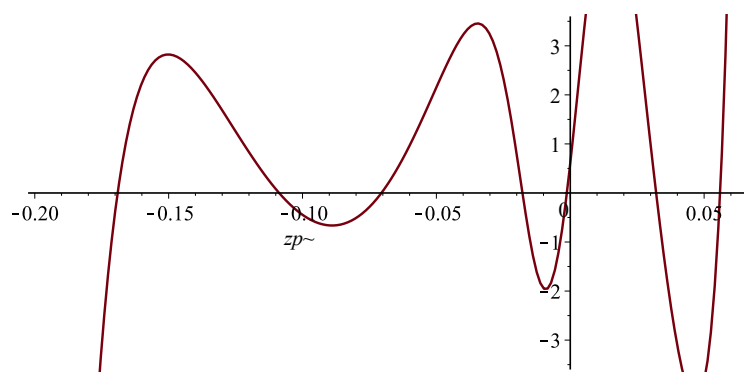


```

> plot([subs([e=etemp,f=ftemp,g=gtemp,j=jtemp,Cur=Curtemp2],
Bfit_neg)+subs([a=atemp,b=btemp,c=ctemp,d=dtemp,Cur=Curtemp1],
Bfit_pos),subs(z=zp,Bideal)],zp=-0.3..0.2);
# Following in Gauss, if the field is off by 3.6G then the
scattering rate decreases by 5%
plot(10000*[subs([e=etemp,f=ftemp,g=gtemp,j=jtemp,Cur=Curtemp2],
Bfit_neg)+subs([a=atemp,b=btemp,c=ctemp,d=dtemp,Cur=Curtemp1],
Bfit_pos)-subs(z=zp,Bideal)],zp=-zerocross..L-zerocross,-3.6.
.3.6);

```

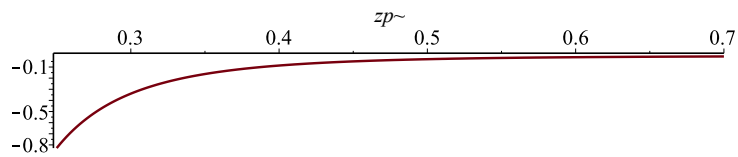
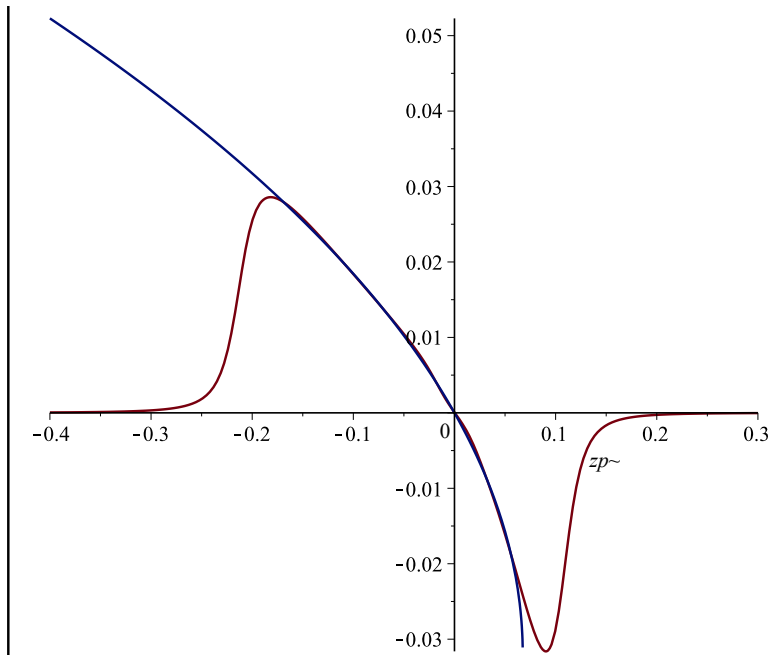




```

> plot([subs([e=etemp,f=ftemp,g=gtemp,j=jtemp,Cur=Curtemp2],
Bfit_neg)+subs([a=atemp,b=btemp,c=ctemp,d=dtemp,Cur=Curtemp1],
Bfit_pos),subs(z=zp,Bideal)],zp=-0.4..0.3);
plot(10000*[subs([e=etemp,f=ftemp,g=gtemp,j=jtemp,Cur=Curtemp2],
Bfit_neg)+subs([a=atemp,b=btemp,c=ctemp,d=dtemp,Cur=Curtemp1],
Bfit_pos)],zp=0.25..0.7);

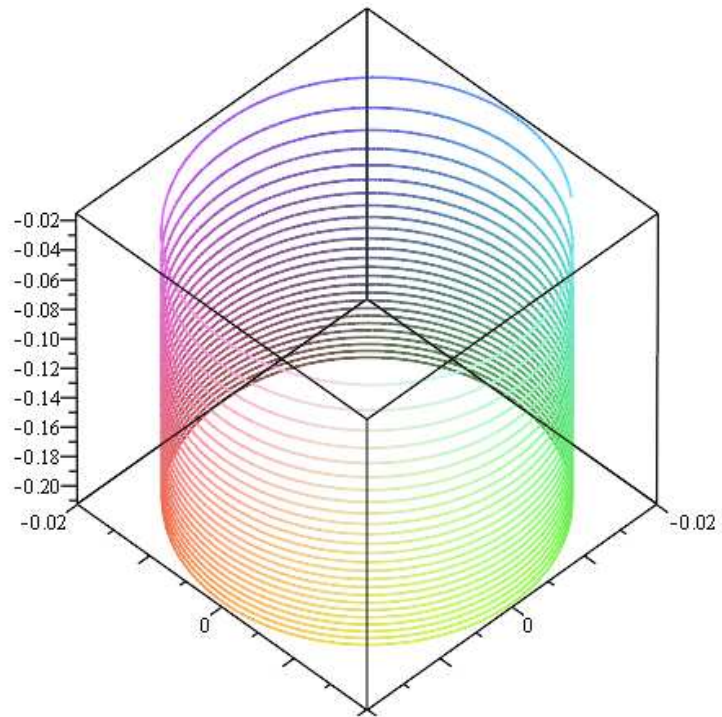
```



```

> xtemp1:=subs([a=atemp,b=btemp,c=ctemp,d=dtemp,R=0.081*
2.54/200+1.5*2.54/200],x1):
> ytemp1:=subs([a=atemp,b=btemp,c=ctemp,d=dtemp,R=0.081*
2.54/200+1.5*2.54/200],y1):
> ztemp1:=subs([a=atemp,b=btemp,c=ctemp,d=dtemp,R=0.081*
2.54/200+1.5*2.54/200],z1):
> spacecurve([xtemp1,ytemp1,ztemp1],p=pos_start-zerocross..
pos_stop,numpoints=5000,axes=boxed);

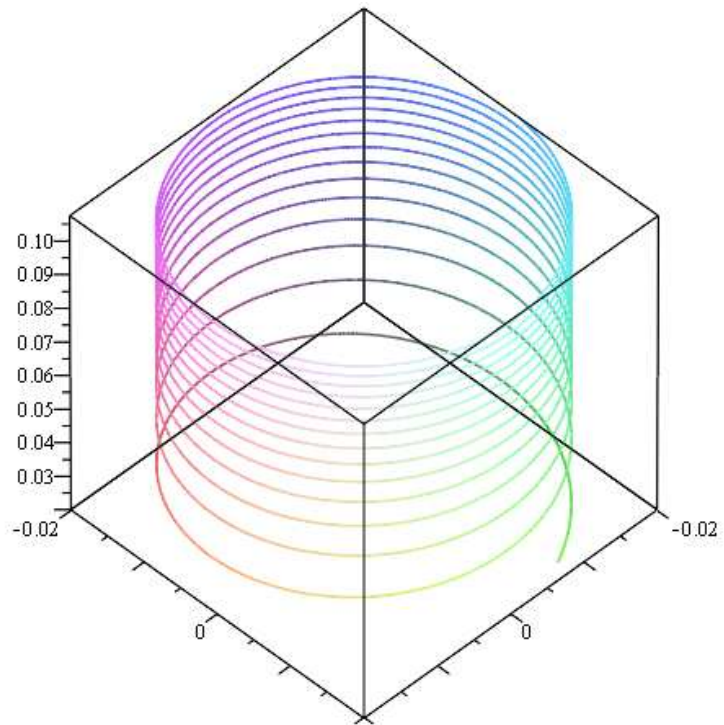
```



```

> xtemp2:=subs ([e=etemp, f=ftemp, g=gtemp, j=jtemp, R=0.081*
2.54/200+1.5*2.54/200], x2) :
> ytemp2:=subs ([e=etemp, f=ftemp, g=gtemp, j=jtemp, R=0.081*
2.54/200+1.5*2.54/200], y2) :
> ztemp2:=subs ([e=etemp, f=ftemp, g=gtemp, j=jtemp, R=0.081*
2.54/200+1.5*2.54/200], z2) :
> spacecurve ([xtemp2, ytemp2, ztemp2], p=neg_start+0..L-zerocross+
neg_stop, numpoints=5000, axes=boxed) ;

```



```
> # number of coils from spacecurves, neg = 11, pos = 52
#neg_wire_length:=12*evalf(Pi)*(0.081*2.54/200+1.5*2.54/100);
#pos_wire_length:=41*evalf(Pi)*(0.081*2.54/200+1.5*2.54/100);
#following lengths from curves generated with 3dpoly in autocad
#cadtools.exe for measurement
```

```
neg_wire_length:=1.797;
pos_wire_length:=3.233;
```

```
total_wire_length:=%%+%;
# 3.28084ft/m
total_wire_length*3.28084*ft;
```

```
neg_wire_length := 1.797
pos_wire_length := 3.233
total_wire_length := 5.030
16.50262520 ft
```

```
> #found some cheap cap tubing, here is the spec
```

```

#capillary tube od = 0.087" id = 0.036"
cross_section:=evalf(Pi)*((0.087*2.54/200)^2-(0.036*2.54/200)^2);
inner_cross_section:=evalf(Pi)*((0.036*2.54/200)^2);
      cross_section := 0.000003178576017
      inner_cross_section := 6.566928930 10-7
(6)
> # copper resistance, resistivity = 1.678e-8 Ohm*meter
rho:=1.678e-8;
resistance_pos:=rho*pos_wire_length/cross_section;
resistance_neg:=rho*neg_wire_length/cross_section;
resistance_total:=rho*total_wire_length/cross_section;
      ρ := 1.678 10-8
      resistance_pos := 0.01706730930
      resistance_neg := 0.009486531025
      resistance_total := 0.02655384032
(7)
> pos_voltage:=Curtemp1*resistance_pos;
neg_voltage:=Curtemp2*resistance_neg;
pos_power:=Curtemp1^2*resistance_pos;
neg_power:=Curtemp2^2*resistance_neg;
total_power:=pos_power+neg_power;
      pos_voltage := 2.218750209
      neg_voltage := 1.233249033
      pos_power := 288.4375272
      neg_power := 160.3223743
      total_power := 448.7599015
(8)
> water_volume_pos:=inner_cross_section*pos_wire_length;
water_volume_neg:=inner_cross_section*neg_wire_length;
      water_volume_pos := 0.000002123088123
      water_volume_neg := 0.000001180077129
(9)
> #heat capacity in J/(m3*K)
water_heat_cap:=4.186*1e6;
      water_heat_cap := 4.186 106
(10)
> water_jk_pos:=water_volume_pos*water_heat_cap;
water_jk_neg:=water_volume_neg*water_heat_cap;
      water_jk_pos := 8.887246883
      water_jk_neg := 4.939802862
(11)
> # For 50 Celcius change
water_j_pos:=60*water_jk_pos;
water_j_neg:=50*water_jk_neg;
      water_j_pos := 533.2348130
      water_j_neg := 246.9901431
(12)
> # time needed to pass water
time_pos:=water_j_pos/pos_power;
time_neg:=water_j_neg/neg_power;
      time_pos := 1.848701236
      time_neg := 1.540584364
(13)
> #volume flow in m3/hour
vol_flow_pos:=water_volume_pos/(time_pos)*3600;
vol_flow_neg:=water_volume_neg/(time_neg)*3600;

```

```

#in l/s
vol_flow_pos*100^3/(3600*1000);
vol_flow_neg*100^3/(3600*1000);
#in L/min
60*vol_flow_pos*100^3/(3600*1000);
60*vol_flow_neg*100^3/(3600*1000);

vol_flow_pos := 0.004134317159
vol_flow_neg := 0.002757575478
0.001148421433
0.0007659931883
0.06890528598
0.04595959130

```

(14)

```

> #from http://www.pressure-drop.com/Online-Calculator/index.html
#want less than 5.5 bar for faucet water ((5.5 bar = 79.75psi))
#pos pressure = 2.57682 bar #laminar Re = 2196
#neg pressure = 0.74636 bar #laminar Re = 1182
#for full length and vol_flow_pos pressure = 3.96362 #laminar Re
= 2196
> 2.57682*14.5;
0.74636*14.5;
3.96362*14.5;

37.363890
10.822220
57.472490

```

(15)

```

> pos_start-zerocross;
pos_stop;
neg_start+0;
L-zerocross+neg_stop;
L+neg_stop-pos_start;

-0.2125000001
-0.015
0.02
0.1074999999
0.32

```

(16)

```

> spacecurve([xtemp1,ytemp1,ztemp1],p=pos_start-zerocross..
pos_start-zerocross+0.01,numpoints=5000,axes=boxed):
spacecurve([xtemp2,ytemp2,ztemp2],p=L-zerocross+neg_stop-0.01+0..
L-zerocross+neg_stop,numpoints=5000,axes=boxed):
> pos_start-zerocross;
pos_stop;
neg_start+0;
L-zerocross+neg_stop;
L+neg_stop-pos_start;

-0.2125000001
-0.015
0.02
0.1074999999
0.32

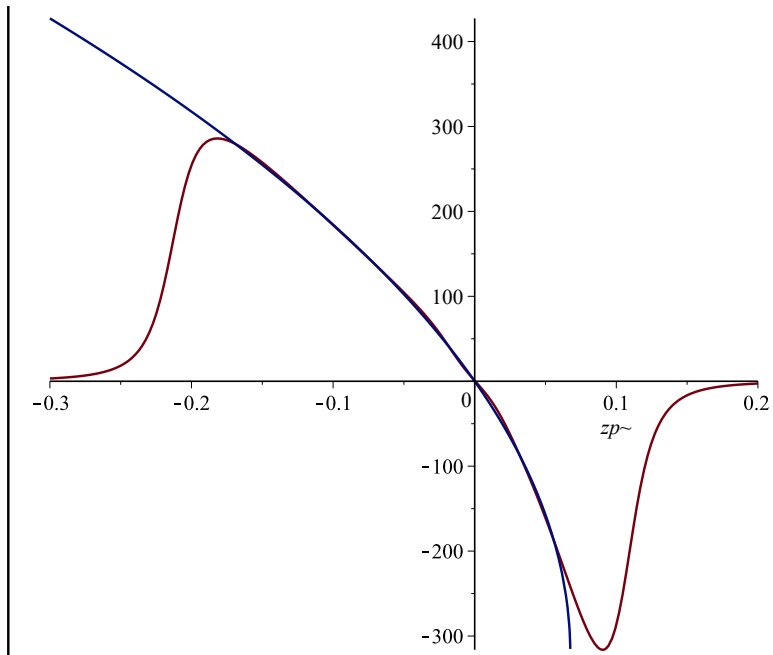
```

(17)

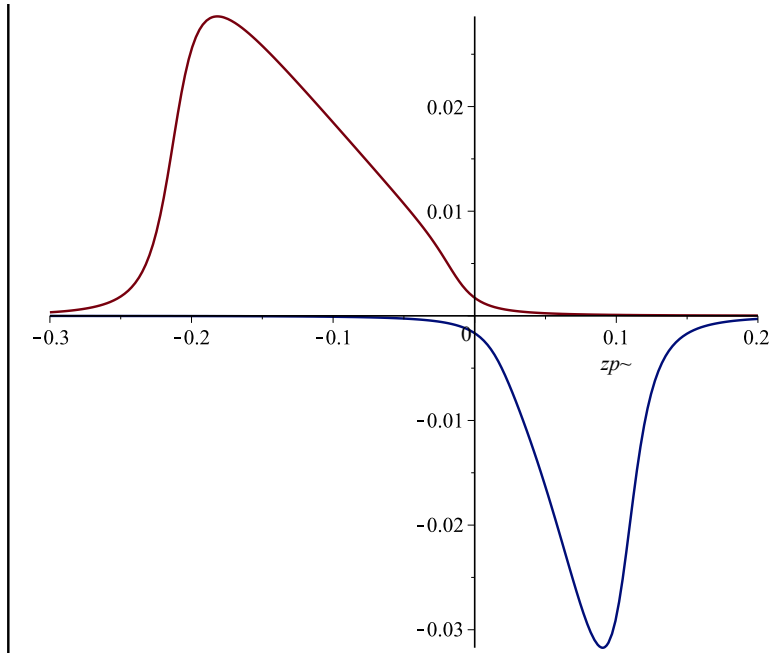
```

> atemp;
btemp;
ctemp;
dtemp;
etemp;
ftemp;
gtemp;
jtemp;
-120
2950
-400
0
40
2000
48000
30000 (18)
> vr/2*Gamma;
1.448382009 106 (19)
> plot(10000*[subs([e=etemp,f=ftemp,g=gtemp,j=jtemp,Cur=Curtemp2],
Bfit_neg)+subs([a=atemp,b=btemp,c=ctemp,d=dtemp,Cur=Curtemp1],
Bfit_pos),subs(z=zp,Bideal)],zp=-0.3..0.2);

```



```
> plot([subs([a=atemp,b=btemp,c=ctemp,d=dtemp,Cur=Curtemp1],
  Bfit_pos),subs([e=etemp,f=ftemp,g=gtemp,j=jtemp,Cur=Curtemp2],
  Bfit_neg)],zp=-0.3..0.2);
```

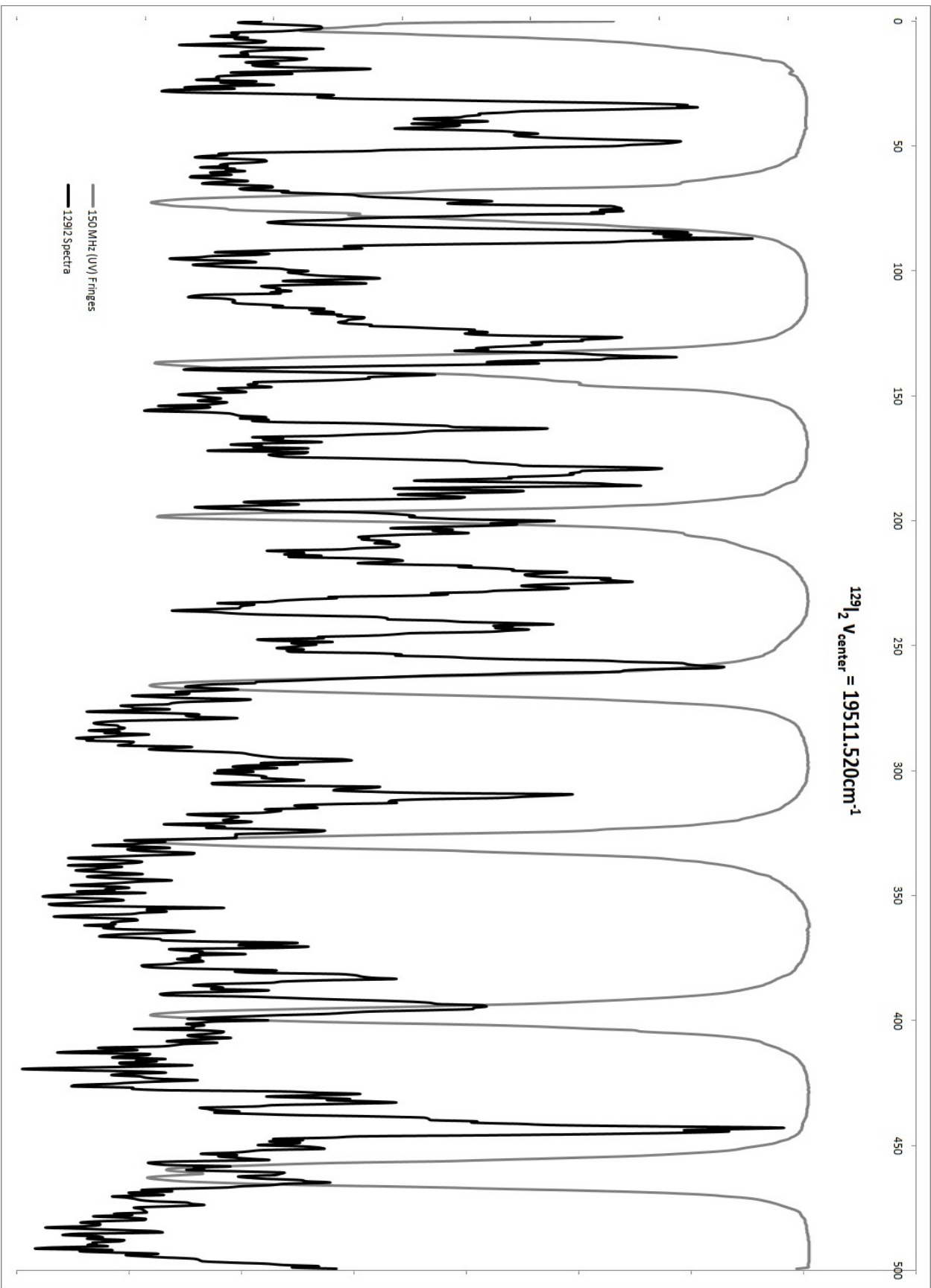


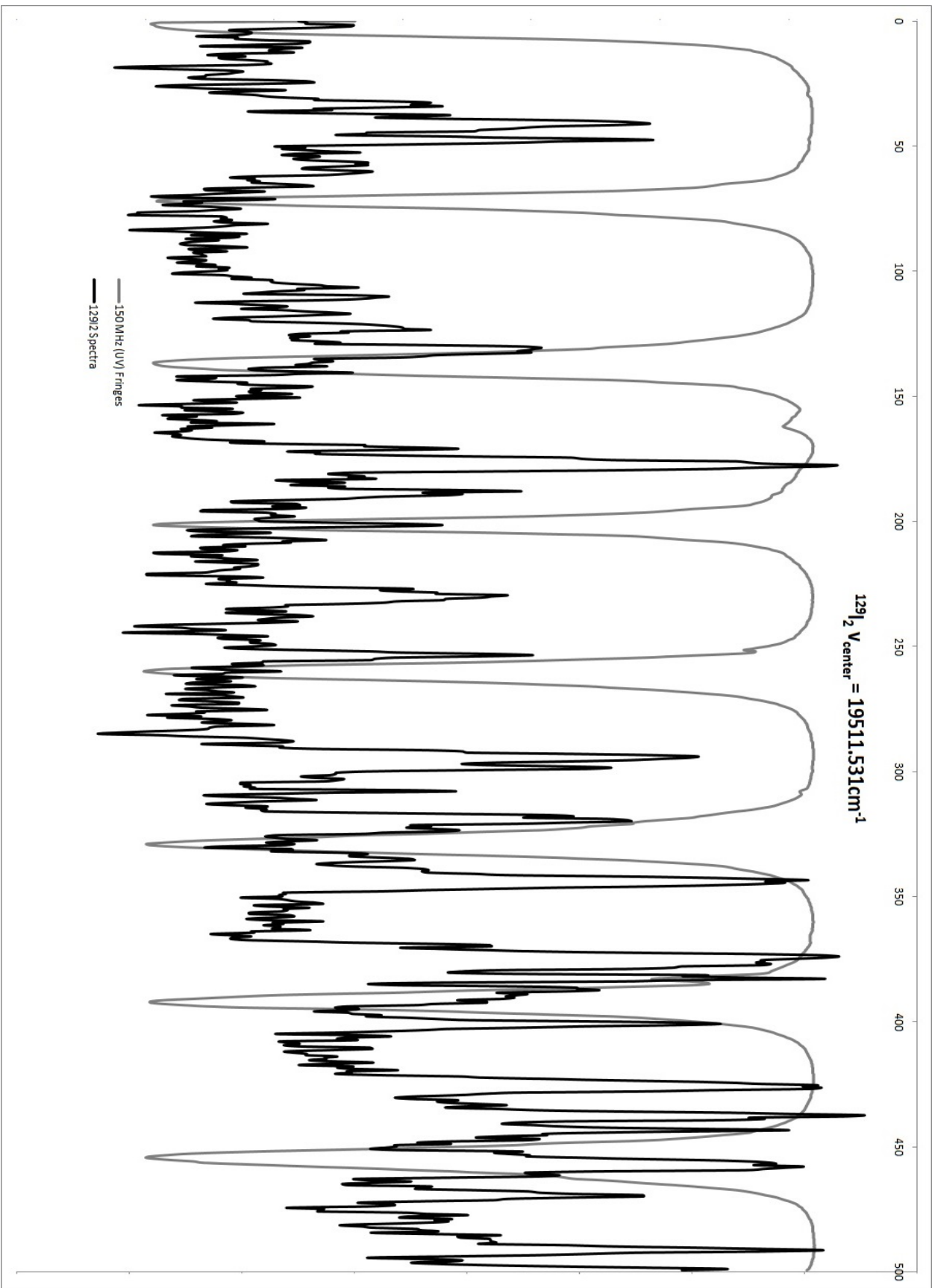
```
> subs ([a=atemp,b=btemp,c=ctemp,d=dtemp,Cur=120,zp=z],Bfit_pos) :  
> subs ([e=etemp,f=ftemp,g=gtemp,j=jtemp,Cur=120,zp=z],Bfit_neg) :
```

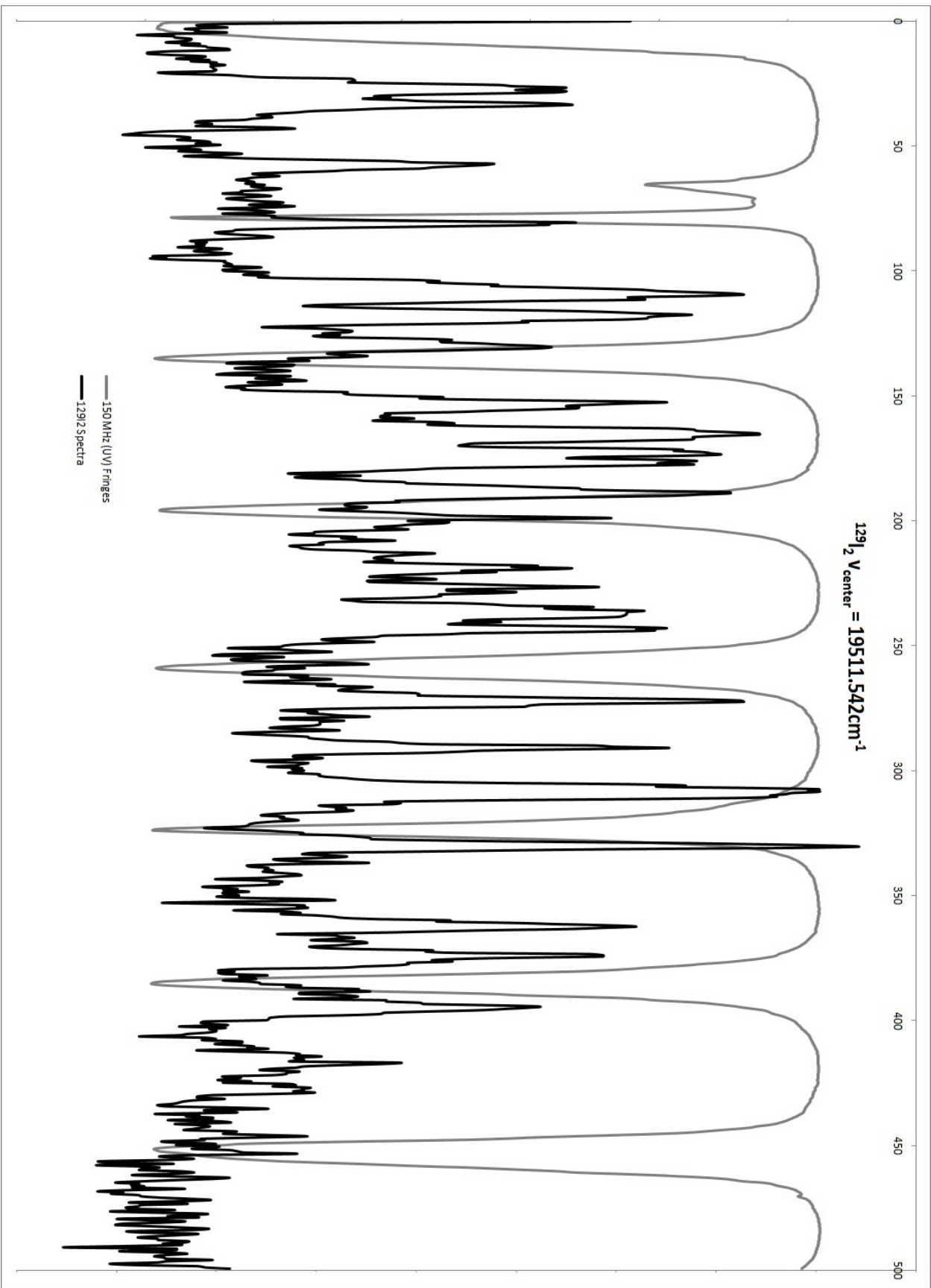
Appendix B

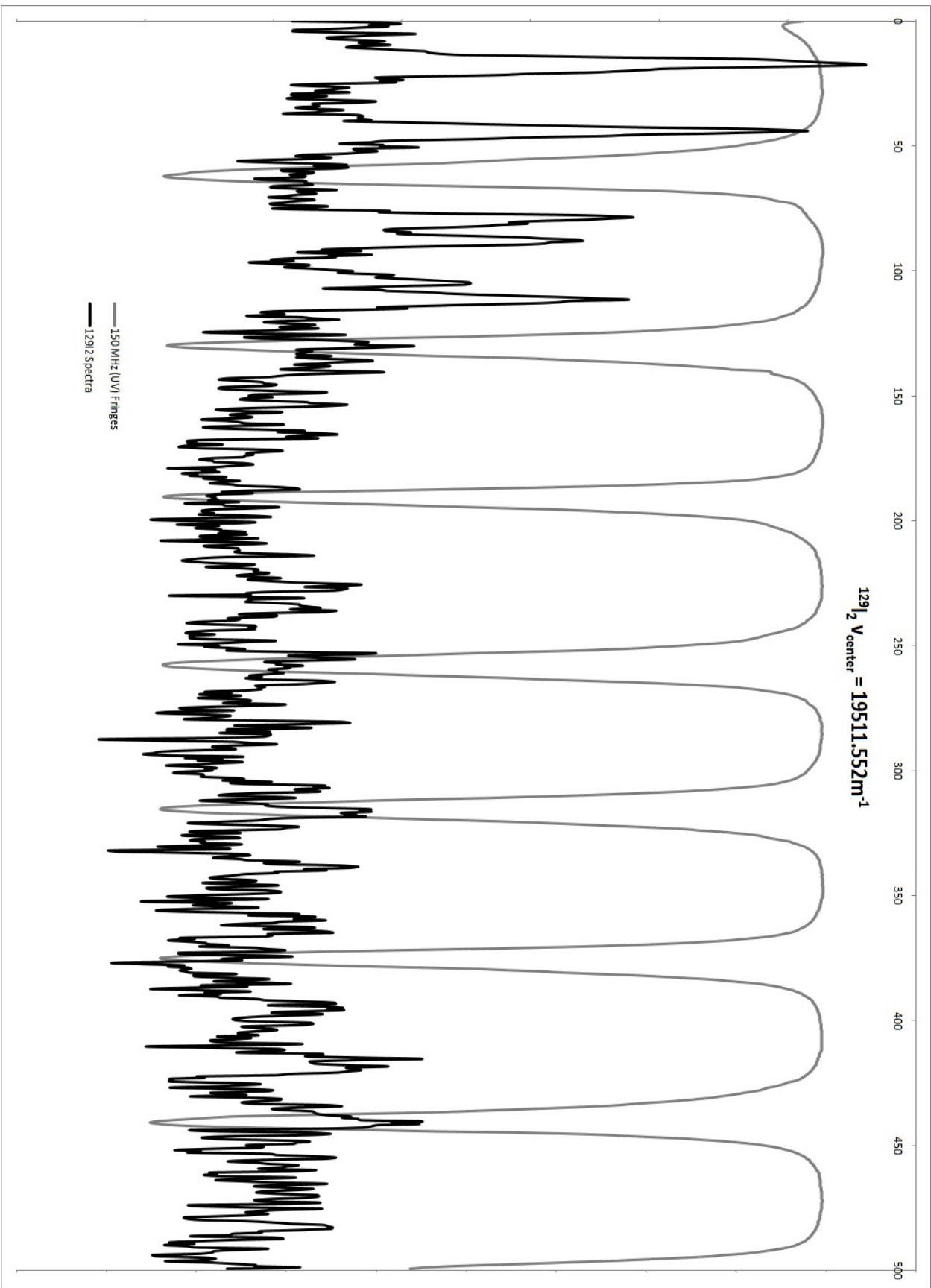
Molecular Iodine-129 Spectra

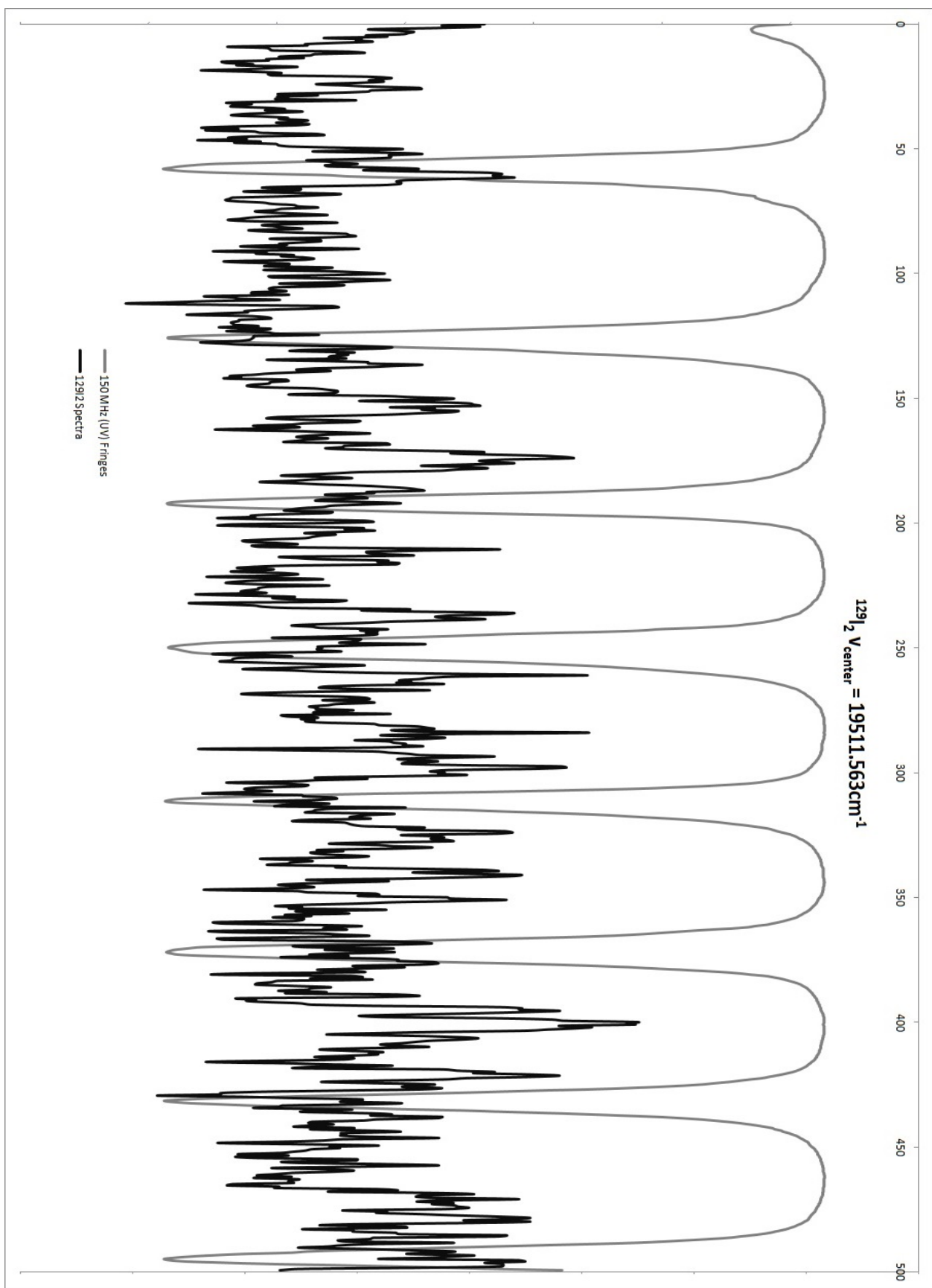
In the following pages you will find the $^{129}\text{I}_2$ spectra that was obtained during the magneto-optical trap investigation of the thesis. All the horizontal axes are expressed in seconds of scan time and the marked frequency corresponds to the frequency center of the 500s scan. The interferometer fringes are from the output of the first second harmonic generation stage at 512nm that was used for the spectroscopy. This interferometer is described in Section 4.3 with a FSR of 72.2433816(66) MHz in vacuum. [52] The fringe spacing in the UV is double this frequency and was more useful information to have at hand during trap runs.











Appendix C

Zeeman Slower Python Simulation Code

```
1  # -*- coding: utf-8 -*-
2
3  """
4  Simulation code for the Zeeman Slower
5
6
7
8  """
9
10 import numpy as np
11 import pandas as pd
12 from scipy.integrate import quad
13 import time
14 import matplotlib.pyplot as plt
15
16 begin_time = time.process_time()
17
18 print(time.asctime(time.localtime()))
19
20 def integrand(v02):
21     return v02**3*(np.exp(-(v02*alpha)**2))
22
23
24 def PosB(I, zz):
25     bc1=np.sqrt(25.12616775+40000*zz**2+1200*zz)
26     bc2=np.sqrt(291.5801868+6400*zz**2+2720*zz)
27     bc3=bc1*bc2
28     PosB=(I/120)*-1/(bc3)*(4.138028521e-8*np.pi*(-11717.33037*bc2-1.84148\\
29     6875e5*bc1+48.37850324*bc1*np.log(-80*zz-17+bc2)*bc2-48.37850324*bc2*\\
30     np.log(-200*zz-3+bc1)*bc1+9.06612972e6*bc1*zz-9.6e6*bc1*zz**3+4.516e7\\
31     *bc1*zz**2+6.39675701e5*bc2*zz+2.4e7*bc2*zz**3-1.1764e8*bc2*zz**2+44.\\
32     32877416*bc3))
33     return PosB
34
35 def NegB(I, zz):
36     bc4=np.sqrt(1913.504671+1.6e5*zz**2-34400*zz)
37     bc5=np.sqrt(2.007885484+2500*zz**2-100*zz)
38     bc6=bc4*bc5
39     NegB=(I/120)*1/(bc6)*(4.138028521e-8*np.pi*(14513.55097*bc4*zz*np.log\\
40     (-50*zz+1+bc5)*bc5-14513.55097*bc5*zz*np.log(-400*zz+43+bc4)*bc4-4.61\\
41     1351401e8*bc5*zz**2-5.358107484e6*bc4*zz**2-6e8*bc4*zz**4-1.144602711\\
42     e5*bc4*zz-7.08e8*bc4*zz**3+4.8e9*bc5*zz**4-1.223769402e7*bc5*zz+5.244\\
43     e9*bc5*zz**3+12072.03232*bc6-5805.420389*bc5*np.log(-400*zz+43+bc4)*b\\
44     c4+5805.420389*bc4*np.log(-50*zz+1+bc5)*bc5+30180.08082*bc6*zz+1.1821\\
45     4465e5*bc5-9576.707292*bc4))
46     return NegB
47
48 plot_x = []
49 plot_x_MHz = []
50 plot_x_sec = []
51 plot_y = []
52 vstarts = []
53 vstops = []
54 vprobes = []
55 times = []
56
57 #####
58 ##### USER PARAMETERS #####
59 #####
60
61 #a list of input parameters
62 s=1.5 #I/Isat
63 dt=2e-6 # time step in sec
64 #detune=-1000 #in gammas
65 detune_start = -1000
66 detune_stop = -99
67 detune_step = 4
```

```

68 velocity_step = 1
69
70 #Zeeman coil current
71 PosI=90
72 NegI=PosI #change this if the two coils have different currents
73
74 #save location
75 filedir = 'D:/docs/Thesis/Current/2020/sim/results/power scaling/'
76 filename = 'data.csv'
77 #automatic file naming
78 filename = str(PosI)+'A s = '+str(s)+' dt = '+str(dt)+' .csv'
79
80 #####
81 ## * END USER PARAMETERS * ##
82 #####
83
84 #list of constants
85 hbar = 1.0545718e-34
86
87 lam = 0.01/(45321.848 - 223.157) #transition wavelegnth in m
88 k = 2.0*np.pi/lam #28336343.2664 #magnitude of k vector for cooling transition
89
90 gam= 4.54e7 # A coefficient, in s-1
91 kgam= k/gam #per 1 m/s, =k/gamma
92
93 m = 4.6456776e-26 #Silicon-28 mass in kg
94
95 F=hbar*k*gam/m #prefactor for acceleration
96
97 mu_b = 9.274e-24
98
99 kb=1.38064852e-23 #Boltzmann constant in J/K
100
101 mugam=-mu_b/gam/hbar #B-field prefactor
102
103 #atomic beam parameters, T=1380 C
104 T=1380+273.15
105 alpha=np.sqrt(m/(2*kb*T)) #alpha is sqrt(m/2kT)
106 f_v=2*alpha**4 #normalization factor for the velocity integral
107
108 for detune in range(detune_start, detune_stop, detune_step):
109     loop_begin_time = time.process_time()
110     r=velocity_step #velocity step increment
111     probe_v = -detune/kgam #for a given detuning, the resonant velocity
112     vstart = int(round(probe_v - 200,0)) #input this value based on detuning
113     vend = int(round(probe_v + 200,0)) #input this value based on detuning
114     if vstart < 30: vstart = 30
115
116
117     print(" detune=",detune, "probe v =", round(probe_v,4), "time step",dt\\
118           , "velocity step",r)
119     print(" s=", s, "B field current, positive coil",PosI,"negative coil",\\
120           NegI)
121     print(" velocity from ",vstart, "m/s to ",vend," m/s")
122     #Create a matrix fin for final values: initial v, final v, A
123     #fin = np.zeros ((100000,4))
124
125     #Initialize the signal and define the starting position
126     signal=0
127     z0=-0.48
128
129     for v02 in range (vstart,vend,r):
130         ans, err = quad(integrand, v02, v02+r) #window for integral
131         #print("population in", v02, "to", v02+r, "is", f_v*ans)
132         z=-0.48
133         v=v02
134         #print("in the velocity loop, the starting velocity is now", v02)

```

```

135     while z < 0.28:
136         #calculate B field at each z, positive and negative coils
137         #total B
138         BZ=(PosB(PosI, z)+NegB(NegI, z))
139
140         delta=detune+kgam*v-mugam*BZ
141         rho22=1/2*s/(1+s+4*delta**2) #rho22 from 2 level bloch eqns
142         A=gam*rho22
143         a=F*rho22
144
145         zf=z+v*dt-1/2*a*dt**2
146         vf=v-a*dt
147         """
148         if zf>=0.28:
149             vfin=vf
150             Afin=A
151             break
152         #"""
153         if vf<=0:
154             Afin=0
155             vfin=1
156             break
157         #"""
158         z=zf
159         v=vf
160     Afin=A
161     vfin=vf
162     signal=signal+Afin*f_v*ans*0.01/vfin
163     #print ("velocity",v02, "final v",vfin, "A",A,"signal",signal)
164     #print("from", vstart,"m/s to ", vend,"the signal is",signal )
165     loop_end_time = time.process_time()
166     loop_time = loop_end_time - loop_begin_time
167     print(detune, signal, "\n      --- %g seconds ---" % (loop_time))
168     plot_x.append(detune)
169     plot_x_MHz.append(detune*gam/2/np.pi/1e6)
170     plot_x_sec.append(detune*gam/2/np.pi/1e6/27.6) #27.6MHz/sec to match exp
171     plot_y.append(signal)
172     vstarts.append(vstart)
173     vstops.append(vend)
174     vprobes.append(probe_v)
175     times.append(loop_time)
176
177     fig, ax1 = plt.subplots()
178     ax1.plot(plot_x_MHz,plot_y, marker=".")
179     ax1.set_title(str(PosI)+"A, timestep="+str(dt)+", s="+str(s))
180     ax1.set_xlabel("Detuning in MHz")
181     ax1.set_ylabel("Signal (arb)")
182     plt.show()
183
184
185     end_time = time.process_time()
186     total_time = end_time - begin_time
187
188
189
190     d = {
191         'detune':plot_x,
192         'detune MHz':plot_x_MHz,
193         'sec':plot_x_sec,
194         'vprobe':vprobes,
195         'signal':plot_y,
196         'vstarts':vstarts,
197         'vstops':vstops,
198         'vstep':r,
199         'compute time':times,
200         's':s,
201         'dt':dt,

```

```
202         'posI':PosI,  
203         'negI':NegI,  
204         'total time':total_time  
205     }  
206     data = pd.DataFrame(data=d)  
207     print (data)  
208  
209     #""  
210     data.to_csv(filedir+filename)  
211     #""  
212  
213  
214     print(" --- %g seconds ---" % (total_time))  
215  
216
```